# Internal Wave Propagation in the Arctic Ocean

Dissertation submitted by

**Joel Bracamontes Ramírez**

in partial fulfillment of the requirements
for the degree of

Doctor of Natural Sciences (Dr. rer. nat.)

to

Faculty 1
Physics and Electrical Engineering
University of Bremen

1. **Reviewer:** Dr. Maren Walter
   Institute of Enviromental Physics
   University of Bremen

2. **Reviewer:** Prof. Dr. Dirk J. Olbers
   Institute of Enviromental Physics
   University of Bremen

**Submission:** 11 April 2024

**Colloquium:** 10 June 2024

# Abstract

The propagation of internal gravity waves in the Arctic Ocean is studied using direct and indirect observations, reanalysis data and two numerical models. I focus on how stratification modifies wave propagation and its connection to the pathways of internal wave energy from the surface to the deep ocean. Understanding internal wave propagation in the Arctic Ocean is crucial for better understanding wave-driven mixing and its implications for climate projections. Therefore, three specific aspects of internal wave propagation have been addressed in this thesis.

First, the transient transmission of a wave packet across a density staircase is studied using a 2D Boussinesq model. A series of simulations with fixed wave frequency and varying horizontal wave number are carried out. The results show that the incident wave excites trapped modes by a near-resonance mechanism, which slowly transfer energy above and below the staircase. A theoretical prediction was made using typical values for thermohaline staircases and internal waves in the Arctic Ocean. Surface-generated near-inertial internal waves that excite trapped modes should have a critical horizontal wavelength of $\sim 400\,\mathrm{m}$. For higher-frequency non-hydrostatic waves, this critical horizontal wavelength decreases to $\sim 80\,\mathrm{m}$. Such waves are likely to be generated by wind-driven ice floes.

Secondly, the existence of turning depths for near-inertial internal waves and their effect on wind-driven deep mixing is assessed using 10 years of temperature and salinity profiles in the Canadian Basin. It is found that turning depths exist in the deep Canadian Basin at $\sim 2750\,\mathrm{m}$, but with decreasing distance from the bottom towards the slope. A subsequent discussion focuses on the possible topographic interaction of internal wave reflection and dissipation, especially where turning depths are shallow and above the slope, where the evanescent perturbation of the internal waves can still interact with the topography.

Finally, direct observations of near-inertial internal waves are investigated using current observations from a mooring on the Gakkel Ridge, and their surface generation is addressed using a wind and ice drift speed and ice concentration dataset. Cross-correlation analysis shows that there is a correlation between ice drift speed and near-inertial wave energy with a lag of $< 26\,\mathrm{days}$. In addition, a correlation of $\sim 15\,\mathrm{days}$ is observed between the wind factor and the near-inertial wave energy. This result suggests that near-inertial internal waves may be generated at the surface by an interplay of wind and ice properties and propagate from the surface to the seafloor. Evidence for wave reflection is also found, and 2D numerical simulations of waves reflected at a turning depth are performed and compared with observations, showing qualitative agreement.

# Zusammenfassung

Die Ausbreitung von internen Schwerewellen im Arktischen Ozean wird mit Hilfe von direkten und indirekten Beobachtungen, Reanalysedaten und zwei numerischen Modellen untersucht. Ich konzentriere mich darauf, wie die Schichtung die Wellenausbreitung verändert und wie sie mit der Ausbreitung der internen Wellenenergie von der Oberfläche in die Tiefe zusammenhängt. Das Verständnis der Ausbreitung interner Wellen im Arktischen Ozean ist entscheidend für ein besseres Verständnis der wellengetriebenen Vermischung und deren Auswirkungen auf Klimaprojektionen. Daher wurden in diesem Projekt drei spezifische Aspekte der internen Wellenausbreitung untersucht.

Zunächst wird die transiente Übertragung eines Wellenpakets über eine Dichtetreppe mit Hilfe eines 2D-Boussinesq-Modells untersucht. Eine Reihe von Simulationen mit fester Wellenfrequenz und variabler horizontaler Wellenzahl wird durchgeführt. Die Ergebnisse zeigen, dass die einfallende Welle durch einen Quasi-Resonanzmechanismus gefangene Moden anregt, die langsam Energie oberhalb und unterhalb der Treppe übertragen. Eine theoretische Vorhersage wurde unter Verwendung typischer Werte für thermohaline Treppen und interne Wellen im Arktischen Ozean durchgeführt. Die kritische horizontale Wellenlänge für oberflächennahe interne Wellen, die stehende Moden anregen, beträgt $\sim 400\,\mathrm{m}$. Für nicht-hydrostatische Wellen mit höheren Frequenzen verringert sich die kritische horizontale Wellenlänge auf $\sim 80\,\mathrm{m}$. Solche Wellen werden wahrscheinlich durch vom Wind angetriebene Eisschollen erzeugt.

Zweitens wird das Vorhandensein von Umkehrtiefen für interne Wellen nahe der Trägheitsfrequenz und deren Auswirkung auf die windbedingte Tiefenmischung anhand von Temperatur- und Salzgehaltsprofilen aus den Jahren 2005 bis 2014 im Kanadischen Becken untersucht. Es wird festgestellt, dass Umkehrtiefen im tiefen Kanadischen Becken bei $\sim 2750\,\mathrm{m}$ existieren, jedoch mit abnehmender Entfernung vom Boden zum Hang hin. Eine anschließende Diskussion konzentriert sich auf die mögliche topographische Wechselwirkung zwischen Reflexion und Dissipation interner Wellen, insbesondere dort, wo die Umkehrtiefen gering sind und sich oberhalb des Hanges befinden, wo die evaneszente internen Wellen noch mit der Topographie interagieren kann.

Schließlich werden direkte Beobachtungen interner Wellen nahe der Trägheitsfrequenz mit Hilfe von Strömungsbeobachtungen von einer Verankerung auf dem Gakkelrücken und ihre Erzeugung an der Oberfläche mit Hilfe von Wind- und Eisdriftgeschwindigkeits- und Eiskonzentrationsdatensätzen untersucht. Die Kreuzkorrelationsanalyse zeigt eine Korrelation zwischen der Eisdriftgeschwindigkeit und der Energie der internen Wellen mit einer Verzögerung von $< 26$ Tagen. Zusätzlich wird eine Korrelation von $\sim 15$ Tagen zwischen dem Windfaktor und der Energie der internen Wellen beobachtet. Dieses Ergebnis deutet

darauf hin, dass interne Wellen an der Oberfläche durch eine Kombination von Wind- und Eiseigenschaften erzeugt werden und sich von der Oberfläche in die Tiefe ausbreiten. Es wurden auch Hinweise auf Wellenreflexionen gefunden und 2D numerische Simulationen von reflektierten Wellen in einer Umkehrtiefe durchgeführt und mit Beobachtungen verglichen, die eine qualitative Übereinstimmung zeigten.

# Contents

# Chapter 1

# 1 Introduction

## 1.1 Arctic Ocean

The Arctic Ocean is located in the Northern Hemisphere, including the North Pole. In winter, it is almost completely covered by a thin layer of sea ice, which decreases by up to three-thirds in summer. Its major basins and adjacent seas cover an area of 14 million km$^2$. The main physical features of the Arctic Ocean are the Canadian Basin, separated from the smaller Eurasian Basin by the submarine Lomonosov Ridge, and the extensive continental shelves of the Eurasian side, which occupy about 35 % of the total ocean. It also includes the only deep passage, the Fram Strait between Greenland and Svalbard (Herman, 2012).

The main oceanic inflows come from the Atlantic Ocean through the Fram Strait and the Barents Sea opening, and from the Pacific Ocean through Bering Strait (Fig. 1.1a). Freshwater inflows from North America and Siberian rivers are also significant. These inflows mainly determine the water column salinity and temperature variability, with salinity dominating the stratification, resulting in a mean halocline rather than a thermocline.

The water mass distribution in the Arctic Ocean is typically characterized by relatively cold and fresh water over warm and salty water (Fig. 1.1b). Due to the strong halocline and the presence of sea ice, the Arctic Ocean exhibits a complex variety of mixing processes. These processes include convection due to surface buoyancy fluxes resulting from turbulence driven by stress at the ice-ocean interface, double-diffusive mixing, and mixing by internal waves (Timmermans & Marshall, 2020). In particular, internal waves provide significant mechanical energy for abyssal ocean mixing, making it crucial to better understand their generation, propagation, and dissipation, which are influenced by the high-latitude Coriolis effect and sea ice cover (Timmermans & Marshall, 2020).

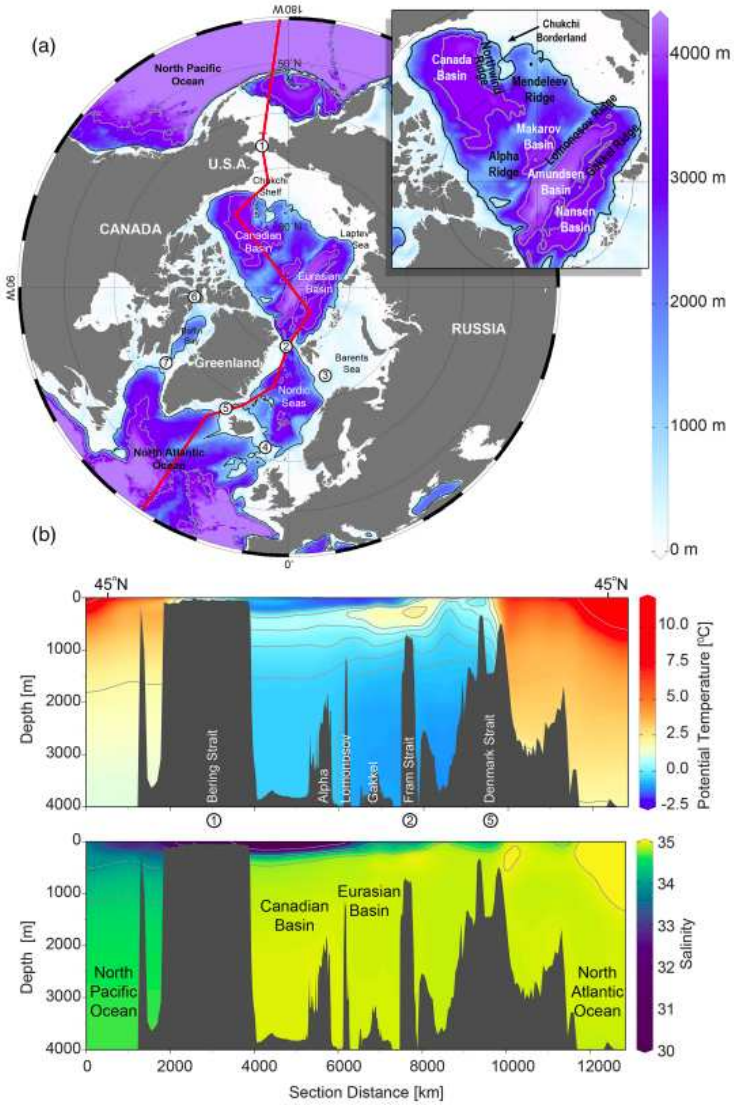


Figure 1.1: Arctic Ocean. (a) shows the main geographic features and the inset depicts the Arctic Ocean in details. The number refer to (1) Bering Strait, (2) Fram Strait, (3) Barents Sea Opening, (4) Greenland-Scotland Ridge, (5) Denmark Strait, (6) Lancaster Sound and (7) Davis Strait. The red line depicts the transect showed in (b) potential temperature (top) and salinity (bottom). Figure and caption adapted from Timmermans and Marshall (2020).

## 1.2 Waves

A wave is a moving signal, typically moving at a rate different from the motion of the medium, e.g. in a fluid, the signal could be the surface rise in the ocean due to surface gravity waves, or the distortion of isopycnals in the interior of the ocean due to internal gravity waves. This up and down motion away from equilibrium experiences a restoring force due to buoyancy and ultimately gravity (Pedlosky, 2003). For small amplitude waves we can often find a solution in the form of a plane wave $\phi(\mathbf{x}, t) = \Re\, A\, e^{\imath}(\mathbf{K} \cdot \mathbf{x} - \omega t)$, where $\phi$ is a field variable, such as velocity, density, pressure, $\omega$ is the wave frequency, $\mathbf{K}$ is the wavenumber vector, $A$ is the wave amplitude, and $\Re$ means to take the real part of the expression. For internal gravity waves, the small perturbation from the rest state is characterized by oscillations with a characteristic buoyancy frequency $N = (-g/\rho_0\, \partial\overline{\rho}(z)/\partial z)^{1/2}$, where $g$ is gravity, $\rho_0$ is the reference density, and $\partial\overline{\rho}(z)/\partial z$ is the background density gradient. $N$ is the maximum frequency for gravitational oscillations, which impose a local constraint on wave propagation. In the ocean, including the effect of rotation leads to a dispersion relation for internal inertial gravity waves $\omega = f^2 \sin^2\theta + N^2 \cos^2\theta$, where $f$ is the Coriolis frequency and $\tan\theta = m/|\mathbf{K_h}|$, where $m$ is the vertical wavenumber and $\mathbf{K_h} = k + l$ is the horizontal wavenumber. Thus, the wave frequency depends only on the angle and not on the wavenumber. Furthermore, since in the ocean in general $f << N$, it follows that $f \leq \omega \leq N$, giving the upper and lower bounds for $\omega$, which limits wave propagation (Pedlosky, 2003; Olbers, 2012).

An important quantity of internal waves propagation is the group velocity $\mathbf{c}_g = \partial\omega/\partial\mathbf{K}$, which is orthogonal to the wavenumber vector $\mathbf{c}_g \cdot \mathbf{K} = 0$ (Olbers, 2012). In the two-dimensional case, with $l = 0$, the group velocities are $c_{gx} = (k/\omega)(N^2 - \omega^2)/(k^2 + m^2)$ in the $x$-direction and $c_{gz} = (m/\omega)(f^2 - \omega^2)/(k^2 + m^2)$ in the $z$-direction. From these group velocity equations it follows that if $\omega = N$ then $c_{gx}$ vanishes. Furthermore, $m(z) = k((N^2 - \omega^2)/(\omega^2 - f^2)^{1/2})$, henceforth $c_{gz}$ also vanishes, there is no wave propagation, and the waves become non-propagating oscillations. To conserve energy, internal waves reflect from such regions. However, total reflection is a consequence of ray theory, and it is valid if the vertical variations of $N$ are large compared to the vertical wavenumber of the wave, otherwise it is not reliable (Sutherland, 2010c).

## 1.3 A changing Arctic – the internal wave conundrum

Internal (gravity) waves propagate in density-stratified fluids, transporting energy both horizontally and vertically. Particularly in the ocean they play an essential role in the vertical transport of heat and salinity caused by the mixing that occurs when the waves break (Ferrari & Wunsch, 2009a). The energy associated with the internal wave climate in the Arctic Ocean is lower than in other oceans (D'Asaro & Morehead, 1991), partly because a thick sea ice layer covers the ocean surface, preventing the wind from acting on it (Fig. 1.2 a). The ice cover varies non-uniformly in both time and space. In the marginal zone and towards the coast, the sea ice has a seasonal cycle, with thinner sea ice that usually does not survive the summer (Walsh et al., 2017). In contrast, the sea ice is thicker at higher latitudes and can survive several years (Kwok, 2018). This sea ice pattern is changing. In the last decades, the summer ice cover has decreased considerably, which implies more open ocean areas where the wind can act on and transfer energy and momentum into the ocean (Rainville et al., 2011b; Rainville & Woodgate, 2009). In particular, an increase in near-inertial wave amplitude (Dosser et al., 2014; Dosser & Rainville, 2016a) and kinetic energy (Fine & Cole, 2022) in the Canadian Basin and the enhancement of wind-driven vertical heat fluxes and dissipation rates in the Eurasian Basin (Meyer et al., 2017; Peterson et al., 2017) have already been observed.

As the summer sea ice extent continues to decrease and the areas with seasonal sea ice cover increase (Fig. 1.2 b), wind-driven internal waves will be more energetic, mainly in the near-inertial range (Rainville & Woodgate, 2009; Rainville et al., 2011b). This shift in ice cover dynamics and the fact that most of the Arctic Ocean is located north of the $M_2$ critical latitude make wind-driven internal waves an important contributor to altering the wave climate. In a fully sea-ice-covered Arctic Ocean, near-inertial internal waves generated at the surface are hypothesized to survive one round-trip to the bottom and then dissipate partially under sea ice (Pinkel, 2005; Cole et al., 2018). In a feasible, less dissipative future scenario with more open ocean areas (Kim et al., 2023), we expect surface-generated near-inertial internal waves to travel and carry energy over longer distances towards the slope or the bottom.

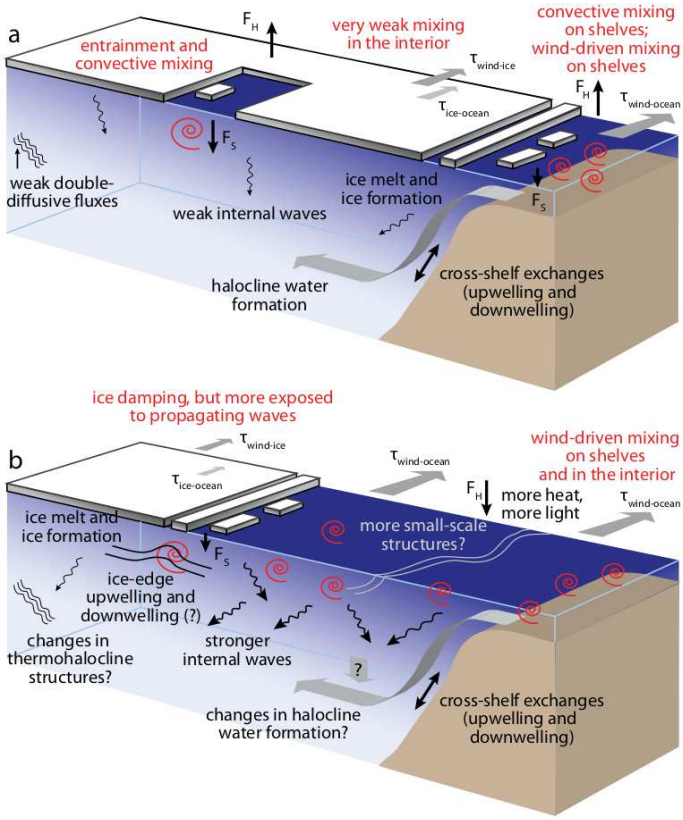


Figure 1.2: Schematic of the dominant mixing processes in the Arctic Ocean with a) small seasonal ice-free areas and b) large ice-free areas. With sea ice cover (a), the wind transfers significant momentum and energy to the ice shelves only in summer. Sea ice effectively acts as a frictional boundary layer. It inhibits wind-driven internal wave generation and dampens existing internal waves. In contrast, in a plausible future with more open water areas (b), the wind effectively generates more internal waves that propagate into the deep interior, potentially enhancing mixing, modifying stratification and eroding the thermohaline staircase observed throughout the Arctic Ocean. Figure and caption adapted from Rainville et al. (2011b).

The frequency of propagating internal waves is limited by the background buoyancy frequency $N$, which is a measure of the rate at which the background density increases with depth. In particular, the frequency of internal waves in the ocean is limited by $f \leq \omega \leq N$ (see Sec. 1.2), and the stratification of the water columns modifies the internal wave propagation. In the mid-water of the Arctic Ocean, the interaction between downward propagating internal waves encountering a thermohaline density staircase (Fig. 1.3) is of particular interest for understanding the propagation of wave energy. The vertical profile of the density in a staircase is characterized by steps of uniform density ($N \sim 0$) separated by sharp density jumps, which have been observed in different regions of the ocean from the tropics to the Arctic Ocean

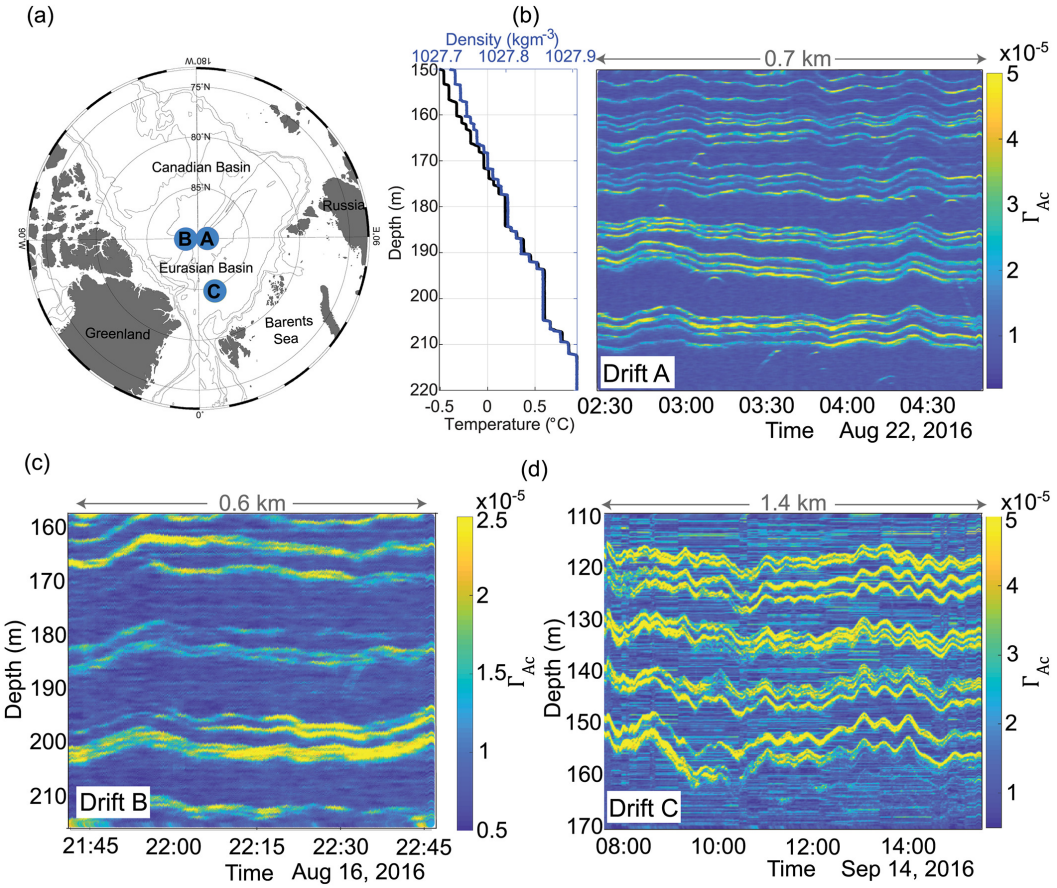


Figure 1.3: a) An example of thermohaline staircases and their locations in the Arctic Ocean showing thermohaline staircase collected from a Simrad EK80 broadband echo sounder mounted on the icebreaker Oden from August–September 2016. Acoustics maps at b) 89.7°N, 52.1°E, c) 89.3°N, 70.2°W. d) 84.4°N, 17.4°E. Adapted from Shibley et al. (2020).

and occur as a result of double diffusion processes (Kunze et al., 1987; Schmitt et al., 1987; Zodiatis & Gasparini, 1996; Padman & Dillon, 1988; Guthrie et al., 2017; Shibley et al., 2017).

## 1.4 Upper ocean - thermohaline staircases

Observations have revealed the presence of a staircase horizontally over a thousand square kilometers in the Canadian Basin, located a few hundred meters below the surface and extending over 100 m depth (Timmermans et al., 2008; Boury et al., 2022). The steps of the staircase have depths on the order of 1 m with sharp density jumps having thicknesses on the order of 1 cm. As Arctic sea ice decreases, winds blowing over the exposed ocean surface or driving mobile ice floes can more

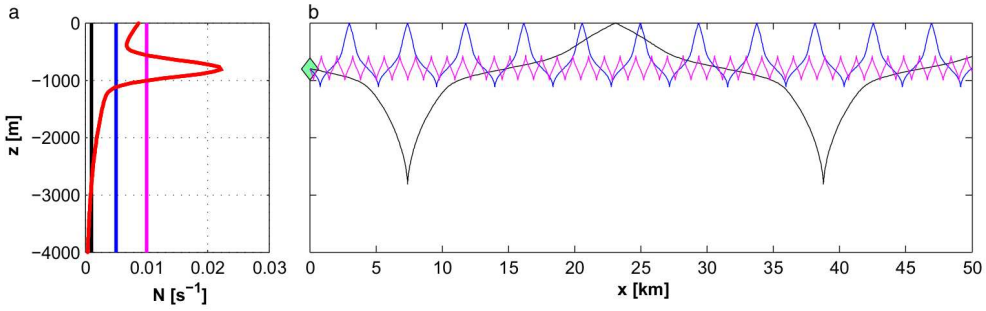


Figure 1.4: Schematic of internal wave reflection upon turning depths. a) buoyancy frequency $N$ (in red) and different wave frequencies $\omega$ (vertical lines). b) propagation of internal waves with frequencies depicted in (a). Notice that internal wave reflection occur when $N \leq \omega$, which is the definition of a turning depth. Adapted from Olbers (2012)

frequently generate internal waves that then propagate downward and interact with the thermohaline staircases (Rainville et al., 2011a).

Within the steps of the staircase, an incident internal wave is evanescent and internal waves are reflected. However, if the steps are sufficiently small compared to the size of the incident wave, the wave can partially transmit through them, henceforth the staircase acts as a sort of wave filter (Sutherland, 2016; Wunsch, 2018). Internal waves partially transmitted through the staircase can act as a source of mixing that may bring warm and salty Atlantic water (Fig. 1.1b) at depth closer to the surface, which can then enhance sea ice melting.

## 1.5 Deep ocean – turning depths

In the Arctic Ocean, when internal waves are partially or fully transmitted to deeper waters, they can reach the bottom layer where their frequency $N(z) < \omega$ and where they cannot propagate (Fig. 1.4). Waves are more likely to be reflected at these so-called turning depths than to break (Paoletti & Swinney, 2012a). Therefore, the internal wave path to the surface is shortened after reflection at turning depths. Below a turning depth, waves are evanescent and their amplitudes decrease exponentially with depth (Sutherland, 2010a). Therefore, if the turning depth is well above the topography, waves are unlikely to interact with the bottom (Paoletti et al., 2014a) and directly cause deep mixing.

Turning depths for the semidiurnal tide, with $N(z) \leq M_2 \approx 1.405 \times 10^{-4} s^{-1}$, are ubiquitous in the entire Ocean (King et al., 2012b). In the South China Sea, turning depths were also found for the diurnal tide $K_1 \approx 7.292 \times 10^{-5} s^{-1}$ (Liu et al., 2022). For near-inertial internal waves, the buoyancy frequency must be in the order of $N(z) \leq \omega \approx 1.4 \times 10^{-4} s^{-1}$, which corresponds to the average Coriolis frequency in the Arctic Ocean ($> 70\,N°$). Such a weak stratification is found mainly at great depths, for example, in the abyssal plain of the Canadian Basin below $\sim 2700\,m$ (Timmermans et al., 2007; Timmermans & Garrett, 2006).

## 1.6 Research Questions

Based on the literature and concepts outlined above, I propose that one of the key components to understanding how the Arctic Ocean climate will change is to study the propagation of surface-generated internal waves into the Arctic Ocean interior and onto the shelves, their interaction with key density features, and their contribution to driving deep mixing. Therefore, the aim of this research is to study the propagation of internal waves in the deep Arctic Ocean, focusing on their interaction with the thermohaline staircases, the deep homogeneous layer, and the topography, using a combination of new direct observations, data sets, spectral analysis, development and setup of idealized numerical simulations, and internal wave theory. Three specific research questions are addressed

### Q1: Thermohaline staircases and transient transmission

Thermohaline staircases act as a filter for internal waves (Sutherland, 2016). Theoretical predictions have been made for the transmission and reflection of monochromatic (in frequency) horizontally periodic internal waves incident upon a single uniform-density slab of fluid (Sutherland & Yewchuk, 2004), two mixed layers (Ghaemsaidi et al., 2016a) and for an incident plane wave across a density staircase with an arbitrary number of equal-sized steps (Sutherland, 2016). In reality, wind-driven internal waves are a transient phenomenon. However, the transient interaction between a wavepacket and density steps has not been well studied, except for a numerical examination of finite-amplitude effects associated with a wavepacket propagating across a density step with no density jump above and below the step (Brown et al.,

2008).

Thus, in Chapter 2, I address the question:

***What is the transmission process of the transient interaction between an incident vertically localized internal wavepacket and a density staircase?***

**Q2: Turning depths and topographic interaction**

Tidal energy is weak, in part because most of the Arctic Ocean lies north of the critical latitude for semidiurnal tides at ∼74.5 °N. However, beyond this latitude in the interior of the Canadian Basin, away from the continental slopes, upward and downward near-inertial internal wave energy fluxes dominate at the surface (Halle, 2003; Pinkel, 2005) even though the weak tides do not generate strong upward internal waves. A possible explanation without observational evidence for this upward wave flux paradox is that surface-generated near-inertial internal waves are reflected after encountering an internal turning depth (Gregg, 2021). In addition, deep mixing is enhanced on slopes, especially in areas of steep topography (Rainville & Winsor, 2008). If tides do not play a significant role in driving the mixing interior beyond the critical latitude, the pathways of near-inertial internal waves are key to understanding the mechanisms that drive deep mixing in the Canadian Basin.

The question addressed in Chapter 3 is therefore:

***Do near-inertial turning depths exist in the Deep Canadian Basin and what are the consequences of turning depths for deep mixing?***

**Q3: Deep near-inertial internal waves**

In this thesis, based on previous research, we assumed that in the Arctic Ocean, internal waves propagate downwards and eventually interact with the thermohaline staircases and turning depths. I have used indirect observations, numerical simulations and theory to address the above questions. However, up to know there was no direct observational evidence for near-inertial internal waves at the bottom. A new set of current observations at 83 °N, beyond the critical latitude for the $M_2$ tide, allows us to address the next question using direct observations deep currents in Chapter 4:

***Do near-inertial internal waves reach the bottom in the Eurasian Basin of the Arctic Ocean after surface generation by a combination of wind and sea ice properties?***

# Chapter 2

In this chapter I addressed the first research question. What is the transmission process of the transient interaction between an incident vertically localized internal wavepacket and a density staircase?

This chapter is part of the homonymous manuscript submitted to Physical Review Fluids, which is currently under consideration. My contributions were as follows:

I actively participated in modifying the original research question as we obtained simulation results. I co-designed and ran the numerical simulations and processed the output, for which I modified previously written code and implemented and wrote new code. I wrote the first draft of the manuscript and prepared the figures, which was edited and submitted by co-author Prof. Dr. Bruce Sutherland. The theoretical contributions, in particular Sections 2.2.1 and 2.2.2 and the Appendix A, were entirely developed by Prof. Dr. Bruce Sutherland. I have included them in this thesis for completeness. The section "Near-Resonant Mode Excitation by an Incident Wavepacket" of the submitted manuscript is not included in this thesis. Parts of the introduction have also been used.

The following preprint is already published and the used content in this thesis may slightly differ from the printed version:

Bracamontes-Ramirez, J., and B.R. Sutherland (2024) Transient internal wave excitation of resonant modes in a density staircase. Phys. Rev. Fluids, 9(6), 064801, doi:10.1103/PhysRevFluids.9.064801.

# 2 Transient internal wave excitation of resonant modes in a density staircase

## 2.1 Theory

In the following four subsections, we first describe the background density profile of the staircase, and then give general solutions for the vertical structure of disturbances in the staircase. We then specifically review the theory (Sutherland, 2016) of internal wave tunneling across a staircase that predicts the transmission coefficient as it depends upon the horizontal wavenumber and frequency of the incident wave. From this prediction we derive the methodology to determine numerically the dispersion relation for "global modes" for which there is pure transmission at non-zero horizontal wavenumber. We then consider the natural modes of the density staircase, giving an expression from which the dispersion relation of vertical modes can be derived. Showing that the global modes and natural modes are near-resonant, we examine the excitation of the natural modes that are transiently forced by incident waves with wavenumber and frequency near that of the global modes.

## 2.2 Problem setup

In setting up the density profile for the staircase, we imagine the fluid in the absence of a staircase is uniformly stratified with constant buoyancy frequency $N_0$. We now suppose that this profile is uniformly mixed across $J$ steps, each of depth $L$, with the staircase extending between $z = 0$ and $z = -JL$. The corresponding background density profile is thus given by

$$\bar{\rho}(z) = \begin{cases} \rho_0 \left(1 - \frac{\Delta\rho}{\rho_0}\frac{z}{L}\right), & z > 0 \\ \rho_0 \left(1 + \left(j - \frac{1}{2}\right)\frac{\Delta\rho}{\rho_0}\right), & -jL < z < -(j-1)L, \quad j = 1, 2, \ldots, J \\ \rho_0 \left(1 - \frac{\Delta\rho}{\rho_0}\frac{z}{L}\right), & z < -J\,L \end{cases} \tag{2.1}$$

Here, $\rho_0 = \rho(0^+)$ represents the characteristic density, located just above the top step. Above and below the staircase, the (constant) squared buoyancy frequency is $N_0^2 \equiv -(g/\rho_0)d\bar{\rho}/dz = g'L$, in which $g' = g\Delta\rho/\rho_0$ is the reduced gravity. This sets the size of the density jumps $\Delta\rho$ within the staircase for given step depth, $L$. The

density jump at the top and bottom step is $\Delta\rho/2$.

The fluid is assumed to be inviscid and Boussinesq, and the disturbances are assumed to be small-amplitude and two-dimensional with structure in the $x$-$z$ plane. For simplicity, the influence of background rotation is ignored. Under these approximations, then general evolution equation is given by

$$\left[\frac{\partial^2}{\partial t^2}\nabla^2 + N^2\frac{\partial^2}{\partial x^2}\right]\psi = 0, \tag{2.2}$$

in which $\psi(x,z,t)$ is the streamfunction, $\nabla^2 = \partial^2/\partial x^2 + \partial^2/\partial z^2$ is the Laplacian, and $N^2(z)$ is the buoyancy frequency. Because the coefficients of (2.2) are independent of $x$ and $t$, we can seek solutions in which the spatio-temporal structure of disturbances outside and within the staircase are horizontally periodic with wavenumber $k$ and which have (possibly complex) frequency $\omega$. A general solution can be constructed from a superposition of these waves.

The streamfunction can thus be written as $\psi(x,z,t) = \hat{\psi}(z)\exp[\imath(kx-\omega t)]$, in which it is understood that the actual streamfunction is the real part of this expression. From (2.2), the vertical structure, $\hat{\psi}$, satisfies

$$\frac{d^2\,\hat{\psi}}{dz^2} + k^2\left(\frac{N^2}{\omega^2} - 1\right)\hat{\psi} = 0. \tag{2.3}$$

Because $N = N_0$ is constant above and below the staircase and $N = 0$ within each step of the staircase, piecewise-analytic general solutions can be found for $\hat{\psi}(z)$ of the form

$$\hat{\psi}(z) = \begin{cases} A_0\, e^{\imath m z} + B_0\, e^{-\imath m z}, & \text{for } z > 0 \\ A_j\, e^{k[z+L(j-1/2)]} + B_j\, e^{-k[z+L(j-1/2)]}, & -jL < z < -(j-1)L, \quad j = 1\ldots J \\ A_{J+1}\, e^{\imath m[z+L\,J]} + B_{J+1}\, e^{-\imath m[z+L\,J]}, & \text{for } z < -J\,L. \end{cases} \tag{2.4}$$

Here, $m \equiv k\sqrt{N_0^2/\omega^2 - 1}$, represents the (positive) vertical wavenumber of waves above and below the staircase if $\omega$ is real and less than $N_0$. We will see that for natural modes of the staircase, $m$ is complex-valued. In this case, we define $m$ so that its real part is positive.

The constants $A_j$ and $B_j$ for $j = 0, \ldots J+1$ can be found by imposing continuity of vertical velocity and pressure. This amounts to requiring that $\hat{\psi}$ and $d\psi/dz = g\frac{\bar{\rho}}{\rho_0}\frac{k^2}{\omega^2}\hat{\psi}$ are continuous (e.g. see Sec 2.6.1 of Sutherland (Sutherland, 2010b)). This gives a pair of interface conditions at $z = jL$, for $j = 0, \ldots, J$, for a total of $2(J+1)$ equations. These are given in

Full solutions depend upon conditions imposed above and below the staircase. Because the sign of the vertical group velocity, $c_g$, is opposite to the sign of (the real part of) $m$, the coefficients $A_0$ and $A_{J+1}$ correspond to the amplitudes of downward propagating waves, whereas $B_0$ and $B_{J+1}$ correspond to the amplitudes of upward propagating waves. For the tunneling problem with incident waves propagating downward from above, we take $B_{J+1} = 0$. For the problem of modes, we require waves to propagate away from the staircase so that $A_0 = B_{J+1} = 0$.

### 2.2.1 Tunneling of plane waves

The theory for the transmission of incident plane waves across a density staircase was developed by Sutherland (Sutherland, 2016). That study included the effects of rotation and allowed for steps having small random variations in the step size. Here we review the essential results of (Sutherland, 2016), focusing on the analytic solutions where the step size, $L$, is same for all steps, and we ignore background rotation.

Setting $B_{J+1} = 0$ in 2.4, and applying the interface conditions gives $2J+2$ equations in $2J+3$ unknowns. These can be combined to get an explicit expression for $A_0$ in terms of $A_{J+1}$:

$$A_0 = \frac{i}{4M}\big(a_+, a_-\big)\,\mathcal{C}^{J-1}\begin{pmatrix} a_+ \\ a_- \end{pmatrix} A_{J+1}, \tag{2.5}$$

in which the left and right vectors have components

$$a_\pm \equiv \Delta^{\pm 1/2}\,[1 \mp \Gamma \pm iM], \tag{2.6}$$

the matrix $\mathcal{C}$ is

$$\mathcal{C} = \begin{pmatrix} \Delta(1-\Gamma) & -\Gamma \\ \Gamma & \Delta^{-1}(1+\Gamma) \end{pmatrix}, \tag{2.7}$$

and we have defined the following nondimensional quantities:

$$\Delta \equiv \exp(kL), \quad M \equiv m/k = \sqrt{\frac{N_0^2}{\omega^2} - 1}, \quad \Gamma \equiv \frac{g' k^2}{2k\ \omega^2} = \frac{1}{2} kL(M^2 + 1). \tag{2.8}$$

In the expressions for $M$ and $\Gamma$ we have used the dispersion relation where $N^2 = N_0^2$ is constant: $\omega^2 = N_0^2 k^2/(k^2 + m^2)$.

An analytic solution to (2.5) is found by diagonalizing $\mathcal{C}$ in terms of its eigenvalues, $\lambda_\pm$. From this solution an expression for the transmission coefficient is found: $T = |A_{J+1}/A_0|^2$, which represents the fraction of the energy (or, equivalently, energy flux) associated with the incident waves that is transmitted below the staircase. Explicitly this is given by (Sutherland, 2016)

$$T = \frac{1}{1 + X^2}, \text{ with } X \equiv \frac{\delta_+ \Gamma_+ \ + \ \delta_- \Gamma_- \ + \ 2\delta_0 \Gamma |\Lambda_-|}{4M|b_0|}, \tag{2.9}$$

in which

$$\delta_\pm \equiv \Delta^\pm \left[(1 \mp \Gamma)^2 + M^2\right], \quad \delta_0 \equiv \Gamma^2 - 1 + M^2, \tag{2.10}$$

$$\Gamma_\pm = b_- |\Lambda_-| \ \pm \ |b_0| \Lambda_+, \quad \Lambda_\pm = \frac{1}{2}\left[\lambda_+^{J-1} \pm \lambda_-^{J-1}\right], \tag{2.11}$$

$$\lambda_\pm = b_+ \pm b_0, \quad b_\pm \equiv \frac{1}{2}\left[\Delta\,(1 - \Gamma) \pm \Delta^{-1}\,(1 + \Gamma)\right], \quad b_0 \equiv \sqrt{b_+^2 - 1}. \tag{2.12}$$

Examination of $T$ shows that the transition between strong and weak transmission occurs for (Sutherland, 2016)

$$\omega_c/N_0 = [(kL/2)\tanh(kL/2)]^{1/2} \simeq kL/2, \tag{2.13}$$

in which the last expression gives the approximation for $kL \ll 1$. Alternately, given a forcing frequency $\omega_0 \ll N_0$, the critical transition occurs for relative horizontal wavenumber

$$k_c L = 2\omega_0/N_0. \tag{2.14}$$

Mathematically, the transition corresponds to the condition, $b_0 = 0$, delineating the boundary between real and complex values of $\lambda_\pm$. For frequencies lower than $\omega_c$ ($\lambda_\pm$

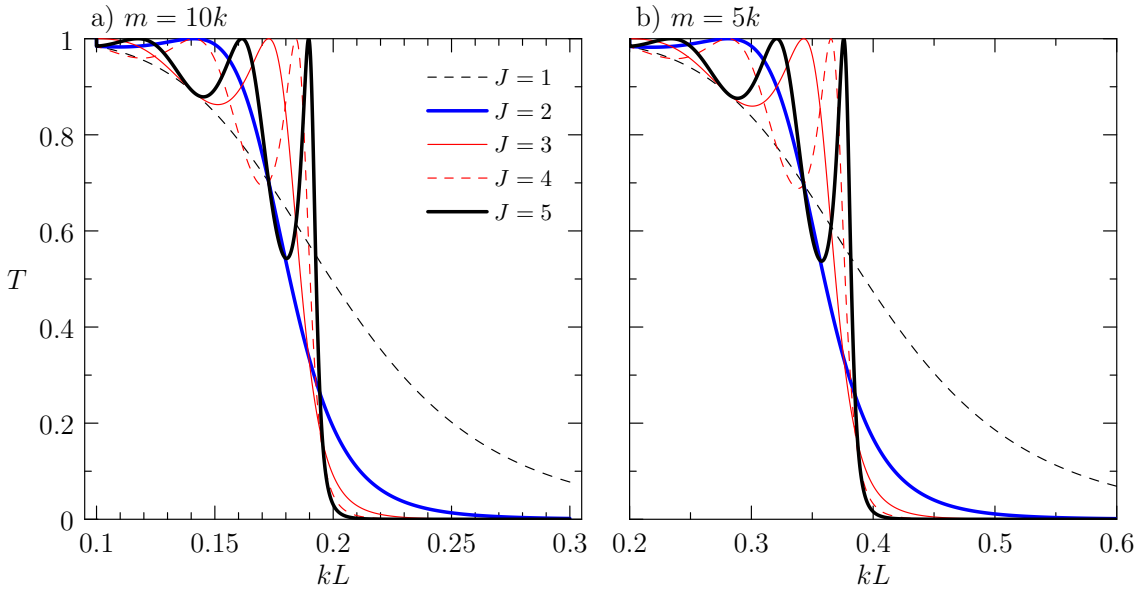


Figure 2.1: Predicted transmission coefficient as it depends on the relative step size, $kL$, and the number of steps, $J$, for incident plane waves with a) $m = 10k$ ($\omega/N_0 \simeq 0.0995$) and b) $m = 5k$ ($\omega/N_0 \simeq 0.1961$). The different line styles in both plots represent the number of steps, as indicated in a).

complex), a series of transmission spikes occurs where $T = 1$. If the staircase has $J$ steps, there are $J$ transmission spikes. This is shown, for example in Figure 2.1.

In astrophysics, the transmission spikes are said to correspond to "global (g-)modes" (Belyaev et al., 2015; André et al., 2017). The dispersion relation of these modes can be found by setting $X = 0$ in (2.9), which is equivalent to setting $B_0 = 0$ (and hence $|A_{J+1}| = A_0$) in (2.4) and applying the interface conditions to get an eigenvalue problem. In the expression for $X$, it is readily shown that $|\Lambda_-|/|b_0|$ and $\Lambda_+$ are polynomials in $b_0^2$. Hence $4MX$ can be written as a polynomial in $M^2$, whose roots can be found numerically for given $kL$ (e.g. with MATLAB's "vpasolve" function). The corresponding frequency is then found from $\omega/N_0 = (1 + M^2)^{-1/2}$.

The resulting dispersion relations for the global modes are plotted in Figures 2.2a,c) for cases with $J = 2$ and 5 steps. The lowest mode has $\omega/N_0$ nearly constant with $kL$ for small $kL$. This mode arises from the interfaces at $z = 0$ and $-JL$. For $J > 1$, higher modes exhibit a near-linear dependence upon $kL$ for small $kL$, with the highest mode having frequency moderately larger than the critical frequency $\omega_c$, given by (2.13).

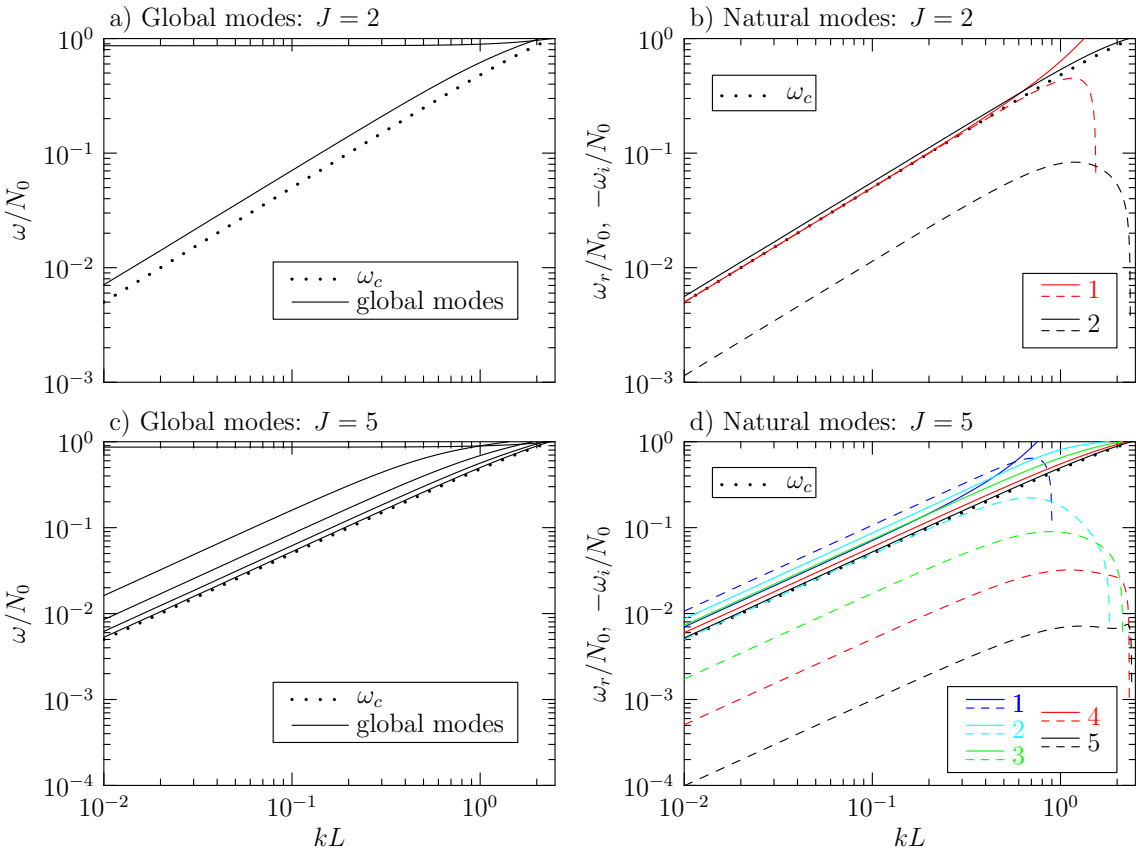


Figure 2.2: Log-log plots of the dispersion relation for a,c) global modes and b,d) natural modes of a density staircase having a,b) $J = 2$ steps and c,d) $J = 5$ steps. In all four plots, the dotted black line is the critical frequency $\omega_c$, given by (2.13). The solid black lines in a,c) represent different global modes. In b,d) the solid and dashed lines correspond, respectively, to the real and (negative) imaginary part of the frequency. The colours indicate the mode number, as shown in the legends, with the highest vertical mode (lowest frequency at fixed $kL$) drawn as solid and dashed black lines.

### 2.2.2 Natural modes of a $J$-step staircase

The dispersion relation corresponding to the natural modes of a density staircase is found by setting $A_0 = B_{J+1} = 0$ in (2.4) and applying the interface conditions to get an eigenvalue problem. The resulting eigenvalue problem can be written as a pair of equations for $B_0$ and $A_{J+1}$:

$$\begin{pmatrix} a_- \\ a_+ \end{pmatrix} B_0 = \mathcal{C}^{J-1} \begin{pmatrix} a_+ \\ a_- \end{pmatrix} A_{J+1}, \tag{2.15}$$

in which $a_\pm$ is given by (2.6) and the matrix $\mathcal{C}$ is given by (2.7). Casting this as a matrix eigenvalue problem for the eigenvector $(B_0, A_{J+1})^T$, and setting the matrix determinant to zero gives

$$[-2\Gamma a_+ a_- + b_-(a_+^2 + a_-^2)]\,(\Lambda_0/b_0) + (a_+^2 - a_-^2)\,\Lambda_+ = 0. \tag{2.16}$$

with $\Gamma$, $\Lambda_\pm$, $b_-$ and $b_0$ defined by (2.8), (2.11) and (2.12).

As with the problem of finding global modes, $\Lambda_+$ and $\Lambda_-/b_0$ are expressions involving $b_0^2$. Hence (2.16) reduces to the problem of finding the roots of a polynomial in $M^2$. Unlike the global modes, the eigenvalues, $m = Mk$, are complex, as are the corresponding frequencies $\omega = N_0/(1+M^2)^{1/2}$. This result can be contrasted with the study of Belyaev et al (Belyaev et al., 2015) who found only real-valued frequencies in their dispersion relation for natural modes in a staircase. Although they assumed the fluid was a compressible gas, the main reason for having real frequencies is likely because they examined modes in an effectively infinite staircase with periodic upper and lower boundary conditions. These boundary conditions ($A_0 = A_{J+1}$ and $B_0 = B_{J+1}$) neglected the physics of energy propagation escaping a finite-depth staircase (which we will show leads to exponentially growing wave amplitudes).

Taking eigenvalues with the real part of $M$ to be positive, we find the complex frequencies have positive real parts, $\omega_r$, and negative imaginary parts, $\omega_i$. Hence the modes decay exponentially in time with an e-folding time $1/|\omega_i|$, as is expected for modes that continuously lose energy to upward and downward propagating internal waves, respectively above and below the staircase.

The dispersion relations of modes in staircases with $J = 2$ and $J = 5$ are plotted in Fig. 2.2b,d). Like the global modes, the largest vertical mode (with lowest frequency at fixed $kL$) has frequency moderately larger than the critical frequency, $\omega_c$, and also has the lowest magnitude of the decay rate, $|\omega_i|$.

The overlap between the dispersion relation of global modes and the real part of the dispersion relation of the natural modes with large vertical mode number was anticipated, but not explicitly derived by (Sutherland, 2016): higher transmission is expected when incident plane waves are near-resonant with natural modes of the

system. However, the resonance is never exact because the natural modes are not steady, but decay in time. Furthermore, the imaginary part of the eigenvalues of $M = (m_r + im_i)/k$ for the modes is negative. Thus, while the vertical structure of the modes oscillate above and below the staircase with vertical wavenumber $m_r$, they also grow exponentially with e-folding scale $1/|m_i|$. This is a result of the normal mode solutions representing an effectively infinitely large disturbance in the staircase as $t \to -\infty$ that propagates vertically away from the staircase at the group velocity as the disturbance in the staircase decays exponentially in time.

We are particularly interested in the dependence upon the number of steps, $J$, of the decay rate of the highest vertical mode. An approximate analytic expression can be found in the limit $kL \ll 1$ and $J \gg 1$. Because the highest vertical mode is near the critical transition, $\omega_c/N_0 \simeq kL/2$, we require $\omega/N_0 \ll 1$. Hence, using $\omega/N_0 = (M^2+1)^{-1/2}$, we must have $|M| \gg 1$ and $\omega/N_0 \simeq 1/M = k/m$. Explicitly, we suppose the relative vertical wavenumber of the highest mode can be written as $\tilde{m} \equiv mL = 2 - \epsilon$, in which $\epsilon$ is complex-valued and $|\epsilon| \ll 1$. The perturbation calculation, described in Appendix A, gives $\epsilon \simeq (3/2)J^{-2} - 3iJ^{-3}$. From this it follows that the approximate dispersion relation of the highest vertical mode is

$$\frac{\omega}{N_0} \simeq \frac{kL}{2}\left(1 + \frac{3}{4}J^{-2} - \frac{3}{2}i\,J^{-3}\right). \tag{2.17}$$

In particular, this shows that the decay rate of the mode decreases with the number of steps as $J^{-3}$. The predicted e-folding time scale, $\tau_e$, associated with the decay of energy is given by

$$N_0\tau_e = \frac{2}{3}\frac{1}{kL}J^3 \tag{2.18}$$

## 2.3 Numerical Simulations

We use a numerical code that solves the fully nonlinear two-dimensional, Boussinesq equations cast in terms of the spanwise vorticity, $\zeta \equiv \partial_z u - \partial_x w$, and buoyancy, $b$:

$$\frac{D\zeta}{Dt} = -\frac{\partial b}{\partial x} + \nu\mathcal{D}_\zeta, \qquad \frac{Db}{Dt} = -N^2 w + \kappa\mathcal{D}_b, \tag{2.19}$$

in which $D/D_t = \partial_t + \vec{u}\cdot\nabla$ is the material derivative, $\vec{u} = (u, w)$ is the velocity with horizontal ($x$) and vertical ($z$) components $u$ and $w$, respectively, and $\nabla = (\partial_x, \partial_z)$. The fields are discretized vertically on an evenly spaced grid and are represented horizontally in Fourier space. The effect of viscosity and diffusion is represented by the operator $\mathcal{D}$. This is the Laplacian operator in horizontal Fourier space, $-k_n^2 + \partial_{zz}$, except that it operates only upon horizontal wavenumbers, $k_n$, above a specified cut-off taken to be $k_\star = 32k$. In this way diffusion acts to damp small-scale numerical noise, but does not act upon the waves associated with the wavepacket, having horizontal wavenumber $k$, and the modes it excites. The viscous and diffusion coefficients are taken to be $\nu = \kappa = 100000 N_0 k^{-2}$. At each time step, the streamfunction is found through inversion of the Laplacian equation $\nabla^2\psi = -\zeta$. From this the velocity components are found by $u = -\partial_z\psi$ and $w = \partial_x\psi$.

In the idealized staircase used by our theory, the density jumps discontinuously at each step. So that $N^2$ is finite, but still representative of rapid density jumps, we define a background density profile, $\bar{\rho(z)}$, similar to (2.1) but with continuously varying density that increases with depth across each step over a thickness scale, typically taken to be $\sigma_N = 0.01L$. For a staircase with $J$ steps, the density profile is given explicitly by

$$\begin{aligned}
\bar{\rho}(z) \;=\; & \rho_0 - \frac{1}{2}\rho_0\frac{N_0^2}{g}[z + \sigma_N \ln\cosh(z/\sigma_N)] + \frac{1}{2}\Delta\rho[1 - \tanh(z/\sigma_N)] \\
& + \sum_{j=1}^{J-1} \Delta\rho[1 - \tanh((z + jL)/\sigma_N)] \\
& + \frac{1}{2}\rho_0\frac{N_0^2}{g}\Big[ - z + \sigma_N \ln\left(\frac{\cosh((z+JL)/\sigma_N)}{\cosh(JL/\sigma_N)}\right)\Big] \\
& + \frac{1}{2}\Delta\rho\Big[1 - \tanh\left(\frac{z+JL}{\sigma_N}\right)\Big]. \qquad (2.20)
\end{aligned}$$

Using $g' = g\Delta\rho/\rho_0 = N_0^2 L$, the corresponding $N^2$ profile is given by

$$\begin{aligned}
N^2(z)/N_0^2 \;=\; & \frac{1}{2}\Big[1 + \tanh(z/\sigma_N) + \frac{1}{2}\frac{L}{\sigma_N}\operatorname{sech}^2(z/\sigma_N)\Big] \\
& + \sum_{j=1}^{J-1} \frac{1}{2}\frac{L}{\sigma_N}\operatorname{sech}^2\Big((z + jL)/\sigma_N\Big) \\
& + \frac{1}{2}\Big[1 - \tanh\Big((z+JL)/\sigma_N\Big) + \frac{1}{2}\frac{L}{\sigma_N}\operatorname{sech}^2\Big((z+jL)/\sigma_N\Big)\Big] \qquad (2.21)
\end{aligned}$$

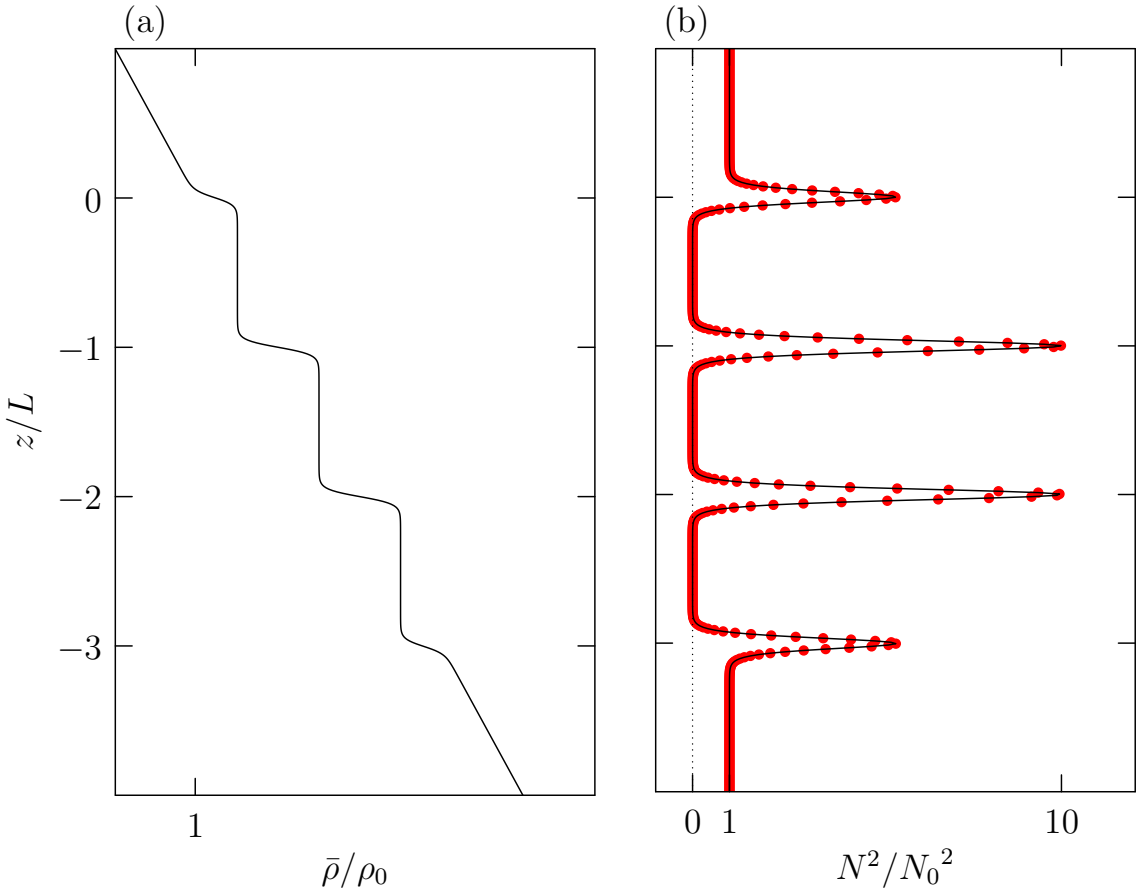


Figure 2.3: Profiles used in numerical simulations of a) background density $\bar{\rho}(z)$ and b) background stratification $N^2(z)$, for $J = 3$. The red dots in b) indicate the vertical resolution of the numerical model.

These profiles are plotted for the case $J = 3$ in Fig 2.3.

Superimposed on the background stratification, the simulations were initialized with a horizontally periodic, vertically compact quasi-monochromatic wavepacket having a Gaussian amplitude envelope centered at $z = z_0$. In terms of the streamfunction the wavepacket is defined by,

$$\psi(x, z, t = 0) = A_0 \exp\left[-\frac{1}{2}\left(\frac{z - z_0}{\sigma_0}\right)^2\right] \cos(kx + m_0 z) \tag{2.22}$$

in which $k$ and $m_0$ respectively, are the horizontal and peak vertical wavenumbers, $A_0$ is the maximum streamfunction amplitude, and $\sigma_0$ is the vertical extent of the wavepacket. In most simulations we set $\sigma_0 m_0 = 10$, but also explore cases with $\sigma_0 m_0 = 5$ and 20. Because $\sigma_0 m_0 \gg 1$, the wavepacket is quasi-monochromatic

with peak frequency $\omega_0 = N_0 k/(k^2 + m_0^2)^{1/2}$. The initial wavepacket is centered at $z_0 = 10k^{-1} \gg \sigma_0$ so that the wavepacket has negligible amplitude within the staircase at the start of the simulation. From the polarization relations for monochromatic waves, the initial spanwise vorticity and buoyancy are specified in terms of the streamfunction by $\zeta|_{t=0} = (k^2 + m_0^2)\,\psi|_{t=0}$ and $b|_{t=0} = N_0^2(k/\omega_0)\,\psi|_{t=0}$,

In our simulations there was no mean background flow. Nevertheless, we computed the Eulerian-induced mean flow, $u_E$, generated by the wavepacket and superimposed this on the background. Explicitly, the wave-induced mean flow is defined in terms of $\zeta$ and $b$ by $u_E(z, t = 0) = \langle \zeta\ b \rangle / N_0^2$ (e.g. see Sutherland (Sutherland, 2010b)). The presence of the induced flow is included by adding $-du_E/dz$ to the background vorticity field. Because the waves are small amplitude, the induced mean flow has no influence upon the wave propagation. However, it is included to avoid what would emerge as a negative jet $-u_E(z, t = 0)$ at the initial location of the wavepacket and, consequently, would give rise to the unphysical presence of energy above the staircase.

The simulations were performed in a horizontally periodic domain with one horizontal wavelength of the incident wavepacket spanning the horizontal extent. The vertical extent needed to be sufficiently tall for the disturbance in the staircase to reach negligibly small amplitude before the transmitted and reflected waves reached the top and bottom of the domain, respectively. Thus we set $-H \leq z \leq H$, with $H = 60L$. In order to resolve the spikes in $N^2$, high vertical resolution was required with typical simulations having $2^{16}$ points in the vertical, giving a vertical resolution of $\Delta z \simeq 0.0018L$. This resolution is indicated by the red dots in Fig. 2.3b. The horizontal field was represented by a superposition of 64 Fourier modes. Simulations were advanced in time using a leapfrog scheme for advective terms, with an Euler backstep taken every 20 steps. Each time step had a resolution of $\Delta t = 0.05N_0^{-1}$. Simulations performed with higher resolution and shorter time-steps show that the measurements of relative energy above, below and within the staircase are accurate to three-digits.

In all simulations the time scale was set so that $N_0 = 1$ and the length scale was set so that $k = 1$. Nonetheless, the results are presented with these scales being explicitly

represented. We conducted a range of simulations with the number of steps in the staircase ranging from $J = 1$ to 10. The relative vertical wavenumber of the incident wavepacket, $m_0/k$, was 5 or 10, corresponding to $\omega_0/N_0 \simeq 0.2$ or 0.1, respectively. According to (2.13), the predicted transition between weak and strong transmission with $kL \ll 1$ occurs for $\omega_c \simeq kL/2$. To explore this transition, in simulations with $m_0/k = 5$, $kL$ ranged from 0.2 to 0.55; in simulations with $m_0/k = 10$, $kL$ ranged from 0.1 to 0.3.

We also conducted a range of simulations varying the initial wavepacket amplitude. In terms of the initial vertical displacement amplitude, $\mathcal{A}_{\xi 0} = -(k/\omega)\, A_0$, our simulations had amplitudes with $\mathcal{A}_{\xi 0} k$ ranging from 0.001 to 0.01. In this range there was no significant quantitative difference between simulation results in terms of transmission and reflection diagnostics. Hence, we report here only upon simulations with $\mathcal{A}_{\xi 0} k = 0.001$. The sensitivity of results to the interface thickness was examined by performing some simulations with half the interface thickness ($\sigma_N = 0.005L$) and double the vertical resolution. No significant quantitative differences to our results were found.

The analysis of our simulations focused upon the evolution of energy over time above, within, and below the staircase. At each time, we calculated the total horizontally averaged, vertically integrated energy, $E_{\text{total}}$. This was partitioned into the energy above, within and below the staircase respectively by the integrals

$$E_r = \int_{z=3\sigma_N}^{H} (\text{KE} + \text{PE})\; dz \tag{2.23}$$

$$E_s = \int_{z=-JL-3\sigma_N}^{3\sigma_N} (\text{KE} + \text{PE})\; dz, \tag{2.24}$$

$$E_t = \int_{z=-H}^{-JL-3\sigma_N} (\text{KE} + \text{PE})\; dz \tag{2.25}$$

in which $\text{KE}(z,t) = (1/2)\,\langle u^2 + w^2 \rangle$ is the horizontally averaged kinetic energy per mass and $\text{PE}(z,t) = (1/2)\,\langle b^2 \rangle\, /N^2$ is the horizontally averaged available potential energy. Within the staircase $||b|| \to 0$ as $N \to 0$ such that $\text{PE} \to 0$. Hence, in calculating the integral of PE in (2.24), we do so only where $N^2$ exceeds a threshold of 0.001.

From the energy integrals, we compute the time-evolving transmission coefficient ($T(t)$) and reflection coefficient ($R(t)$) as well as the relative energy in the staircase ($S(t)$):

$$T(t) = \frac{E_t}{E_{\text{total}}}, \quad R(t) = \frac{E_r}{E_{\text{total}}}, \quad S(t) = \frac{E_s}{E_{\text{total}}}. \tag{2.26}$$

The duration of the simulations varied primarily based on the vertical group velocity of the incident wavepacket and the number of steps, $J$, in the staircase. As we show, for larger $J$, energy remains trapped in the staircase for longer times, requiring longer simulations. In most simulations, the final time was set so that the relative energy within the staircase, $S(t)$, fell below 0.001 after reaching its peak. In the simulation with $J = 10$, the waves reached the top and bottom of the domain before this threshold was reached. These simulations were terminated at time $6590N_0^{-1}$ when $S(t) \simeq 0.0065$.

We will show that energy persists for longer times in a staircase with a larger number of steps due to the excitation of modes with long e-folding decay times. To quantify this, we constructed a log-plot of the energy within staircase, $\ln(S(t))$ versus $t$, and found the slope of the best-fit line through over late times for which $S \leq 0.01$. The slope determined the e-folding energy decay time, $\tau_e$, within the staircase, which could be compared with the predicted decay time, $2/\tau_j$, of each mode.

## 2.4 Results

We begin with a qualitative examination of wavepacket tunnelling in a simulation of an initial wavepacket having $m_0 = 10k$ being incident upon a staircase with $J = 5$ steps. The peak frequency of the incident wave is $\omega_0 \simeq 0.0995$. We examine the case with $kL = 0.2$, which corresponds to waves near the transition between weak and strong transmission, given by (2.14). This wavenumber is moderately larger than the predicted largest relative wavenumber of the transmission spikes, which occurs at $kL \simeq 0.19$ (see Fig. 2.1a). We note that, for $kL = 0.2$, the predicted transmission coefficient is $\simeq 0.5$ for $J = 1$, but is predicted to be small for $J = 5$.

Snapshots of the wavepacket evolution at three times are shown in Fig. 2.4. The structure of the waves is represented here in terms of the horizontal velocity field

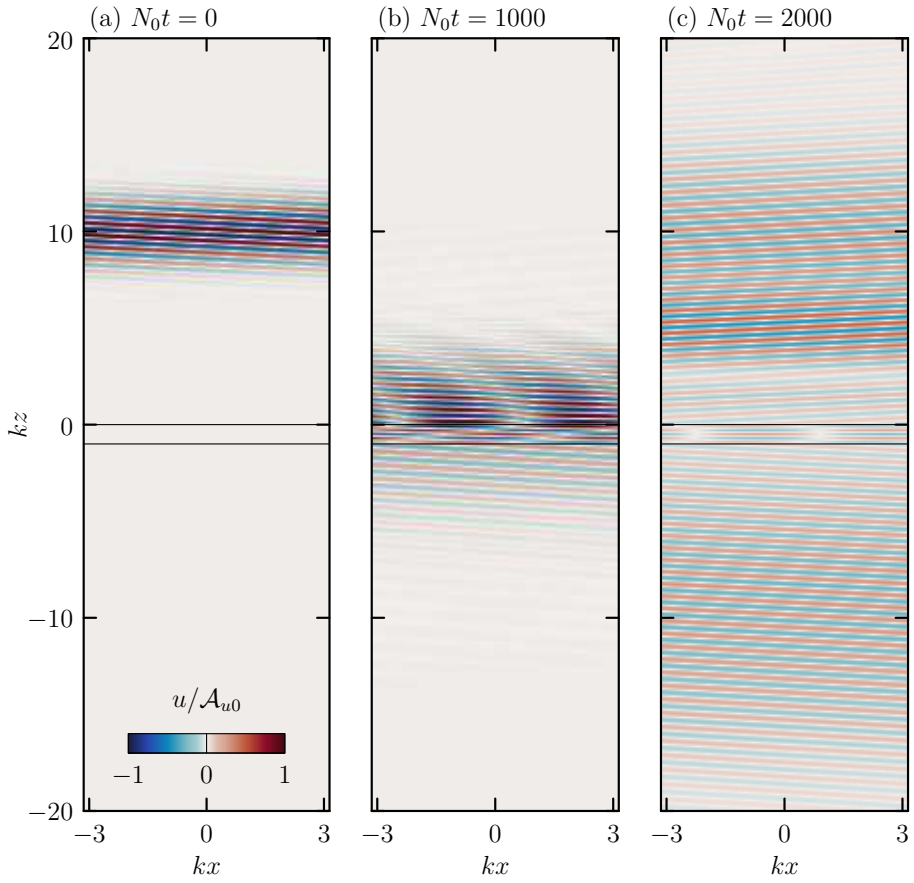


Figure 2.4: From a simulation with $m_0 = 10k$, $kL = 0.2$ and $J = 5$, snapshots of horizontal velocity at times a) $t = 0$, b) $1000N_0^{-1}$ and c) $2000N_0^{-1}$. The colours in all three plots show the horizontal velocity normalized by the initial horizontal velocity amplitude $\mathcal{A}_{u0}$, with values indicated by the scale in a). The horizontal lines at $z = 0$ and $z = -1$ indicate the levels at the top and bottom of the staircase, respectively.

normalized by the initial amplitude, $\mathcal{A}_{u0} = m_0 A_0$. Initially the wavepacket is centered at $z_0 = 10k^{-1}$. The width of the envelope, $10/m_0 = k^{-1}$, is much smaller than $z_0$ so that the signal of the initial wavepacket within that staircase is negligible.

The vertical group velocity of the wavepacket is $\simeq -N_0 k/m_0^2$. And so the estimated time for the center of the wavepacket to reach the top of the staircase (at $z = 0$) is $z_0 m_0^2/(kN_0) = 1000/N_0$. This is the time shown in Fig. 2.4b. At this time, the leading flank of the incident wavepacket has partially transmitted through the staircase, as evident from the pattern of downward propagating waves below $z = -JL = -k^{-1}$. Above the top of the staircase the disturbance field is a superposition of the incident trailing flank of the wavepacket and partially reflected upward propagating waves.

At $N_0 t = 2000$ (Fig. 2.4c), the transmitted waves below the staircase and the reflected waves above the staircase are broadly distributed in the vertical, but disturbances within the staircase are non-negligible. This simulation thus gives qualitative evidence for the excitation of natural modes of the staircase by the traversing incident wavepacket.

To illustrate the impact of the incident wave upon disturbances within the staircase, Fig. 2.5a shows a close-up view of the staircase region at time $N_0 t = 2000$, corresponding to Fig. 2.4c. Near-monochromatic waves are evident above and below the staircase by phase lines having approximately constant slope. In contrast, disturbances within the staircase have a standing wave pattern, evident both in the horizontal velocity field and isopycnal displacements. The latter are found in terms of the buoyancy field at the center of each interface by computing $\xi = -b/N^2$. The isopycnal displacements exhibit an alternating varicose pattern associated with bulging and pinching contours. As our energy analysis below demonstrates, the disturbances within and near the staircase correspond to a trapped mode that emits internal waves above and below the staircase as the amplitude of disturbances with the staircase decay exponentially in time.

By contrast, in Fig. 2.5b we show a snapshot of the horizontal velocity field and isopycnal displacements from a simulation with $J = 5$ and $kL = 0.2$ but with $m_0 = 5k$. Because the vertical group velocity of the incident wavepacket is approximately 4 times larger than the wavepacket with $m_0 = 10k$, we show the snapshot at time $500 N_0^{-1}$, which is one quarter of the time of the snapshot shown in Fig. 2.5a. For this simulation, tunnelling theory for plane waves predicts near-perfect transmission of the wavepacket across the staircase. This is evident in the simulation which shows downward-sloping phase lines above and below the staircase, corresponding to downward propagating waves. Although the phase lines are vertical within each step, the phase shift across each interface corresponds to the expected change for waves unimpeded by the staircase. In a simulation with $m_0 = 5k$ but $kL = 0.4$, which is close to the transition wavenumber, we once again observe the standing wave pattern of horizontal velocity and isopycnal displacements as in Fig. 2.5a (not shown).

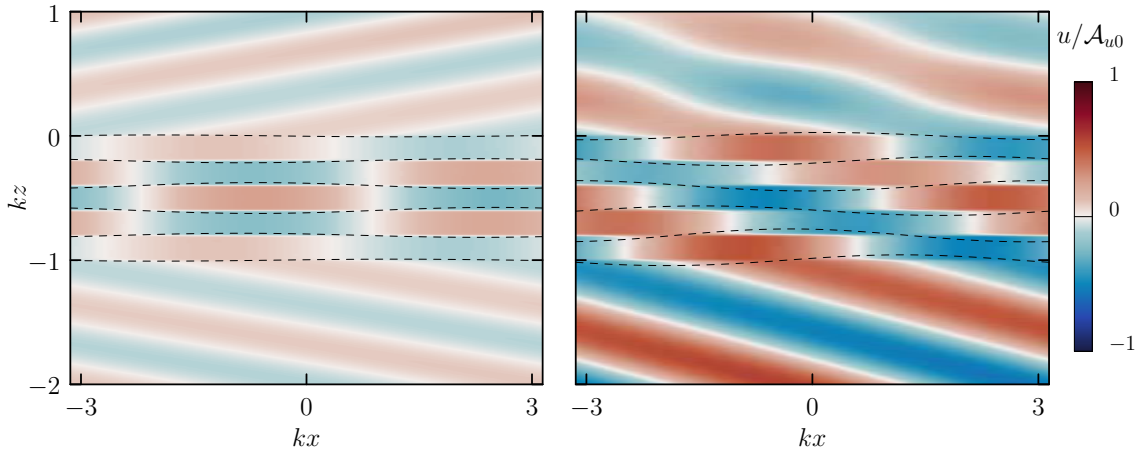


Figure 2.5: Horizontal velocity field and isopycnal displacements at each density interface in simulations with $J = 5$, $kL = 0.2$ and a) $m_0 = 10k$ at time $t = 2000\, N_0^{-1}$ and b) $m_0 = 5k$ at time $t = 500\, N_0^{-1}$. The plot in a) corresponds to the snapshot shown in in Fig. 2.4c, but focused on the vertical region about the staircase situated between $-1 \leq kz \leq 0$. The dashed lines show the vertical displacement of isopycnals at the center of each interface (at $z = -jL = -0.2j\, k^{-1}$, $j = 0 \ldots 5$). For clarity, the displacements have been magnified by a factor of 100 in a) and by a factor 20 in b).

During each simulation, we computed the energy above, below and within the staircase, as given by (2.26). Here we show the results for three simulations, all with $m_0/k = 10$ and $kL = 0.2$ but with different numbers of steps: $J = 2$, 5 and 10. The results are shown in Fig. 2.6. In all three cases, initially $R = 1$ and $T = S = 0$, corresponding to all the energy lying well above the staircase. As the center of the wavepacket reaches the staircase (in all cases around time $\simeq 1000 N_0^{-1}$), the relative energy grows below and within the staircase while decreasing above. At late times the relative energy above and below the staircase plateau to near-constant values as the energy within the staircase decays to zero.

The late-time values of the relative energy below the staircase give the simulated transmission coefficient, which may be compared with the predicted transmission of incident plane waves. This comparison is shown in Fig. 2.7 for a wide range of simulations, all having $m_0/k = 10$ and with $kL$ spanning a range about the critical transmission wavenumber at $k_c L \simeq 0.2$. The results of simulations for staircases having $J = 1$ and 2 steps are shown in Fig. 2.7a. Particularly in the case with 1 step, the predicted transmission coefficient corresponds well with the values

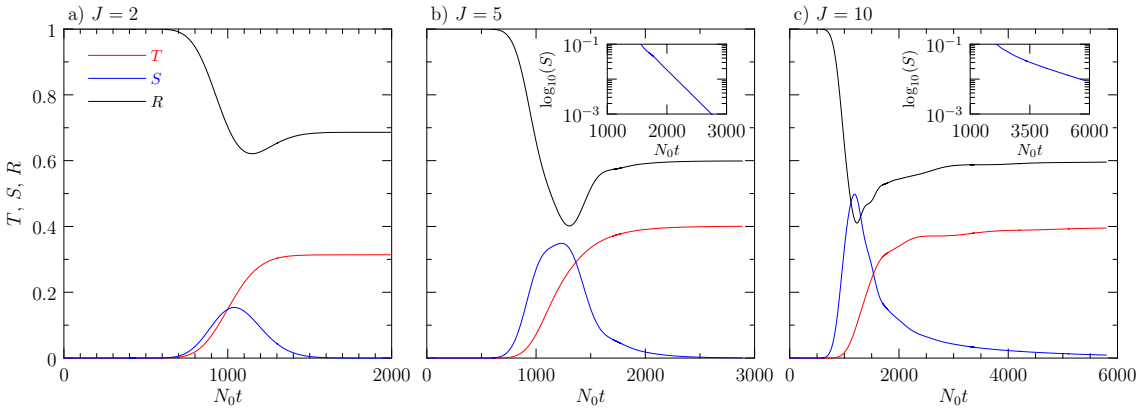


Figure 2.6: Time series of the evolution of transmitted energy, $T$ (red line), reflected energy, $R$ (black line), and energy within the staircase, $S(t)$ (blue line) in simulations with a) $J = 2$, b) $J = 5$ and c) $J = 10$ steps. The insets in b) and c) shows a log-linear plot of $S$ for times $t \geq 1000/N_0$. In all simulations $m_0 = 10k_0$ and $Lk_0 = 0.2$.

measured in simulations. In the case of 2 steps, theory moderately under-predicts the measured values for $0.18 \lesssim kL \lesssim 0.25$. In simulations with more steps, the measured transmission versus $kL$ is qualitatively different for the predicted values about $k_c L = 0.2$ (Fig. 2.7b). The presence of more steps leads to a prediction of more transmission spikes with the highest wavenumber spike having $kL$ close to, but below, $k_c L$. However, the measurements from simulations show a near monotonic decrease in $T$ with increasing $kL$. In particular, with $J = 5$ and $kL = 0.19$, theory predicts near-perfect transmission, whereas the measured transmission coefficient was 0.59. For the same number of steps but with $kL = 0.20$, theory predicts near-zero transmission, whereas the simulation measured a coefficient of 0.40. Similar behaviour is found in simulations with $m_0 = 5k$ (Fig. 2.7c) about the critical transmission wavenumber at $k_c L \simeq 0.4$.

A qualitative explanation for the lack of transmission spikes occurring in simulations can be found through closer examination of the time-evolution of relative energy within the staircase, $S(t)$, shown in Fig. 2.6. In the case with two steps (Fig. 2.6a), the growth and decay of energy within the staircase is almost symmetric about the peak, which occurs at time $\simeq 1040 N_0^{-1}$. However, in the cases with $J = 5$ and 10 (Figs. 2.6b,c), the decay of $S$ occurs over a longer time than its initial growth. The insets in Figs. 2.6b,c) plot $\log_{10}(S)$ versus time, revealing that the late time decay is nearly exponential and the decay is slower with larger $J$.

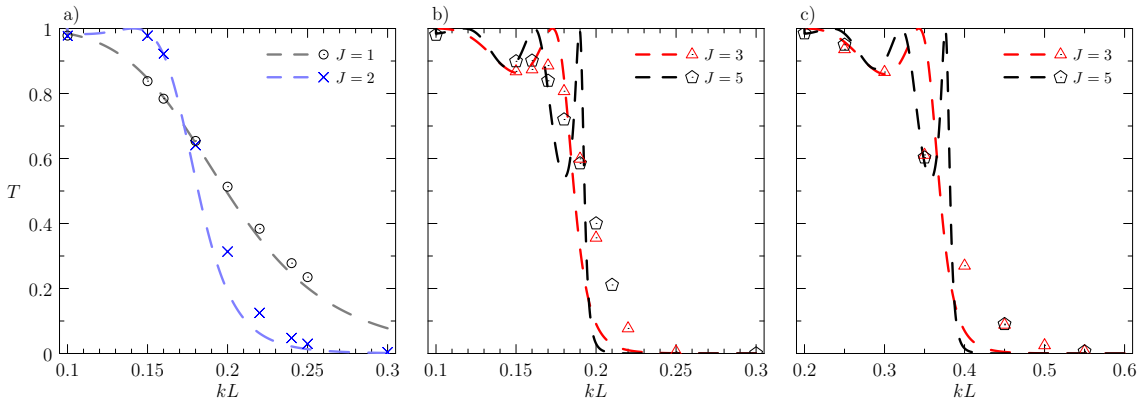


Figure 2.7: Measured and predicted transmission as a function of $kL$ in simulations with $m_0 = 10k$ and a) $J = 1$ and 2 steps and b) $J = 3$ and 5 steps, and c) with $m_0 = 5k$ and $J = 3$ and 5 steps. Dashed lines indicate the theoretical prediction for incident plane waves and symbols denote measurements from simulations, as indicated in the legends.

By finding a best-fit line through the log plots over times when $S$ falls below a threshold of 0.01, we measure the exponential decay rate and, from this, get the e-folding energy decay time-scale, $\tau_e$. This is plotted in Fig. 2.8 for a range of simulations with $J$ ranging from 1 to 10, keeping $m_0 = 10k$ and $kL = 0.2$ fixed. In simulations with $J \geq 4$, $\tau_e$ increases rapidly with increasing $J$. These measured values are compared with the predicted e-folding energy decay time associated with natural modes of the staircase, given by $\tau_e = \tau_j/2$, in which $\tau_j = -1/\omega_{ji}$ where $\omega_{ji}$ is the imaginary part of the frequency of mode-$j$ determined from the solution of the eigenvalue problem given by (2.16). The highest vertical mode has the lowest real and (magnitude of) imaginary frequency and so has the largest predicted e-folding decay time (see Fig. 2.2b,d). The predicted energy decay times of the highest modes correspond excellently with the measured values, clearly indicating that the incident wavepacket with $kL$ near the critical transition excited the highest vertical mode.

Even after the incident wavepacket partially transmitted and reflected, energy remains in this mode which then continuously transmits waves above and below the staircase as its energy decays. Thus a transmission spike in a 5-step staircase does not occur near $kL = 0.19$ because the incident wavepacket resonated near perfectly with the highest vertical mode of the staircase, which then retransmitted half the absorbed energy as upward propagating waves above the staircase. Likewise, though theory

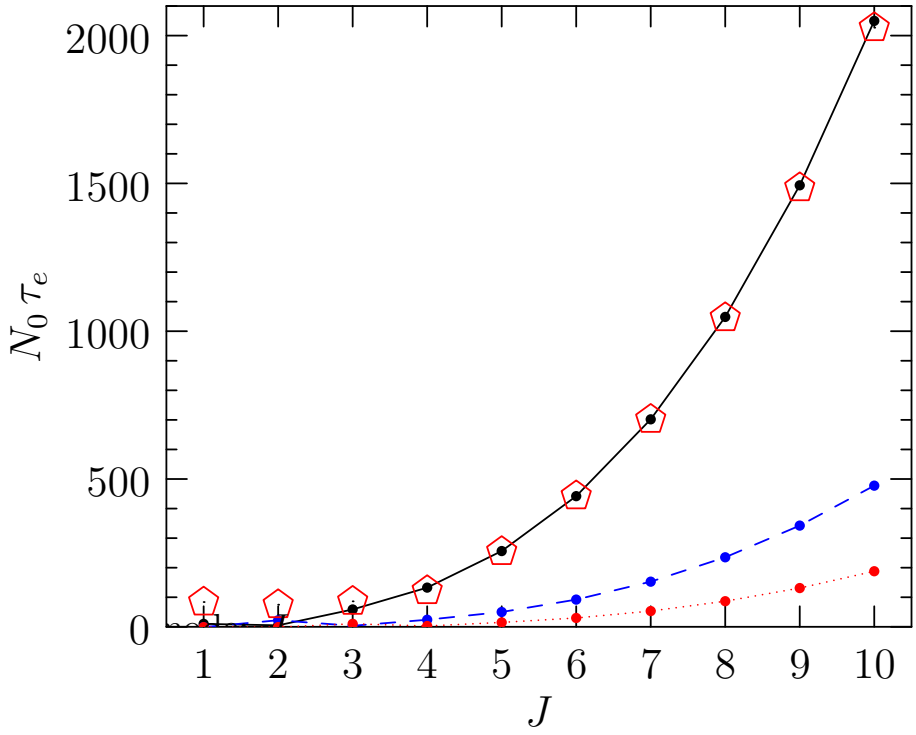


Figure 2.8: Effect of the number of steps $J$ on the e-folding decay time of energy, $\tau_e$, within the staircase at late times. Open pentagons represent measurements from simulations. The lines denote theoretical predictions based on the decay time, $1/(2\tau_j)$ of natural modes of the staircase for the highest mode ($j = J$, solid black line), second-highest mode ($j = J - 1$, blue dashed line) and the third-highest mode ($j = J - 2$, red dotted line). In all simulations $A_0 = 0.001\,k_0^{-1}$ and $m_0 = 10\,k_0$, with corresponding frequency $\omega_0 = 0.0995 N_0$.

predicts weak transmission for $kL = 0.2$, the measured transmission in simulations is large because half of the incident energy, absorbed in near-resonance with the highest vertical mode, is retransmitted as downward propagating waves below the staircase.

By plotting the results in Fig. 2.8 on log-log axes and finding a best-fit line to data with $J \geq 4$, we find that the relative energy decay time-scale increases with the number of steps as

$$N_0 \tau_e = (2.09 \pm 0.02) J^3, \tag{2.27}$$

in which the measured power law exponent, accurate to 0.1%, is consistent with the prediction (2.18).

## 2.5 Conclusions

We have performed simulations of a quasi-monochromatic wavepacket incident upon a density staircase having a different number of steps, $J$, and relative step size, $kL$. In simulations with 1 step, the transmission coefficient from the theory for incident monochromatic waves well-predicted the transmission measured in simulations. However, in simulations with a larger number of steps, the predicted occurrence of transmission spikes near the critical transition wavenumber, $k_c = 2\omega_0/(N_0 L)$, was not evident. Instead the simulations showed a near-monotonic decrease in transmission with increasing $kL$ about $k_c L$. The discrepancy between the theory for monochromatic incident waves and simulations is explained by the near-resonant excitation of the highest vertical mode of the staircase which partially extracts energy from the incident wavepacket and retransmits this energy above and below the staircase as it exponentially decays in time. The measured e-folding decay time of energy corresponded well with the predicted energy decay time for the highest vertical mode.

Due to computational cost, the simulations were necessarily restricted to the study of hydrostatic internal waves uninfluenced by rotation. For example, with $m_0 = 10k$, $\omega_0/N_0 \simeq 0.1$ which is much larger than $f/N_0$, assuming a typical value of the Coriolis parameter $f \simeq 0.01\, N_0$. In simulations with higher $m_0/k$ and lower $\omega_0/N_0$, the vertical group velocity of the incident wavepacket would have been lower, requiring prohibitively long computational times to simulate the interaction of the wavepacket with the staircase. Nonetheless, the generic nature of our results suggests they can be extended to the inertia gravity wave regime.

Our results indicate that transient effects associated with a wavepacket interacting with a density staircase should be considered if the incident wavenumber is near the critical transition value, $k_c$. Past theory has shown that $k_c$ well approximates the transition wavenumber even for finite Coriolis parameter $f_0$ provided $\omega_0 > f_0$ and $kL \ll 1$ (Sutherland, 2016). The same study showed that the critical transition wavenumber is relatively insensitive to having steps that vary in size within the staircase about a mean value $\bar{L}$. With these considerations, we tentatively use observations of a density staircase in the Arctic ocean (Timmermans et al., 2008)

to estimate conditions under which incident waves are near the critical transition. In that study, 20 steps of a staircase were observed between 240 and 290 meters depth, giving a mean step size of $\bar{L} \simeq 2.5\,\mathrm{m}$. The mean buoyancy frequency was observed to be $0.007\,\mathrm{s}^{-1}$ and $f \simeq 1.4 \times 10^{-4}\,\mathrm{s}^{-1}$ at the observed latitude around 78°N. For near-inertial incident waves ($\omega_0 \gtrsim f_0$), the critical transition occurs for $k_c \simeq 0.016\,\mathrm{m}^{-1}$, corresponding to a horizontal wavelength of $\simeq 400\,\mathrm{m}$. It is unlikely that natural processes would create inertia gravity waves with such small horizontal scale. And so our study is more relevant to higher frequency waves that are not significantly influenced by rotation. In particular, for incident waves with relative frequency $\omega_0/N_0 = 0.1$, the critical horizontal wavelength would be $\simeq 80\,\mathrm{m}$. Hence the possible near-resonant excitation of modes in the staircase would occur for internal waves that are excited by a relatively horizontally localized disturbance near the surface, for example by the motion of wind-driven ice floes in the marginal ice zone. Although this may seem restrictive, because the decay time is longer for modes in staircases with more steps the impact of incident waves upon the staircase would persist. For example, in a staircase with $J = 20$ steps, (2.18) predicts an e-folding energy decay time of $\sim 44\,\mathrm{days}$.

# Chapter 3

In this chapter we addressed the second research question. Do near-inertial turning depths exist in the Deep Canadian Basin and what are the consequences of turning depths for deep mixing?

This chapter is part of the homonymous manuscript submitted to Journal of Geophysical Research: Oceans, which is currently under review. My contributions were as follows:

I developed the research questions jointly with the co-authors. I prepared the dataset and conducted the analysis. Particularly, I collected the temperature and salinity profiles, wrote the code to calculate $N$ (King et al., 2012a) and the non-traditional approximation. I wrote the first draft of the manuscript, prepared the figures and submitted it.

The following preprint is already published and the used content in this thesis may slightly differ from the printed version:

Bracamontes-Ramírez, J., M. Walter, and M. Losch (2024) Near-inertial wave propagation in the deep Canadian Basin: Turning depths and the homogeneous deep layer. J. Geophys. Res. Oceans 129, e2023JC020228, doi:10.1029/2023JC020228.

# 3 Near-inertial wave propagation in the deep Canadian Basin: Turning depths and the homogeneous deep layer

## 3.1 Data and Methods

### 3.1.1 UDASH temperature and salinity profiles

The Unified Database for Arctic and Subarctic Hydrography (UDASH) consists of over 250 000 high-quality temperature and salinity profiles from the Arctic and Subarctic region for latitudes north of 65° N for the period 1980 to 2015. These data were measured by conductivity-temperature-depth devices (CTDs), expendable CTDs, drifting buoys, profiling floats, and expendable, digital, and mechanical bathythermographs (Behrendt et al., 2017; Behrendt et al., 2018). The mean vertical resolution of the data is 1.5 m but varies due to the range of instrumental sources between 1 cm and 693 m. In this study, we analyzed all available 21 748 profiles of temperature and salinity within the Canadian Basin, which corresponds to 10 years of data from 2005 to 2014 for the region between the 120° W and 160° W meridians and north of 70° N. Only 196 profiles (Fig. 3.1) were deep enough to have a value at some depth where $N(z)^2 \leq f^2$. These profiles represent only 0.9 % of the available data, and all are CTD casts, with precision and accuracy ranges of 0.02–0.001 °C and 0.002-0.0003 S/m for temperature and conductivity.

### 3.1.2 IBCAO bathymetry

The International Bathymetric Chart of the Arctic Ocean (IBCAO) Version 3.0 has a spatial grid resolution of 500 m. We computed the representative depth for each profile as an average of the nearest bathymetric data points (Jakobsson et al., 2012).

### 3.1.3 $N^2_{bin}$ computation and near-inertial turning depths

The deep Canadian Basin is weakly stratified with small $N^2$ between $\sim 10^{-8} - 10^{-7}\,\mathrm{s}^{-2}$. As a consequence, the noise in the estimated $N^2$ is in the same order as the relatively small Coriolis frequencies $f^2$ ($1.87 - 2.12 \times 10^{-8}\,\mathrm{s}^{-2}$ for $70 - 90°\mathrm{N}$),

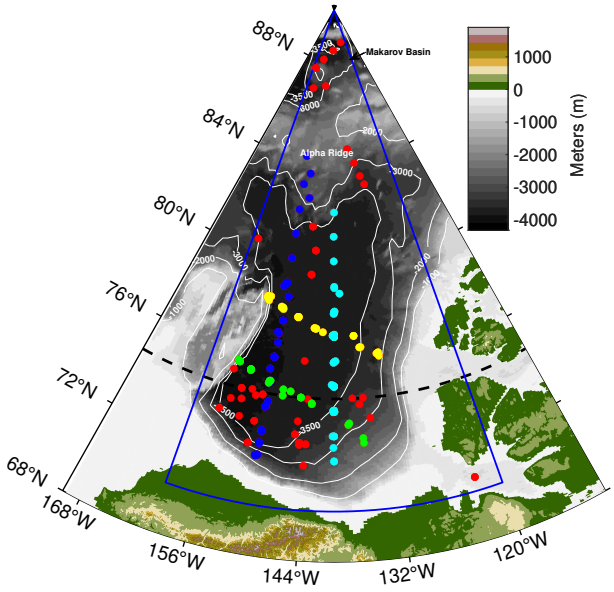


Figure 3.1: Canadian Basin bathymetry, the blue sector marks the study area. The dotted black line represents the critical latitude for the $M_2$ tide and the dots are the location of the 196 profiles used for this study. In light and dark blue, yellow, and green the profiles used for the transects shown in Fig. 3.4.

and the semidiurnal $M_2$ tidal frequency of $\omega_{M_2}$ ($\omega^2_{M_2} = 1.974 \times 10^{-8}\,\mathrm{s}^{-2}$). For the determination of turning depths, it is therefore important to minimize the noise in the $N^2$ estimation. To do so, we followed the methodology of King et al. (2012b).

This method reduces the noise by taking vertical averages of the data over depth bins. King et al. (2012b) found that a 100 m-bin is the optimal vertical width for averaging as the bin is wide enough to reduce the noise and narrow enough to preserve the $N^2$ information. Observations in the upper layers of the Canadian Basin show upward- and downward-wave energy flux with a peak within the near-inertial frequencies at vertical wavelengths of 30–50 m (D'Asaro & Morehead, 1991; Halle, 2003; Fer, 2014). Hence, the 100 m-bin width may be too large to identify turning depths for near-inertial internal waves in the upper layers, or in general to study wave motions with similar or smaller vertical scales O($\leq$100 m) since the background of $N^2$ associated with the vertical scales in which these waves propagate is smoothed (Haren & Millot, 2006; Ghaemsaidi et al., 2016b). However, we expect near-inertial internal waves will encounter a deep turning depth close to the bottom where $N^2$ is weak. For traveling waves, the vertical wavelength increases as $N^2$ decreases. We can use the following equation (Olbers, 2012), in which $m$ and $K_h$ are the vertical

and the horizontal wavenumbers, to calculate changes in the vertical wavelength of surface-generated near-inertial internal waves as they approach the bottom and roughly estimate whether a 100 m-bin is appropriate for finding turning depths for near-inertial internal waves.

$$m(z) = \pm K_h \sqrt{\frac{N^2(z) - \omega^2}{\omega^2 - f^2}} \tag{3.1}$$

Using Eq. 3.1, we estimated $K_h$ at the surface as a function of observed vertical wavelengths, 30–50 m, and $N$ =$8.73{\times}10^{-3}s^{-1}$ (5 c.p.h. ). $N$ was computed from our dataset as an average buoyancy frequency below the pycnocline. The value is consistent with previous estimates (Cole et al., 2018; Pinkel, 2005). Assuming a wave frequency $\omega = 1.05\, f$, we obtained a horizontal wavenumber $K_h = 0.105 - 6.706 \times 10^{-4}\, m^{-1}$, which is equivalent to wavelengths of 5–10 km. These wavelengths are within the values expected for the Arctic Ocean and are also within the order of the Rossby radius of deformation (Nurser & Bacon, 2014). Therefore, we used this $K_h$ to compute $m$ at 1000 m, a depth 1500 m well above $N \to \omega$ (where Eq. 3.1 no longer applies). At this depth, $N \approx 1.03 \times 10^{-3}s^{-1}$ (e.g., see in Fig. 3.2) and the vertical wavelengths increase from 30–50 m to 230–400 m. These vertical wavelengths are larger than 100 m, and they still increase as they approach the bottom and $N$ continues to decrease with depth. Therefore, we argue that the 100 m-bin averaging scale is appropriate for detecting turning depths in the deep Canadian Basin in case surface-generated near-inertial internal waves with vertical wavelengths of 30–50 m propagate to the bottom.

Prior to binning, in-situ temperature and salinity data was converted to conservative temperature ($\Theta$) and absolute salinity ($S_A$) (McDougall & Barker, 2014; McDougall & Barker, 2011). The profiles were vertically averaged in 100 m-depth bins ($\Theta_{bin}$, $S_{A\,bin}$) and spline fitted ($\langle\Theta\rangle$, $\langle S_A\rangle$) to their respective original depths. We utilized both $\langle\Theta\rangle$ and $\langle S_A\rangle$, and the original profiles $\Theta$ and $S_A$, to calculate the experimental standard deviation of the mean ($\sigma_\Theta$ and $\sigma_{S_A}$). Subsequently, we employed a Monte Carlo method to generate an ensemble of 500 synthetic profiles by adding random Gaussian noise with a half-width of $\sigma_\Theta$ and $\sigma_{S_A}$ to $\Theta_{\text{bin}}$ and $S_{A\text{bin}}$. These ensembles

were then used to compute the final averaged value of $N^2_{\text{bin}}$ in 100 m-bins, along with its experimental standard deviation $\sigma_{N^2}$ of the mean (King et al., 2012b).

We identified depths where $N^2_{bin}(z) \leq f^2_\phi$, in which $f_\phi = 2\Omega \sin(\phi)$, and $\phi$ is the latitude of each profile. This criterion defines turning depths for waves with $f_\phi \leq \omega$, which is what we expect for surface-generated near-inertial internal waves. In particular, we are interested in regions where there are consecutive depths $N^2_{bin}(z) \leq f^2_\phi$. Note that we used $N^2_{bin}$ rather than $N_{bin}$ to handle instabilities with $N^2_{bin} < 0$.

## 3.2 Results

### 3.2.1 Testing the computation of $N^2_{bin}$: a turning depth example

Especially at great depths, where the stratification is weak and $N^2$ is small, noisy $\theta$ and $S_A$ profiles make identifying turning depths difficult. As an example of how the post-processed $N^2_{bin}$ profiles improve this situation, we chose four profiles close to the same location at $\sim$(73 °N, 150 °W), but from different years (2005, 2007, 2008, and 2011) to illustrate the temporal (interannual) variability. In addition, and only for illustration purposes, we compare the $N^2_{bin}$ profiles to $N^2_{mvg}$ computed from original $\Theta$ and $S_A$ profiles of 2005 that have been smoothed by a 100 m-moving-average.

The temporal (interannual) variability of the $N^2_{bin}$ profiles is small (Fig. 3.2a) below 1000 m ($RMS_{N^2} = 6.83 \times 10^{-7} s^{-2}$). Below 2500 m, $N^2_{bin}$ approaches the local Coriolis frequency at 73 °N (the location of these profiles) and the tidal frequency $\omega^2_{M_2}$. These frequencies nearly coincide, because the critical latitude for the $M_2$ tide is at ∼74.5 °N (Rippeth et al., 2017a). $N^2_{bin}$ decreases further until the deep homogeneous bottom layer is reached, at ∼2700 m, where $N^2_{bin} \lesssim 4 \times 10^{-8} s^{-2}$. The following consecutive depths satisfy the criterion $N^2_{bin}(z) \leq f^2_o$. In contrast, $N^2_{mvg}$ fluctuates around $f^2_\phi$ (Fig. 3.2a) so that a turning depth cannot be identified in a statistically robust way. Note that all profiles have a very similar structure, implying that the post-processing method extracts the persistent modes of the water mass structure and does not introduce artifacts.

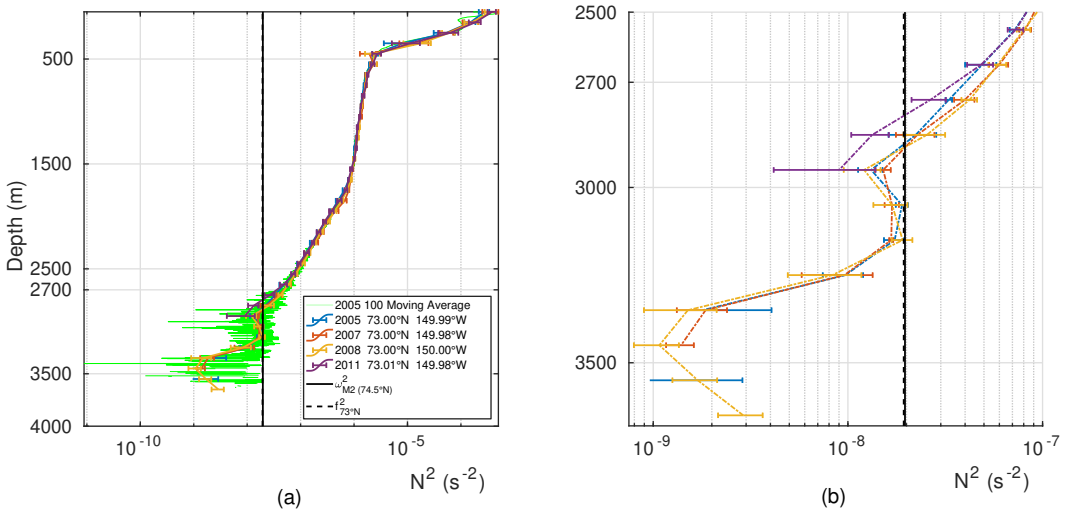


Figure 3.2: $N^2_{bin}$ profiles from a small geographical region show low temporal variability between 2005 and 2011. Below 2950 m, $N^2$ is generally smaller than $f^2_{73°N}$ and $\omega^2_{m2}$. (a) 100 m-$N^2_{bin}$. (b) Zoom in to 100 m-$N^2_{bin}$ for depths below 2500 m. In (a), the green line is the $N^2_{mvg}$ profile, computed conventionally from smoothed hydrography from 2005 (100 m-moving-average) for comparison, see text for the details. The vertical lines indicate the frequencies for $\omega^2_{m2}$ and $f^2_{73°N}$. In (a), and (b) the horizontal bars are the uncertainties $\sigma_{N^2}$.

### 3.2.2 Mean $N^2_{bin}$ and uncertainties $\sigma_{N^2}$

Near a turning depth, $N^2_{bin} \approx f^2_\phi$ so that, if $\sigma_{N^2}$ is too large, there can be cases for which $N^2_{bin} + \sigma^2_N > f^2_\phi > N^2_{bin}$. We exclude these cases and, as a condition that takes into account the estimated uncertainties, identify turning depths only if $N^2_{bin} + \sigma^2_N < f^2_\phi$. For instance, although below 2800 m nearly all $N^2_{bin} \leq f^2_o$, there are few data for which $N^2_{bin} + \sigma^2_N > f^2_o$ (Fig. 3.2b). These will not be termed turning depths, but only the following depths for which $N^2_{bin} + \sigma^2_N < f^2_o$.

$N^2_{bin} \pm \sigma_{N^2} < f^2_\phi$ or $> f^2_\phi$ varies between profiles and depths. On average, however, $N^2_{bin} \leq f^2_\phi$ and $\sigma_{N^2}$ is small (Fig. 3.3), so that we can apply a cumulative frequency analysis to assess the occurrence of depths where $N^2_{bin} + \sigma^2_N < f^2_o$. We normalized $N^2_{bin}$ and $\sigma_{N^2}$ by $f^2_\phi$, because the ratio $N^2_{bin}/f^2_\phi$ is useful to define transitions between regions (green and red dotted lines in Fig. 3.3 and 3.4). We found that below 2700 m the frequency of occurrence for $(N^2_{bin} + \sigma^2_N)/f^2_\phi \leq 1$ is higher than 90%, which is a robust result. There is not only one 100 m-thick sporadic turning depth, but below the first depth at which $N^2 + \sigma^2 < f^2_\phi$, the stratification of the consecutive depths is also $< f^2_\phi$. Thus, the turning depth is not only a single location but a layer,

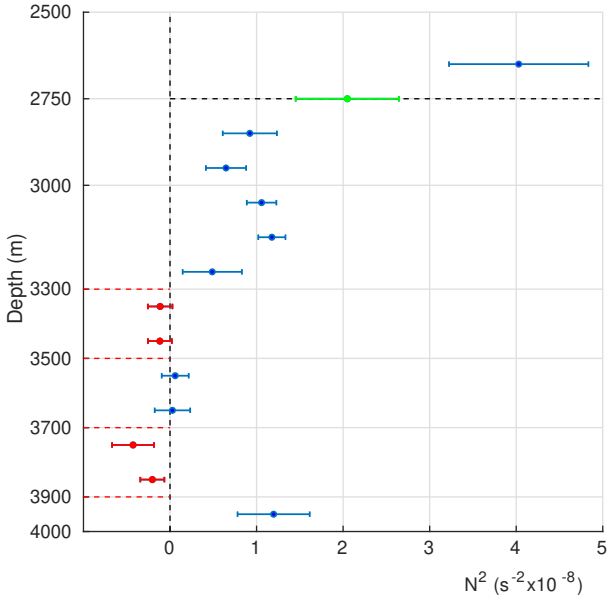


Figure 3.3: Averaged values of all profiles per depth for $N^2_{bin}$ and uncertainties $\sigma_{N^2}$. Near-inertial turning depth (NiTD) for the Canadian Basin at ∼2750 m (green dot). Evidence of locally statistically unstable layers at two depths (red dots), within 3300–3500 m and 3700–3900 m. Layers between 3700–3900 m are statistically unstable since $N^2_{bin} + \sigma_{N^2} < 0$.

making wave propagation less probable than having a single 100 m-thick turning depth value.

On average, the deep Canadian Basin is characterized by values of the ratio $N^2_{bin}/f^2_\phi < 1$ with small uncertainties $\sigma_{N^2} \leq 0.3\, f^2_\phi$. Particularly at 2750 m, $\sigma_{N^2} \approx 0.29\, f^2_\phi$ and $N^2_{bin}/f^2_\phi \approx 1$, so that at this depth the mean value of $N^2_{bin}$ is comparable to the local Coriolis frequencies within uncertainties $\sigma_{N^2}$. Hence, we identified 2750 m as the statistical near-inertial turning depth (NiTD) for the Canadian Basin.

Below 3150 m, $N^2_{bin}$ alternates between positive and negative values every 200 m (values between red lines in Fig. 3.3) suggesting locally stable ($N^2_{bin} > 0$) and unstable ($N^2_{bin} < 0$) layers within the (quasi-)homogeneous layer that extends to the bottom. Note that, between depths of 3550–4450 m, $N^2_{bin} + \sigma^2_N > 0$, hence strictly speaking, these layers are not unstable. In contrast, the layers between 3750–3850 m are locally unstable since $N^2_{bin} + \sigma^2_N < 0$. Geothermal heat fluxes from the seafloor (Timmermans et al., 2003) may trigger instability. Alternatively, since the homogeneous layer has neutral buoyancy stability, meaning that $N = 0$, the change in sign may be related to fluctuations around 0. We discuss these possibilities in Section 3.3.2.

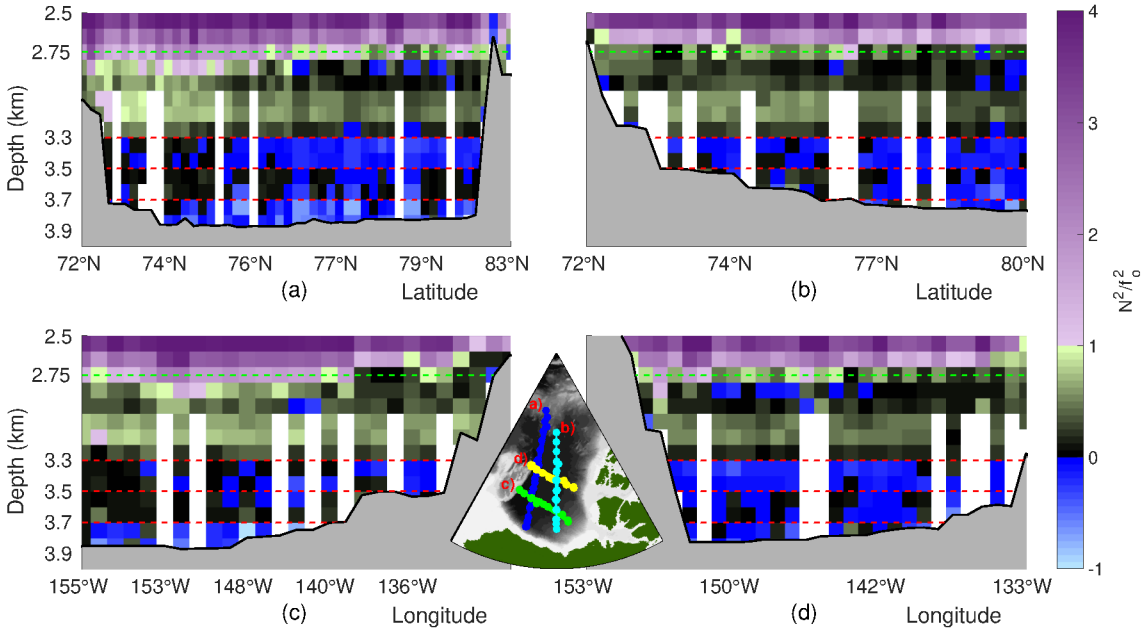


Figure 3.4: Ratio $N^2_{bin}/f^2_\phi$ for two zonal and two meridional transects in the Canadian Basin. Refer to Fig. 3.1 for the location of the sections: (a) Meridional section (dark blue dots in inset, cf. Fig. 3.1), (b) Meridional section (light blue dots), (c) Zonal section (green dots), (d) Zonal section (yellow dots). The color change from light lilac to light green defines the transition from $N^2 \geq f^2_\phi$ to $N^2 \leq f^2_\phi$. Near-inertial turning depth at ∼2750 m (green dashed line) defined by mean $N^2_{bin}$ in Fig. 3.3. The color change from dark green to dark blue defines the transition from $N^2 \geq 0$ to $N^2 \leq 0$. The inset shows each transect. Evidence of locally statistically unstable layers below 3300 m. The red dotted lines refer to the unstable layers within 3300–3500 m and 3700–3900 m defined by average $N^2_{bin}$ in Fig. 3.3.

### 3.2.3 Spatial distribution and heights

The spatial distribution of near-inertial turning depths in the Canadian Basin is nearly uniform at ∼2750 m (Fig. 3.4, color change from lilac to green at $N^2_{bin} = f^2_\phi$), coinciding with the top of the homogeneous layer or below it (Fig. 3.5 d–f).

Most of the meridional variability appears to be related to the strength of the stratification and its proximity to topographic slopes. For example, in the region between 72 °N–76.5 °N and > 143 °W, the turning depths occur in a deeper range between 2750–2950 m (Fig. 3.5a–c) and are located below the top of the homogeneous layer. In this region, $N^2_{bin}$ at 2750 m is relatively large ($N^2_{bin}$ ∼3–5×10 $^{-8}$ s$^{-2}$) compared to the rest of the Canadian Basin at the same depth ($N^2_{bin}$ ∼0. 5–2×10 $^{-8}$ s$^{-2}$), and the top of the homogeneous layer is also deeper than in the eastern Canadian Basin (Fig. 3.5a and d). Note that these deeper near-inertial turning depths at ∼2850 m are

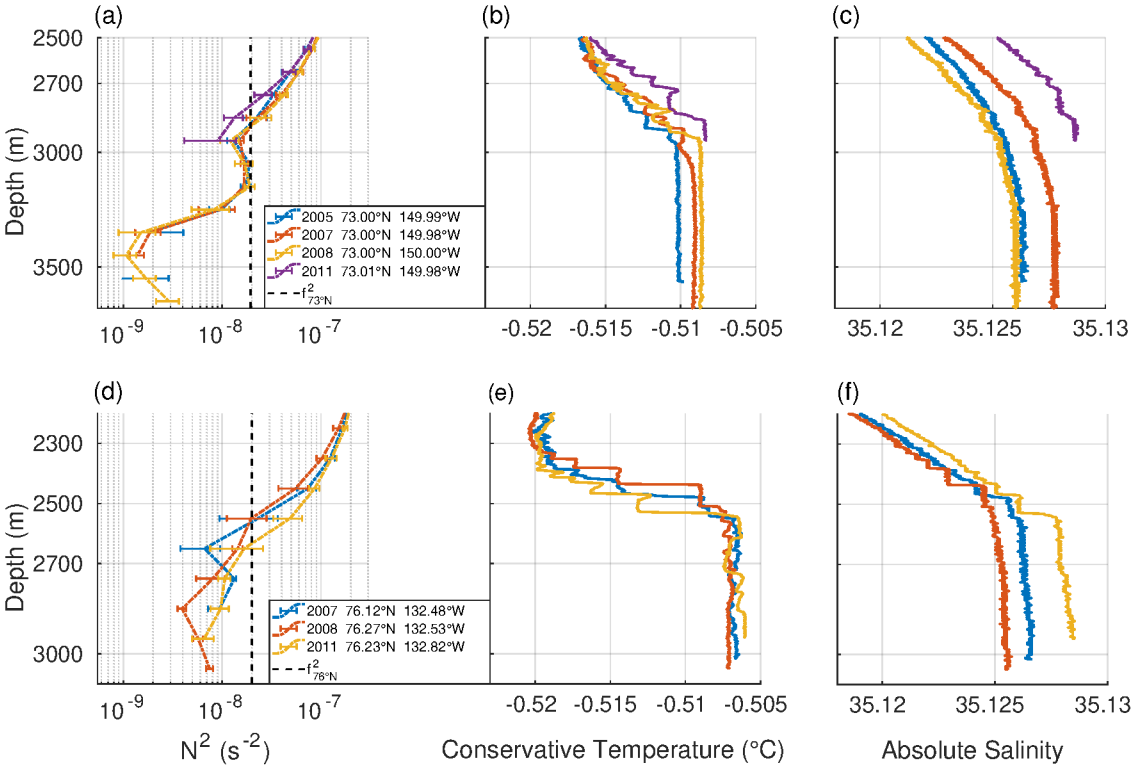


Figure 3.5: $N^2_{bin}$ and raw $\Theta$ and $S_A$ profiles from two small geographic regions between 2005 and 2011. (a–c) Western Canadian Basin at ∼73 °N and ∼150 °W, (d–f) Eastern Canadian Basin at ∼76.2 °N and ∼132.5 °W. The vertical lines show the frequencies for $f^2_{73°\mathrm{N}}$ and $f^2_{76°\mathrm{N}}$. In (a) and (d) the horizontal bars are the uncertainties $\sigma_{N^2}$. The $\Theta$ and $S_A$ profiles show the homogeneous layer and the deep thermohaline staircases. Note that the top and bottom panels have different y-axis limits.

found over nearly flat bathymetry (Fig. 3.4c), and the latitude varies $< 2°$ (Fig. 3.1, green dots), illustrating that the meridional variability away from the slope is in part related to the strength of the stratification for latitudes $< 76.5$ °N.

As $N^2_{bin}$ decreases and $f_\phi$ increases, the near-inertial turning depths for latitudes $>$ 76. 5 °N remain nearly constant at ∼2750 m, except in the Marakov Basin, where the near-inertial turning depths are deepest at ∼3050 m, but have a relatively strong stratification of $N^2_{bin}$ ∼1.2–2.8×10 $^{-8}$ s$^{-2}$, which is compensated by $f^2_\phi$.

A peak in $N^2_{bin}/f^2_\phi$ (light green) below the NiTD at ∼3150 m is a consistent feature throughout the Canadian Basin (Fig. 3.4), coinciding with a slight increase in $S_A$ with depth while $\Theta$ remains constant (Fig. 3.5). Below 3300 m, the stratification is $N^2_{bin} < 0$ within the homogeneous bottom layer (color change from green to blue

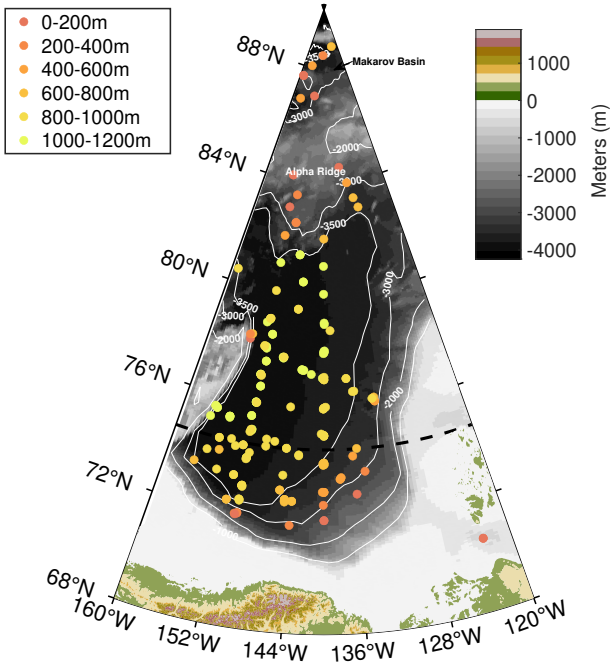


Figure 3.6: Spatial distribution of turning depth heights in the Canadian Basin. The turning depth height is the distance from the sea floor to each near-inertial turning depth. The black dashed line indicates the critical latitude for the $\omega^2_{M_2}$.

in Fig. 3.4), except when $S_A$ or $\Theta$ increases with depth. For example, in the deep western Canadian Basin or on the slope in the eastern part (see Fig. 3.5).

To quantify the proximity to the bathymetry, we defined the turning depth height as the distance from the sea floor to each near-inertial turning depth (Fig. 3.6). We computed the sea floor depth for each profile by averaging the four nearest depths of the IBCAO bathymetry (Jakobsson et al., 2012) to the profile location.

Generally, the turning depth height distribution is related to the isobaths. Over the slope between the 2500–3500 m isobaths and latitudes $< 76\,^{\circ}$N, the turning depth heights are between 0–800 m. Below the 3500 m-isobath and over the Canadian abyssal plain, the turning depth heights are between 800–1200 m, increasing northward to a maximum of 1000–1200 m. Further northward, on the slope of the Alpha Ridge and the Makarov Basin, the turning depth heights decrease to 0–800 m. Overall, surface-generated near-inertial internal waves traveling downward are unlikely to interact with the topography since the near-inertial turning depths are far above the seafloor (up to 1000 m). We discuss the possible wave-topography interactions in Section 3.3.1.

### 3.2.4 Non-traditional effects: critical $N^2$ for near-inertial internal waves

In stratified hydrostatic geophysical flows, only the vertical component of the Coriolis force is taken into account ($f = 2\Omega \sin(\phi)$). Under these assumptions, the frequency band for internal gravity wave is bounded by $f^2$ and $N^2$. Relaxing the hydrostatic approximation to the quasi-hydrostatic approximation, also called non-traditional approximation (NT), involves including the horizontal components of the Coriolis force that vary with the cosine of latitude. With this approximation, the frequency band for internal gravity waves is expanded beyond $f^2$ and $N^2$. Among all effects of NT in wave propagation, we are interested in those that happen at depths where $N \approx 0$ and in weakly stratified layers comparable to the Coriolis force $N \approx 2\Omega$. Under NT, a reflection level no longer exists at $\omega = N(z)$ but at a critical buoyancy frequency $\omega = N_{crt}(z)$ typically smaller than the turning depth frequency calculated with the usual traditional approximation (TA) (Gerkema et al., 2008). Explicitly, the critical buoyancy frequency, $N_{crt}(z)$, is defined as follows:

$$N^2_{crit} = \omega^2 \frac{(f^2 + f_s^2 - \omega^2)}{f^2 - \omega^2} \tag{3.2}$$

In which $f_s = 2\Omega \cos(\phi) \sin(\alpha)$ is the cosine component of the Coriolis force, and $\alpha$ is the angle to the North-South direction. If we set $\alpha = 0$, the TA definition for a turning depth is recovered, in which $N(z) = \omega$, and since $f_s = 0$, the wave propagation is purely zonal, implying NT effects act only upon waves propagating with a meridional component (King et al., 2012b; Gerkema et al., 2008).

From Eq. 3.2, we obtain $N_{crit} = 0$ for a wave with frequency $\omega^2 = f^2 + f_s^2$. Waves with this frequency are known as gyroscopic waves, and they can propagate in layers of neutral stratification (Haren & Millot, 2005), so that there are no turning depth for these waves. In the deep Canadian Basin, near(sub)-inertial fluctuations have been detected (Timmermans et al., 2007), but the nature of the observations suggest these are not gyroscopic waves but that they are related to bottom-trapped topographic Rossby waves at the sub-inertial frequency range (Timmermans et al., 2010; Zhao & Timmermans, 2018).

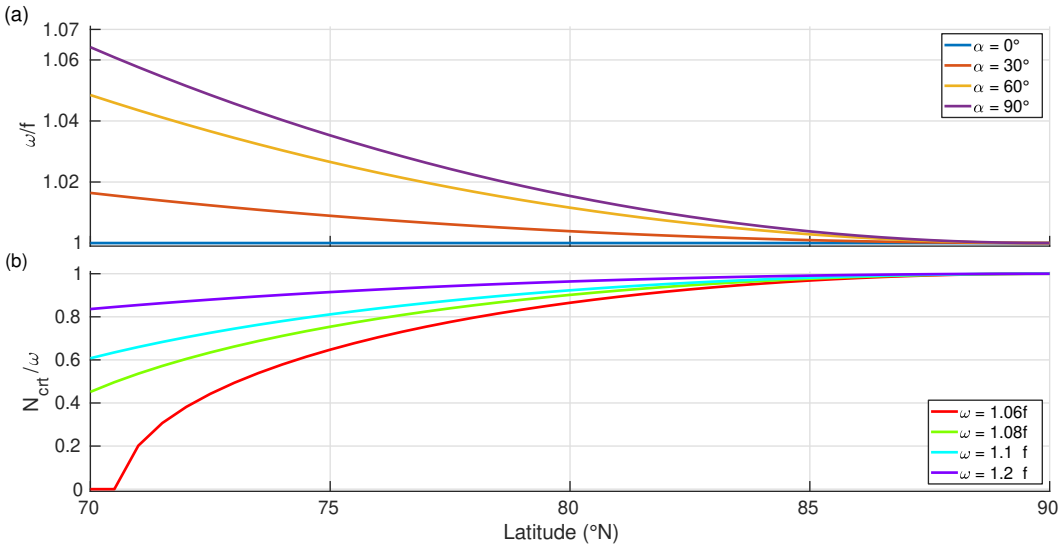


Figure 3.7: (a) Latitudinal variability of waves with frequency $\omega^2 = f^2 + f_s^2$ normalized by $f$. Waves with equal and lower frequencies can propagate through arbitrary stratification, and waves with higher frequencies cannot propagate through depths with certain small values of $N_{crt}$. The colors indicate the direction of propagation, being $\alpha$ the angle to the East-West direction. (b) Example of minimum values of $N_{crt}$, under NT, for a specific range of waves with near-inertial frequencies and meridional propagation ($\alpha = 90°$), which could be generated at the surface by wind forcing. Waves with these frequencies cannot propagate through depths with these specific values of $N_{crt}$ (normalized by $\omega$).

Note that, since $N_{crit} = 0$ when $\omega^2 = f^2 + f_s^2$, any frequency higher than $f^2 + f_s^2$ result in $N_{crit} > 0$. Thus, the frequency $f^2 + f_s^2$ could be interpreted as the lower limit for a wave to find a turning depth under the NT. For instance, Fig. 3.7a shows the $\omega$ lower limit as a function of $f$ and $\alpha$. In the Canadian Basin, these frequency values are in the range of $\omega \approx 1 - 1.07 f_\phi$. Pure meridional propagation ($\alpha = 90°$) is associated with the maximum frequencies (lilac line in Fig. 3.7a), and $\omega$ decreases as the wave approach zonal propagation ($\alpha = 0°$).

From Eq. 3.2 we can estimate $N_{crit}$ for specific near-inertial frequencies that account for hypothetical waves generated at the surface. $\omega = 1.06 - 1.08\, f$ are typical near-inertial frequencies observed in the Arctic Ocean (D'Asaro & Morehead, 1991; Halle, 2003; Fer, 2014; Cole et al., 2018). In general, for latitudes $\geq 72°$ N, near-inertial internal waves with frequencies $\omega \geq 1.06\, f$ have a turning depth with $N_{crit}$ in the range $0 < N_{crit} \leq f$ in the Canadian Basin (Fig. 3.7b). Such frequencies $N_{bin}^2$ exist below NiTD at 2750 m in the entire deep Canadian Basin (Section 3.2.2, Fig. 3.4).

Thus, for both TA and NT, near-inertial internal waves with $\omega \geq f$ and $\omega \geq 1.06\,f$ have a turning depth up to 1000 m above the sea floor. Under NT, near-inertial internal waves with frequencies $\omega < 1.06\,f$ traveling meridionally can propagate through arbitrary stratification.

## 3.3 Discussion

Our results of $N^2_{bin}$ and $\sigma_{N^2}$ are comparable to previous observations of $N^2$ in weakly stratified waters. For example, using the method of King et al. (2012b), squared buoyancy frequencies lower than the diurnal tidal frequency were found in the South China Sea (Liu et al., 2022) with $N^2_{bin} \approx 5.317 \times 10^{-9} s^{-2}$. This is comparable to the average $N^2_{bin}$ below 3000 m of $\sim 3.1 \times 10^{-9} s^{-2} \pm 2.1 \times 10^{-9} s^{-2}$. Furthermore, squared buoyancy frequencies of $N^2 \sim 4 \times 10^{-8} s^{-2}$ in the deep water of the Canadian Basin (Timmermans et al., 2003; Timmermans & Garrett, 2006) are similar to our average $N^2_{bin}$ below 2500 m of $\sim 1.16 \times 10^{-8} s^{-2} \pm 0.32 \times 10^{-8} s^{-2}$.

In addition, from the WOCE Database typical values of the experimental standard deviation for the semi-diurnal tidal frequency of 0.3–0.1 $\sigma_{\omega_{m2}}$ were computed (King et al., 2012b) for the world ocean except for the Arctic Ocean. Along with this, observations of $N$ in the deep Mediterranean Sea were calculated with a standard deviation of $0.8\,f$ over 100 dbar bins; this value was reduced to $0.4\,f$ over 600 dbar bins (Haren & Millot, 2006). This is similar to the $\sigma_{N^2}$ values, we found below the NiTD, of $\sigma_{N^2} \leq 0.3\,f^2_\phi$ ($\sigma_N \leq 0.54\,f_\phi$).

The turning depths are related to the location of the deep staircases, the top of the homogeneous layer and the $N^2$ peak below it (see Fig. 3.5). For example, taking the top of the homogeneous layer as the depth at which temperature and salinity begin to be constant with depth (e.g. in Fig. 3.5e–f), Timmermans et al. (2003) reports layer thicknesses of $\sim$1000 m in the central Canadian Basin when the top of the homogeneous layer is at $\sim$2700 m, which is consistent with our definition of NiTD at 2750 m and also with the turning depth height.

The homogeneous layer is deeper in the western Canadian Basin with its upper limit varying meridionally by about 100 m (Timmermans et al., 2007). To the east it is

shallower with a thickness of 580 m on the slope at 73.5 °N, 137 °W (Timmermans et al., 2007). In our estimates, the turning depth is deeper to the west (Fig. 3.4) and the turning depth height to the east is between 400–600 m (Fig. 3.6). Our results are consistent with the spatial variability of the homogeneous layer thickness (Timmermans et al., 2003; Timmermans & Garrett, 2006). However, in general, the heights of the turning depths are thinner than the thickness of the homogeneous layer, and the near-inertial turning depths are deeper than the top of the homogeneous layer.

### 3.3.1 Wave-topography interactions and mixing below a turning depth

For ice-covered oceans, surface-generated internal waves are hypothesized to be partially dissipated under sea ice after one round-trip from the surface to the bottom (Pinkel, 2005; Cole et al., 2018). The NiTD will reduce the distance and travel time of near-inertial internal waves to reach the surface after reflection, as near-inertial internal waves cannot propagate through the NiTD. Generally, mixing is low on the flat bottom and increases towards the slopes and ridges (Rainville & Winsor, 2008; Lincoln et al., 2016). In the Canadian Basin, the NiTD overlaps deep slopes and steep topography close to the Alpha Ridge (refer to Fig. 3.4 and 3.6), which might prevent waves from playing a more important role in controlling mixing rates above the sea floor.

Even though waves cannot freely propagate across turning depths, part of the wave, known as the evanescent tail, can penetrate. In this process, the wave's amplitude decreases exponentially below the turning depth (Paoletti & Swinney, 2012a). In the Canadian Basin, shallow turning depth heights are located above steep and rugged topography (Fig. 3.6). If those layers are not thick, the evanescent tails of the near-inertial internal waves can interact with the topography (Paoletti et al., 2014a), and they might play a non-trivial role in mixing the Arctic Ocean interior.

From water tank experiments and numerical simulations, Paoletti and Swinney (2012a) deduced that the horizontally-integrated vertical energy flux $\Phi$ decays exponentially from a turning depth in the following way $\Phi(z) = \Phi_{zc}\, e^{-k_c(z_c - z)}$, in which $k_c$ is the horizontal wave number at the turning depth $z_c$. From this relation, we can

estimate the horizontal wavelength, for which the energy flux $\Phi(z)$ is reduced by an order of magnitude. For turning heights above the bottom in the range of 100-1200 m, such a flux reduction occurs for horizontal wavelengths of 300-3700 m. Therefore, although the energy flux is reduced by an order of magnitude, near-inertial internal waves at these wavelengths can still interact with the bottom.

The magnitude of $k_c$ at turning depths is unknown. However, assuming the values estimated in section 3.1.3 and ignoring changes in $k$ as the wave propagates, the flux $\Phi(z)$ of a wave with a horizontal wavelength of 10 km reflecting off a 1200 m thick evanescent layer decreases by a factor of about 2. The reduction of $\Phi$ varies with vertical wavelength and frequency range. For example, for $\omega = 1.05f$, shorter or longer initial vertical wavelengths of 10–100 m result in horizontal wavelengths of ∼1.8–18.8 km and a reduction in wave flux by a factor of ∼65–1.5. Similarly, for a fixed vertical wavelength of 50 m, a change in $\omega$ between $1.01f$ and $1.1f$ results in a horizontal wavelength of ∼7–2 km and a reduction in wave flux by a factor of $\sim 1.4$–3. In particular, significant reductions in wave flux occur only for internal waves with horizontal wavelengths $< 5000$ m at turning depths.

Wave-topography interactions below a turning depth have been studied using numerical models and water tank experiments. For example, topography below a turning depth can generate internal tides under tidal forcing (Paoletti et al., 2014a), and evanescent wave perturbations can generate propagating waves after reaching a depth where $\omega < N^2(z)$ (Lee et al., 2020a). Thus, despite the presence of NiTDs, near-inertial internal waves can still partially account for the deep mixing in the Canadian Basin.

At the top of the homogeneous layer there are thermohaline staircases with a step size of $\sim 10$–50 m and a transition layer of $\sim 10$–25 m throughout the Canadian Basin (Timmermans et al., 2003; Timmermans et al., 2010; Zhou & Lu, 2013; Zhou et al., 2014). These density structures act as a filter for internal waves (Ghaemsaidi et al., 2016b; Sutherland, 2016), leading to wave reflection especially for waves with relatively short length scales. The vertical location of the staircases varies, but assuming that the staircases are between 2500–2700 m (see Fig. 3.5), then $N^2_{bin} \sim 2$–$9\times10^{-8}s^{-2} \pm 1$–$2\times10^{-8}s^{-2}$. However, between each step, the stratification is close

to zero ($N \sim 0$), which cannot be accurately represented by averaging over 100–meter bins. As a result, the binned $N^2_{bin}$ fails to reproduce the step-wise stratification with $N \sim 0$ between steps.

We expected that surface-generated near-inertial internal waves interact with the staircases before reaching the NiTD, modifying their propagation depending on the time and length scales of the wave (Ghaemsaidi et al., 2016b). For typical values of mid-water stair-cases and internal waves in the Arctic Ocean, near-inertial internal waves with wavelength of approximately 50 km transmit across the staircases with little reflection (Sutherland, 2016). These near-inertial internal waves can continue to propagate downwards, but for the staircases in the deep abyss, the internal waves immediately encounter the homogeneous bottom layer and the bottom itself. For this case, let us assume a stratification that allows internal waves to propagate across the deep staircases. We can then calculate the lower wavelength limit of the transmitting waves $\lambda_{Tl} \simeq 0.5\pi D\,(\,0.1\,(\omega^2 - f^2\,)/\,N^2)^{-1/2}$ (Sutherland, 2016), where $D$ is the total length of the staircase. For $\omega = 1.05f$, $D = 150\,\mathrm{m}$ and $f = 0.5N$ ($N_{bin}$ between 2500–2700 m), the lower bound for internal waves transmitting with little reflection is $\lambda_{Tl} \simeq 4.6\,\mathrm{km}$. Therefore, we would expect near-inertial internal waves with longer wavelengths to be able to propagate. However, we cannot rule out other processes, in which near-inertial internal waves attenuate or promote mixing, such as the onset of instability within the staircase.

### 3.3.2 Unstable layers and convective instability

If the main impact of the NiTD in the deep Canadian Basin is to isolate the bottom from surface-generated wind-driven waves, near-inertial internal waves will not play a substantial role in driving the bottom layer dynamics, and other processes, for example, convective instability, govern bottom mixing.

Geothermal heat flux estimates in the Canadian Basin are $F_H \sim 40 - 60\ \ \mathrm{mW\,m^{-2}}$ (Langseth et al., 1990). A considerable fraction of this heat remains in the homogeneous bottom layer. Approximately $F_H \sim 0.1 - 45\ \ \mathrm{mW\,m^{-2}}$ escape through density staircases above the bottom layer (Carmack et al., 2012; Zhou & Lu, 2013; Zhou et al., 2014; Timmermans et al., 2003).

There are two main hypotheses for driving this heat flux transport. The heat is transported either horizontally and escapes near the slope where mixing is strong (Timmermans et al., 2003), or it is driven vertically by thermobaric convection (Carmack et al., 2012). There is evidence that convective instability controls the bottom layer (Zhou et al., 2014) supporting the direct vertical flux of heat. Between 3300–3900 m, we identified consecutive locally unstable layers, which also supports the convective instability hypothesis.

The geothermal flux heats the layer from below, which increases the temperature of the adjacent water parcels. This layer gains buoyancy and destabilizes the upper layers, which may be reflected in the alternating positive and negative $N^2_{bin}$ values. We expect that the homogeneous layer is close to neutral buoyancy $N \approx 0$, but finding exact values of $N = 0$ is unrealistic. The locally unstable values of $N^2_{bin}$ might be related to fluctuations around $N^2_{bin} = 0$, so that the layer does have neutral buoyancy but is unstable, suggesting periods of convective mixing. In addition, the homogeneous layer may have a theoretical thickness of 1051 m (Zhou et al., 2014) based on a comparison of the deep Canadian homogeneous layer thickness to experiments conducted with salt-stratified fluids heated from below. If we consider only the unstable layers (Figs. 3.3 and 3.4), the thickness of the homogeneous layer is ∼600–700 m. However, assuming that the top of the homogeneous layer is at ∼3000 m, just above the peak in $N^2_{bin}$ (Fig. 3.3), the thickness increases up to 1000 m, which is consistent with Zhou et al. (2014) and therefore with the convective instability hypothesis.

In the ocean, wave-driven near-bottom dissipation is still largely unknown (Thomas & Zhai, 2022). We cannot directly compare the results obtained by experiments and simulations described in this section to the actual ocean. However, our results show that in the Arctic Ocean, near-inertial turning depths exist and may play a bigger role in the propagation and reflection of near-inertial internal waves than elsewhere. Further study is needed to understand the wave dynamics in the changing Arctic Ocean. Finally, a homogeneous bottom layer is also present in the Eurasian Basin, and the analysis of some profiles shows turning depths for near-inertial internal waves (not shown). Hence some of the impacts and effects discussed in this section might also apply to the Eurasian Basin.

## 3.4 Summary & Conclusion

Our analyses of buoyancy frequency $N^2$ in the deep Canadian Basin and interpretations of near-inertial turning depths are summarized as follows:

1. From the analysis of $N^2_{bin}$ derived from temperature and salinity profiles of the UDASH dataset from 2005 to 2014 and a statistical method of King et al. (2012b), near-inertial turning depths are found in the deep Canadian Basin at $\sim$2750 m depth and between 100 m and 1200 m above the sea floor.

2. For the traditional and the non-traditional approximation, near-inertial internal waves have turning depths for frequencies $\omega \geq f_\phi$ and $\omega \geq 1.06 f_\phi$, respectively. Furthermore, under the non-traditional approximation, near-inertial internal waves with frequencies $\omega < 1.06 f_\phi$ traveling meridionally can propagate through arbitrary stratification.

3. There are layers below 3300 m that are locally slightly unstable, $N^2_{bin} < 0$. These values are consistent with a homogeneous layer that is quasi-neutral with $N \approx 0$, and with the hypothesis that geothermal flux heats the homogeneous bottom layer from below, destabilizing the overlying layers.

4. After reflection at the NiTD the evanescent wave tails may interact with bathymetry, mainly over slopes where the turning-depth heights above topography are small.

The evidence presented in this study cannot prove with certainty that near-inertial internal waves reflect at turning depths in the deep Canadian Basin. However, we provided different scenarios involving near-inertial wave reflection from turning depths. Further measurements, numerical simulations, and theory are necessary to understand the interaction of near-inertial internal waves upon reflection from turning depths and to link surface-generated waves to mixing rates in the interior and above slopes in the Canadian Basin. This understanding may become very important for correctly representing the changing Arctic Ocean and its future state in climate projections.

# Chapter 4

In this chapter we addressed the third research question. Do near-inertial internal waves reach the bottom in the Eurasian Basin of the Arctic Ocean after surface generation by a combination of wind and sea ice properties?

The results of this chapter are being prepared for publication.

# 4 Observations of deep near-inertial internal waves in the Eurasian Basin under weak stratification

In previous chapters, numerical simulations and indirect observations have shown how internal waves partially propagate across a thermohaline staircase and their feasibility in driving deep mixing in weak stratification. However, no evidence has been provided for surface-generated internal waves that propagate and eventually reach the seafloor.

The main objectives of the PS137 expedition was to study the new lithosphere and associated hydrothermal circulation at the Aurora vent site in the ultraslow spreading Gakkel Ridge in the Eurasian Basin of the Arctic Ocean. A mooring was used to monitor hydrothermal dynamics, with a focus on the dispersal of the hydrothermal plume by *in-situ* ocean currents (Schlindwein, 2023). Innovative and unprecedented deep current observations were obtained that may help to understand the extent to which near-inertial internal waves are expected to drive mixing in the interior beyond the critical latitude for semi-diurnal tides. In a changing Arctic with diminishing sea ice cover, this information may be important to better understand how the climate will change in the future.

## 4.1 Data

### 4.1.1 Currents

The mooring AURORA-1 was placed at 82°53,866'$N$, 006°15,043'$W$ in July 2022 (refer to Fig. 4.1) and subsequently retrieved in July 2023. The AURORA-1 was positioned at a maximum water depth of 3855m. The Doppler Current Meter RCM-11 recorded the horizontal current speed at 3572 m, 3366 m, 3215 m, and 3064 m depth with a interval of 60 minutes (Table 1). This instrument has a range of 0–300 cm $s^{-1}$, resolution of 0.3 cm $s^{-1}$ and an absolute accuracy of $\pm$ 0.15 cm $s^{-1}$. Its statistical precision is $<$ 0.45 cm $s^{-1}$ (standard deviation). The compass has a resolution of 0.35° and an accuracy of $\pm$ 5 ° for 0–15° tilt, and $\pm$ 7.5° for 15–35° tilt (Table 2).

| Instrument | Depth | Sampling interval | Mean u velocity | Mean v velocity |
|---|---|---|---|---|
| RCM-11 | -3064 m | 60 min | -1.19 cm $s^{-1}$ | -0.46 cm $s^{-1}$ |
| RCM-11 | -3215 m | 60 min | -1.25 cm $s^{-1}$ | -0.32 cm $s^{-1}$ |
| RCM-11 | -3366 m | 60 min | -1.21 cm $s^{-1}$ | 0.36 cm $s^{-1}$ |
| RCM-11 | -3572 m | 60 min | -0.21 cm $s^{-1}$ | 0.06 cm $s^{-1}$ |

Table 1: Depth, sampling interval, and mean zonal and meridional velocities recorded by the RCM-11 Doppler Current Meter.

| Instrument type | Range | Resolution | Accuracy | Precision |
|---|---|---|---|---|
| RCM-11 | 0–300 cm $s^{-1}$ | 0.3 cm $s^{-1}$ | $\pm$ 0.15 cm $s^{-1}$ | $<$ 0.45 cm $s^{-1}$ |

Table 2: Range, resolution, accuracy and precision of the Doppler current meter RCM-11.

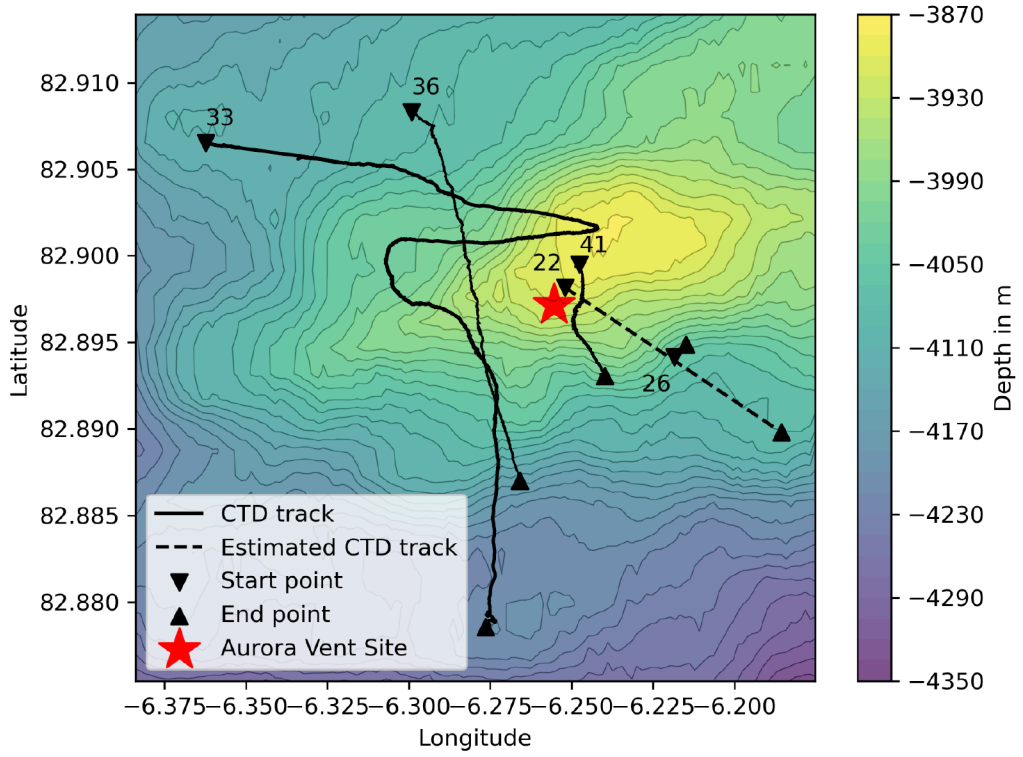


Figure 4.1: Bathymetry near the Aurora vent site. The red start marks the location of the AURORA-1 mooring at 82°53,866'$N$, 006°15,043'$W$. Black lines are the ship track of the expedition PS137. Each number represent sections where vertical profiles of temperature and salinity were taken. The profiles of site 22 were used to compute the initial stratification $N$ (refer to Fig. 4.7) for all the simulations (Sec. 4.4).

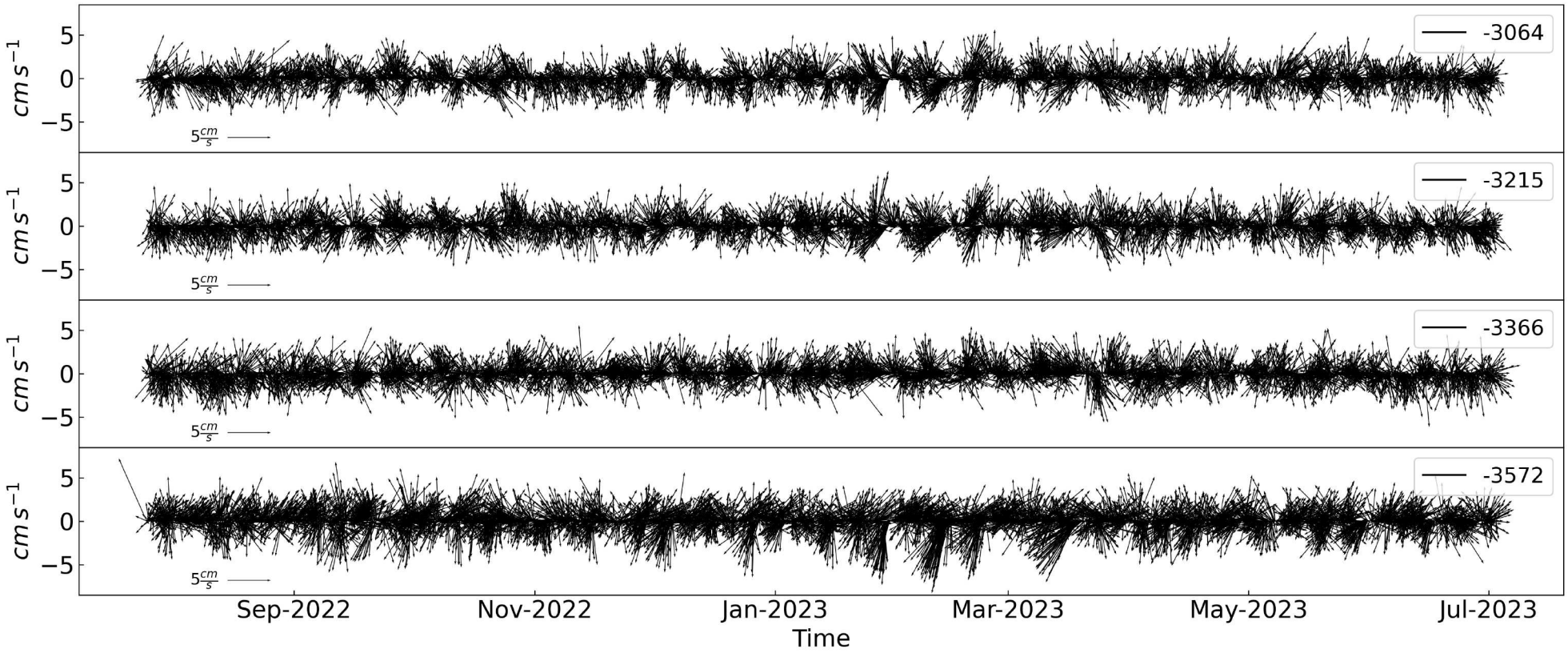


Figure 4.2: Time series of raw velocity currents from the AURORA-1 mooring array at Gakkel Ridge ( 82°53.866'$N$, 006°15.043'$W$). The velocity currents correspond to the period between July 25, 2022 and July 7, 2023 for the depths 3572 m, 3366 m, 3215 m and 3064 m.

### 4.1.2 Temperature and salinity

Temperature and salinity vertical profiles were collected using a Sea-Bird SBE 9 Conductivity-Temperature-Depth (CTD) device with a high level of precision for temperature and conductivity of $\pm 0.001\ ^{\circ}C$ and $\pm 0.0003\ S\ \mathrm{m}^{-1}$, respectively. The casts were conducted around the Aurora vent site, with particular focus on the profile near the AURORA-1 mooring location at 82° 53.89 N, 006° 15.12 $W$, corresponding to site 22 depicted in Fig. 4.1.

### 4.1.3 Sea Ice Drift

The sea-ice actual drift was retrieved from the OSI SAF (Ocean and Sea Ice Satellite Application Facilities) product for $82.9^{\circ}N$, $6.^{\circ}W$ (Provided by T. Krumpen, AWI).

### 4.1.4 Wind speed

Wind speed was obtained from the 2022 to 2023 ERA5 10-m winds reanalysis (Hersbach et al., 2020; Hersbach et al., 2023). The dataset has a grid resolution of $0.25^{\circ} \times 0.25^{\circ}$ at hourly intervals. To ensure accuracy, we selected the latitude of $6.25^{\circ}W$, which is nearest to the mooring site and latitudinally averaged the data from 82.75-84.75 $^{\circ}N$.

### 4.1.5 Ice concentration

The data on sea ice concentration is obtained from the AMSR-E (Advanced Microwave Scanning Radiometer-EOR) sensor, calculated based on an average of several daily satellite overflights. The dataset has a grid resolution of 6.25 km × 6.25 km (Spreen et al., 2008). For this investigation, we have regridded the data to a resolution of $0.1^{\circ} \times 0.3^{\circ}$ and applied latitudinal averaging between 82.75-84.75 $^{\circ}N$.

## 4.2 Methods

### 4.2.1 Incoherent internal waves

The velocity components in the East-West ($u$) and North-South ($v$) directions were calculated based on the current speed and direction at each depth. The velocity time series was interpolated with a unique hourly time vector to account for the time

lags observed in some measurements (Fig. 4.2). The velocity was then treated as a complex vector $\mathbf{U}(\mathbf{z},\mathbf{t}) = u(z,t) + \imath v(z,t)$ for subsequent analysis. The temporally-averaged mean was removed, and the $\mathbf{U}(\mathbf{z},\mathbf{t})$ was detided by subtracting the coherent tides obtained by harmonic analysis at each depth. The resulting vector is defined as the velocities associated with the incoherent internal motions $\mathbf{U_{it}}(\mathbf{z},\mathbf{t})$. A similar treatment has been used to study coherent and incoherent internal waves and tides (Zhao et al., 2010; Cao et al., 2019).

### 4.2.2 Band-pass filter for near-inertial internal waves

A fourth-order Butterworth bandpass filter was used to separate the near-inertial velocities, using upper and lower bounds set at $[0.98\text{-}1.1]f$. These bounds include the superinertial peak at $1.05f$ (refer to Fig. 4.6), but only slightly exclude the frequency of $M_2$ ($\approx 0.97f$). We have denoted this bandpass filtered time series as the near-inertial incoherent velocities $\mathbf{U_f}(\mathbf{z},\mathbf{t})$. Note, however, that the filter does not completely suppress all frequencies beyond the cutoff band, meaning that the $M_2$ baroclinic tides are expected to contribute, even though they are evanescent at this latitude (Rippeth et al., 2017b; Rippeth et al., 2015; Artana et al., 2022).

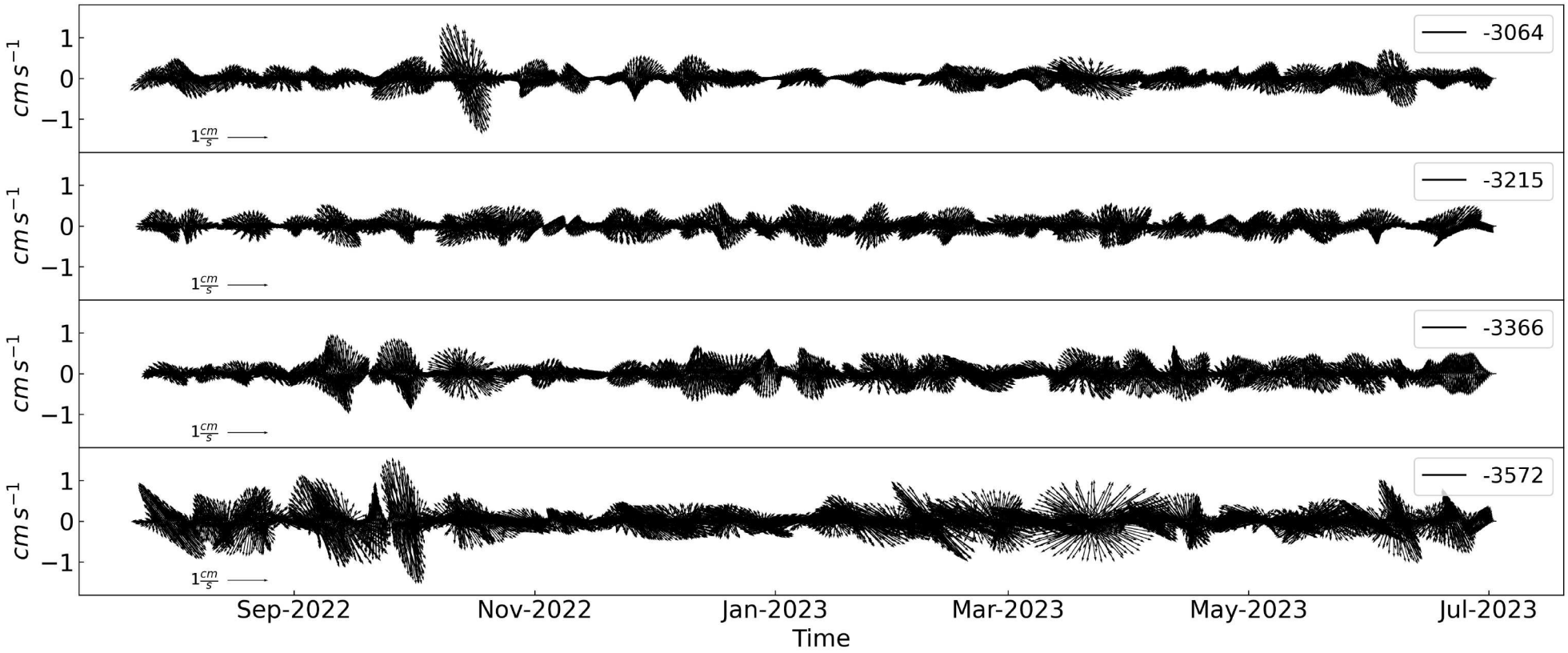


Figure 4.3: Band-pass filter data $\mathbf{U_f(z,t)}$. The velocity currents correspond to the period between July 25, 2022 and July 7, 2023 for the depths 3572 m, 3366 m, 3215 m and 3064 m.

### 4.2.3 Upward- and downward velocities and kinetic energy

The Multi-Taper method (MTm) was utilized to obtain the clockwise ($CW$) and counterclockwise ($CCW$) frequency spectrum (Lilly & Elipot, 2021) of $\mathbf{U}(\mathbf{z},\mathbf{t})$ and $\mathbf{U_{it}}(\mathbf{z},\mathbf{t})$. The MTm estimate the spectrum by selecting windows, called tapers, to minimize the spread of energy across different frequency bins (spectral leakage). It also reduces the variance of the estimate by averaging multiple orthogonal eigenspectrum estimates (Lees & Park, 1995). We set the MTm to smooth over 15 adjoining frequencies. The $CW$ ($CCW$) spectrum in the Northern Hemisphere has usually been associated with internal waves with downward (upward) energy propagation (Ferrari & Wunsch, 2009b; Alford et al., 2007). We use this description in Fig. 4.4– 4.5 to qualitatively compare the frequency spectrum of $\tilde{\mathbf{U}}(\mathbf{z},\omega)$ and $\tilde{\mathbf{U}}_{\mathbf{it}}(\mathbf{z},\omega)$, where the tilde represents the Fourier transform.

The quadrant method (Alford et al., 2012; Alford et al., 2017; Wang et al., 2023; Kawaguchi et al., 2020) was employed to obtain the upward and downward near-inertial velocities of $\mathbf{U_f}(\mathbf{z},\mathbf{t})$ by calculating their two-dimensional (2D) spectra $\tilde{\mathbf{U}}_{\mathbf{f}}(\mathbf{k},\omega)$. The kinetic energy moves with the group velocity $C_g$ which is perpendicular to the phase speed $c = \omega/k$. Thus, the wave energy in the upward (downward) direction corresponds to the quadrants where $-\omega/+k$ ($+\omega/+k$) and $+\omega/-k$ ($-\omega/-k$) are present. By 2D Fourier inversion of the spectrum, the velocity components $\mathbf{U_{f_{up}}}(\mathbf{z},\mathbf{t})$ and $\mathbf{U_{f_{dw}}}(\mathbf{z},\mathbf{t})$ were recovered. This allows to identify wave energy propagating to the bottom (surface) of the ocean, where down (up) indicates a negative (positive) value of $C_g$ (Pinkel, 2008; Baumann & Fer, 2023). The near-inertial kinetic energy was calculated as $KE_*(z,t) = \frac{1}{2}\rho|\mathbf{U}_*(\mathbf{z},\mathbf{t})|^2$, where $*$ denotes either the upward or downward component, and $\rho = 1024$ kg m$^{-3}$.

## 4.3 Results

### 4.3.1 Frequency spectra: internal waves and tides

Fig. 4.4 and 4.5 show the spectra of the raw $\tilde{\mathbf{U}}(\mathbf{z},\omega)$ and the incoherent $\tilde{\mathbf{U}}_{\mathbf{it}}(\mathbf{z},\omega)$ velocity time series. The spectra exhibit comparable spectral power with the highest values corresponding to the deepest current record (-3752m). No significant differences are observed for the $CW$ and $CCW$ components. $\tilde{\mathbf{U}}(\mathbf{z},\omega)$ display energetic

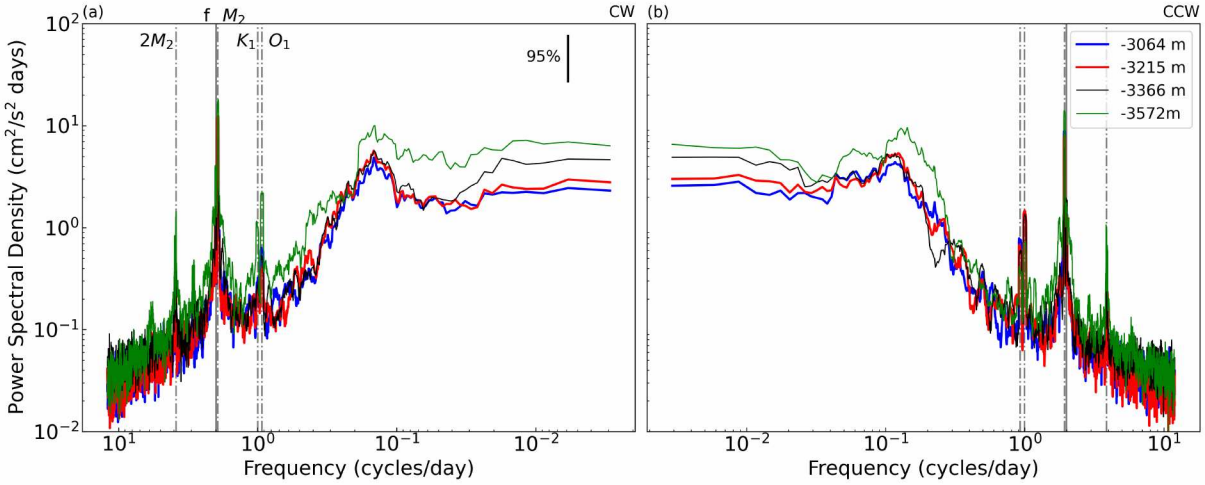


Figure 4.4: Frequency spectra of the raw velocities $\mathbf{U}(\mathbf{z}, \mathbf{t})$ for (a) *CW* and (b) *CCW* component as described in Sec. 4.2.3. Colors represent different depths. The vertical lines represent the tidal constituents $M_2$, $K_1$, $O_1$, the Coriolis frequency $f$ at the mooring site, and the first semidiurnal tidal harmonic $2M_2$. The vertical bar in the right upper corner in (a) indicate the 95% confidence interval.

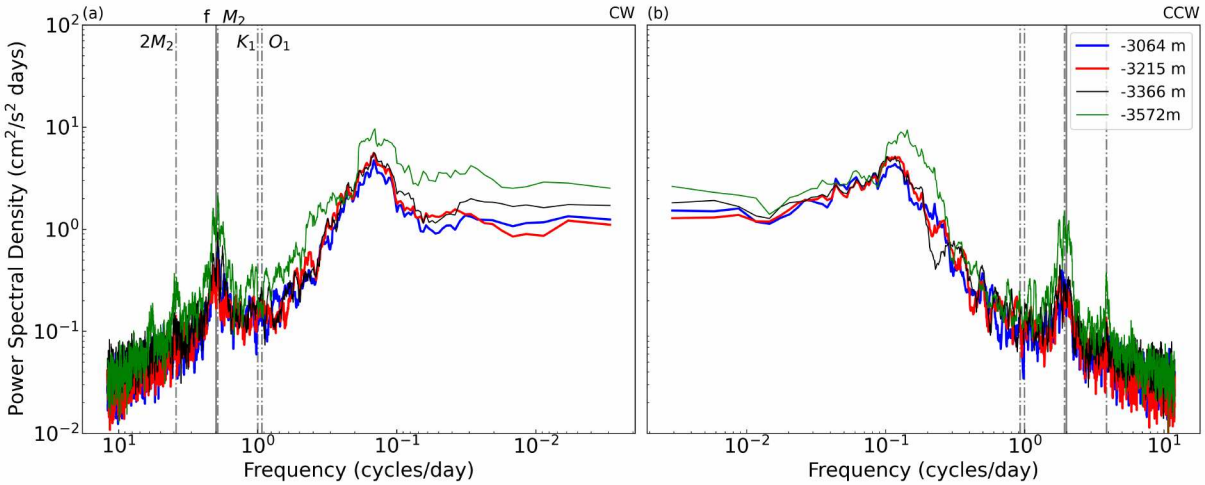


Figure 4.5: As in Fig. 4.4, but for the incoherent velocities $\mathbf{U_{it}}(\mathbf{z}, \mathbf{t})$. Note that the diurnal tidal components were removed.

peaks attributed to the diurnal tidal constituents $K_1$ and $O_1$ (Fig. 4.4). These tidal peaks do not appear in $\tilde{\mathbf{U}}_{\mathbf{it}}(\mathbf{z}, \omega)$ (Fig 4.5), which may be related to the presence of diurnal barotropic tides at the mooring site.

An energetic peak at $2M_2$ is evident in both spectra (Fig. 4.4 - 4.5), providing clear evidence for the presence of semi-diurnal tidal harmonics. The *CW* spectrum around this peak ($2M_2$) is broader than *CCW* (Fig 4.6). This suggests that the semi-diurnal

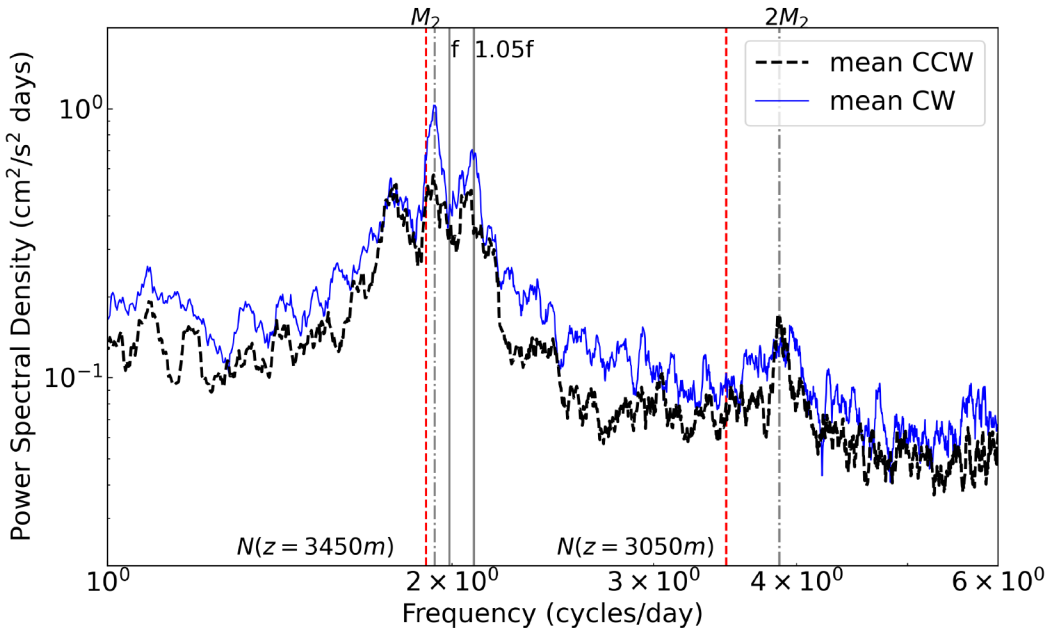


Figure 4.6: Depth-averaged frequency spectra of $\mathbf{U_{it}}(\mathbf{z}, \mathbf{t})$ for $CW$ (solid blue line) and $CCW$ (dashed black line) components. The vertical gray solid lines represent the tidal constituents $M_2$, the first semidiurnal tidal harmonic $2M_2$. The gray dashed lines are Coriolis frequency $f$ at the mooring site and $1.05f$. The red lines are the buoyancy frequency $N$ from the site 22 (see Fig 4.1) at 3050m and 3450m.

harmonics may be generated at the bottom, perhaps by topographic interaction with the nearby sea mount (Fig. 4.1), which manifests itself in a sharp $2M_2$ peak. Furthermore, the frequency is lower than the local buoyancy frequency $2M_2 < N$ at all depths, suggesting that the harmonics are evanescent and may be trapped as they cannot propagate freely, potentially broadening the $CW$ component by transferring energy to the other scales or undergoing mixing.

### 4.3.2 Near-inertial internal waves

Although there is much to be explored regarding tides and tidal harmonics, our focus lies on the near-inertial motions that are of interest. As we described in Sec. 4.2, $\mathbf{U_f}(\mathbf{z}, \mathbf{t})$ contains the near-inertial motions associated with surface-generated waves and the semi-diurnal baroclinic tides. In Fig. 4.6, two peaks with similar spectral power are evident at $M_2$ and $1.05f$ in the depth-averaged $\tilde{\mathbf{U}}_{\mathbf{it}}(\mathbf{z}, \omega)$. The mean $CW$ component is marginally larger than $CCW$, accounting for 57% of the total spectral power. At this latitude the semi-diurnal internal tides generated by topographic interaction are evanescent, $M_2 < f$, and cannot propagate freely, in addition the

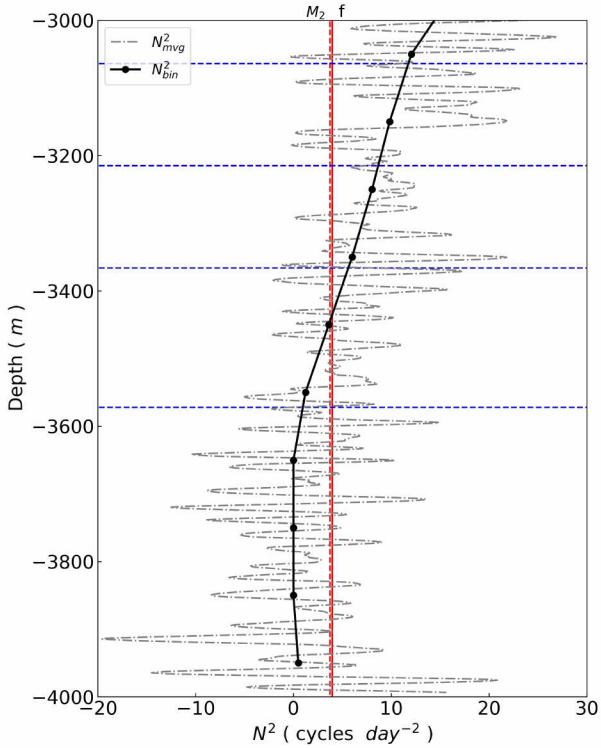


Figure 4.7: Buoyancy frequency vertical profile at site 22 (see Fig. 4.1) of the 100m-running-averaged (gray line) and the 100m-binned (black line).The red vertical dashed (solid) line is the Coriolis (semi-diurnal tidal) frequency $f$ ($M_2$). The horizontal dotted blue lines are the depths of the measurements.

stratification below the deepest measurement (-3752m) is $[M_2, f] > N$ (refer to Fig. 4.6). This is known as turning depth (see Chapter 3), and it suggests that internal waves coming from the surface cannot propagate further (Javam et al., 2000; Paoletti & Swinney, 2012b), instead they reflect and their amplitude decreases exponentially with distance (Paoletti & Swinney, 2012b; Sutherland, 2010c). In contrast, internal waves generated below a turning depth are evanescent but they can reach a depth $[M_2, f] < N$ where the energy is transferred into propagating internal wave (Lee et al., 2020b). For instance, barotropic tides can generate internal tides by topographic interaction but the radiated power is much weaker than in cases without turning depths (Paoletti et al., 2014b).

## 4.4 Propagation under weak stratification

The weak stratification at the mooring site modifies the wave propagation and thus the spatial pattern of wave energy. For near-inertial internal waves and semi-diurnal

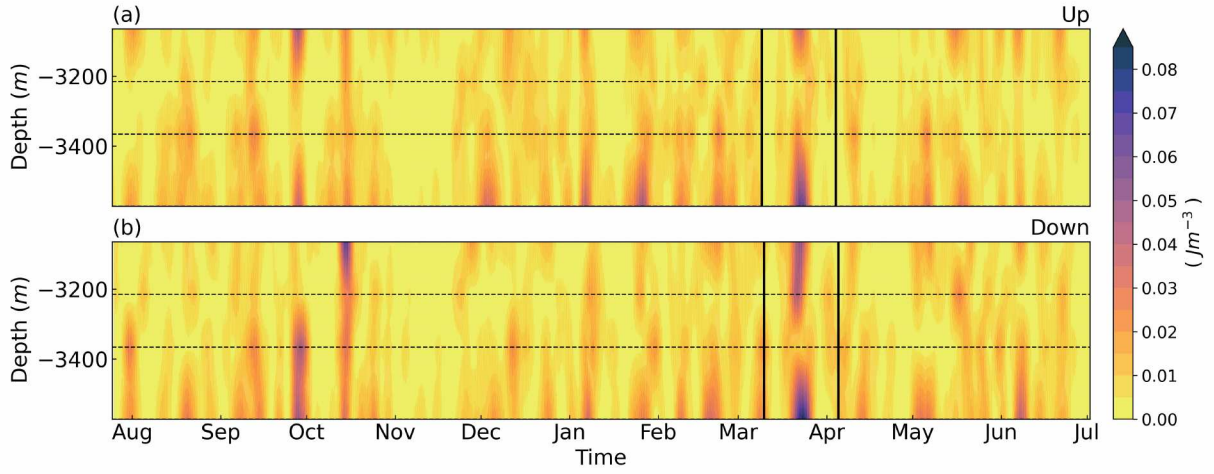


Figure 4.8: Hourly time series of the near-inertial kinetic energy (a) $KE_{up}(z,t)$ and (b) $KE_{dn}(z,t)$. The horizontal dotted black lines are the depths of the measurements. The vertical black lines represent the time period used to illustrate the reflection in Fig 4.11.

baroclinic tides, whose frequency is $\sim N$, we expected wave reflection of downward propagating internal waves at the turning depth or at the bottom (3970 m). The aim of this section is to investigate this possibility.

### 4.4.1 Model setup and numerical simulations

Numerical simulations are used to investigate the effect of weak stratification on the near-inertial wave energy vertical structure. The simulations are performed using the MITgcm model in the non-hydrostatic configuration (Marshall et al., 1997).

With the present data and without more observations at upper depths, it is difficult to detect downward propagating waves. However, the one-year velocity time series recorded at the mooring site may have captured some of the time-averaged characteristics of the internal wave field, which may be influenced by the weak stratification. We observed that the kinetic energy of the near-inertial internal waves showed no clear seasonality (Fig. 4.8), but instead appeared to propagate transiently. We therefore carried out numerical simulations of a downward propagating internal wave until the model reached steady state, and used the last $\approx 10$ wave periods of the simulation to compare with the time-averaged observations.

The model solved the two-dimensional ($z$–$x$) fully-non-linear Navier-Stokes equations. The domain has a spatial resolution of $\Delta x = 50\,\mathrm{m}$ in the $x-$direction and $\Delta z = 10\,\mathrm{m}$ in the vertical, with a total depth and a horizontal extent of 3950 m and 102.35 km respectively. The domain is horizontal-periodic and includes a 20 km-sponge layer at the east boundary, where horizontal velocities ($u$, $v$) and temperature ($\theta$) are restored to the initial conditions, dampening wave propagation. Rigid-lid and no-slip conditions were applied at the boundaries, while a quadratic bottom drag with a coefficient of $C_D = 0.001$ was used at the bottom.

The horizontal momentum viscosity and thermal diffusivity were set as $\kappa = \mu = 0.1\,\mathrm{m^2\,s^{-1}}$. In the vertical we set them to zero to allow the forcing and bottom friction to drive the vertical dynamics alone. We used the linear equation of state $b = g\alpha_\theta\theta'$, in which $\alpha_\theta = 2\times10^{-4}\ ^\circ C$ is the thermal expansion coefficient. We set $\Delta t = 10\,\mathrm{s}$ for all simulations.

To simulate a downward propagating wave, we relaxed the horizontal velocities $u$ and $v$, and the buoyancy $b$ fields, to the polarization relation of an internal gravity wave as follows (see appendix B),

$$u_m(x,z,t) = -\imath m\Psi(x,z,t). \tag{4.1}$$

$$v_m(x,z,t) = -\frac{fm}{\omega}\Psi(x,z,t). \tag{4.2}$$

$$b_m(x,z,t) = \frac{N^2k}{\omega}\Psi(x,z,t). \tag{4.3}$$

in which, $k$ and $m$ represent the horizontal and vertical wavenumbers, $N^2$ is the squared buoyancy frequency at the generation depth, $f$ is the Coriolis frequency at the mooring site (Fig. 4.1) and $\omega$ is wave frequency. For all simulation, we chose $\omega = 1.05f$ which is the near-inertial energy peak observed in Fig. 4.6.

The streamfunction $\Psi(z,x,t)$ is defined by

$$\Psi(z, x, t) = Ae^{kx+mz-\omega t}. \tag{4.4}$$

with amplitude $A$ chosen to be consistent with the observed velocities $\mathbf{U_f}(\mathbf{z}, \mathbf{t})$ in Fig 4.11.

The equations 4.1–4.3 require a constant value of $N$ (see B). Therefore, a stratification profile was generated with $N = 7$ for $z \leq$1 km, i.e. waves begin to propagate in the deep ocean. The observed bin-averaged (King et al., 2012a) stratification shown in Fig. 4.7 (corresponding to site 22 in Fig. 4.1) is used for $z >$1 km. The transition between these two regions is smoothed by a $\tanh(z)$ function.

The wave field has been set to be one wavelength away from the western boundary and to have a decay of $1/4\lambda_z$ and $1/4\lambda_x$. We set $m$ to be consistent with observations in the Arctic Ocean. For example, in the upper ocean, spectral analysis suggests internal waves with vertical wavelength ($\lambda_z = 2\pi/m$) $<$100 m (Halle & Pinkel, 2003; Wang et al., 2023; Kawaguchi et al., 2019; Athanase et al., 2019). The $\lambda_z$ increases with depth (for decreasing $N$), since we assumed that waves with local $N$ start to propagate at 1500 m, we run simulations with $\lambda_z >$100 m. In particular, we used $\lambda_z$ = 150, 250, 350 and 500 m.

The wave forcing is periodic with a time resolution of $T/100$, in which the wave period is $T = 2\ \pi/\omega$. The temporal resolution of the instantaneous velocities $u_m$ and $v_m$ (Fig 4.9) is $\omega/8$ intervals.

Similarly to $KE_{dw}$, we calculate the downward kinetic energy $KE_{model} = \frac{1}{2}\rho(u_m^2 + v_m^2)$ with $\rho$ =1024 kg m$^{-3}$ and then we averaged in time.

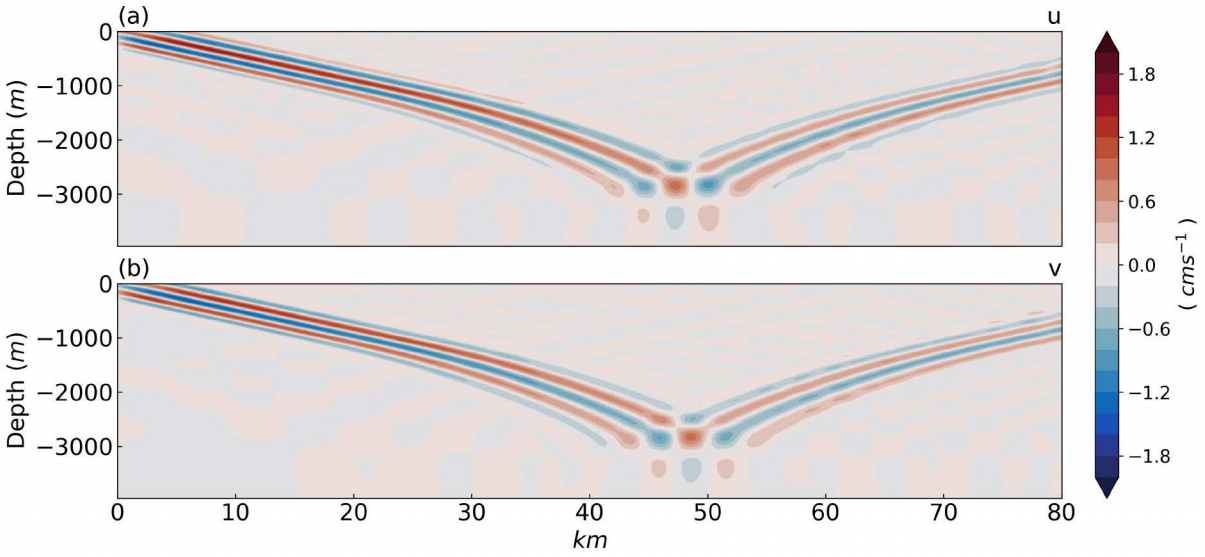


Figure 4.9: Snapshot of the instantaneous velocity components (a) $u(z, x)$ and (b) $v(z, x)$ for the simulation with initial vertical wavelength $\lambda_z$ =350 m.

### 4.4.2 Time-averaged kinetic energy

The vertical $KE_{up}$ and $KE_{dw}$ components show large variability with no clear seasonality (Fig. 4.8). In general, there are more energetic periods in the deepest and the shallowest current measurements, particularly for $KE_{dw}$. The periods between Oct-Nov 2022 and Mar-Apr 2023 are particularly energetic for both components, but only at 3064 m and 3572 m, while the intermediate measurements have lower kinetic energy. Some of the energetic periods appear to be coherent with depth for both components, which may be related to the influence of tides.

The downward time-averaged kinetic energy $KE_{dw}$ is minimally larger than the upward component $KE_{up}$ (Fig. 4.10), which is consistent with the spectra in Fig. 4.6. At 3572 m the kinetic energy is 37.1 % and 36.4 % of the total kinetic energy ($KE_{dw} + KE_{up}$), whereas at a depth of 3215 m it is only 18.1 % and 16.8 % for $KE_{dw}$ and $KE_{up}$ respectively. The time-averaged $KE_{model}$ and $KE_{dw}$ comparison shown in Fig. 4.10 for different $\lambda_z$ shows a larger $KE_{dw}$ than the model at all depths except at 3366 m.

$KE_{model}$ decreases with $\lambda_z$ and the maximum in $KE_{model}$ is at the same depth (3385 m) regardless of $\lambda_z$ and coincides with the expected turning depth, $\omega = N(z)$. Below the turning depth $KE_{model}$ decreases, which did not occur in the observations.

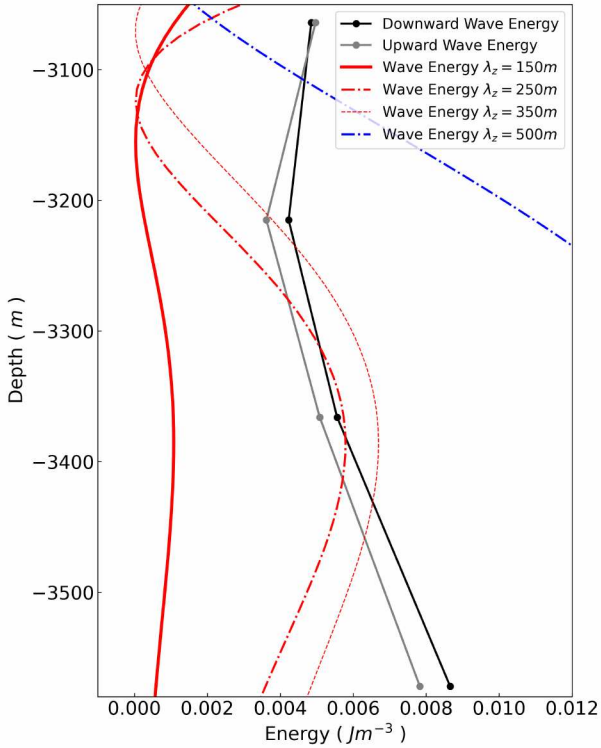


Figure 4.10: Time-averaged vertical of $KE_{dn}(z)$ (black line), $KE_{up}(z)$ (gray line), and $KE_{model}(z)$ from simulation with initial vertical wavelength $\lambda_z$ =150 m (solid red line), $\lambda_z$ =250 m (dashed red line), $\lambda_z$ =350 m (dotted red line) and $\lambda_z$ =500 m (blue line).

This difference may be related to the transient generation of baroclinic tides or lee waves by topographic interaction, which modifies the time-averaged $KE_{dw}$. Another explanation may be related to an incorrect estimation of $N$ due to its temporal variability, since we used only one profile, which may not be representative for the whole period, especially if the hydrothermal vents generate a buoyancy flux. There is also an error associated with the vertical averaging of $N$ due to its variability (see $N^2_{mvg}$ in Fig. 4.7). For example, the 100m bin-averaged method (King et al., 2012a) at 3450 m shows uncertainties $N$ =0.96$f$ ±0.36$f$.

The minimum $KE_{model}$ relative to other depths moves down for shorter $\lambda_z$ showing some qualitative agreement with $KE_{dw}$, in contrast $\lambda_z$ = 500 m differs completely from $KE_{dw}$ both qualitatively and quantitatively. This result suggests that shorter waves explain better the vertical kinetic energy distribution, which is consistent with observations in the upper ocean ($\lambda_z < 100$ m). However, in the simulations the internal waves start to propagate from a constant $N$ representative of 1000 m depth.

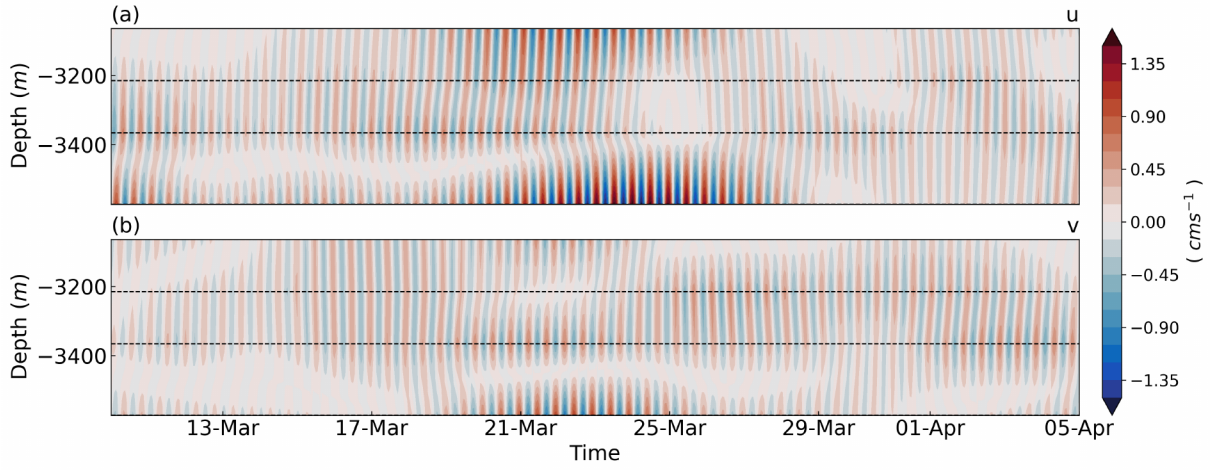


Figure 4.11: Hourly time series of (a) $u(u,t)$ and (b) $v(z,t)$ for the time period described in Fig.4.8. The horizontal dotted black lines are the depths of the measurements. Notice that $u, v$ are the real and imaginary parts of $U_f$.

We can estimate the change in $\lambda_z$ with depth. For example, assuming $\lambda_z$ = 30-100 m at the surface, for a wave with frequency =1.05$f$, the wavelength increases to $\lambda_z$ = 120-400 m at 1000 m. Thus, the values of $\lambda_z$ used in the model are consistent with observations if the wavelength increases with depth, and the simulation $KE_{model}$ with $\lambda_z$ =150 m is qualitatively closest to $KE_{dw}$, but with smaller magnitude.

Based on the results presented in this section, we propose that the time-averaged $KE_{dw}$ is related to the yearly averaged kinetic energy, which is partially explained by the transient reflection of downward propagating internal waves. We have found evidence in the observations that is consistent with wave reflection. For example, in Fig.4.11, between 17 and 21 March, the $u$ and $v$ patterns were consistent with a downward propagating internal wave. Subsequently, after 26 March, an upward propagating pattern is observed in $u$, although it is not as clear in $v$. During the reflection period, a change in velocity polarization appears at the deepest measurement, consistent with a transient reflection of a wavepacket.

## 4.5 Surface generation mechanisms for deep near-inertial internal waves

In the previous section, we presented evidence for the correlation between the averaged kinetic energy at the mooring site and transient near-inertial internal waves

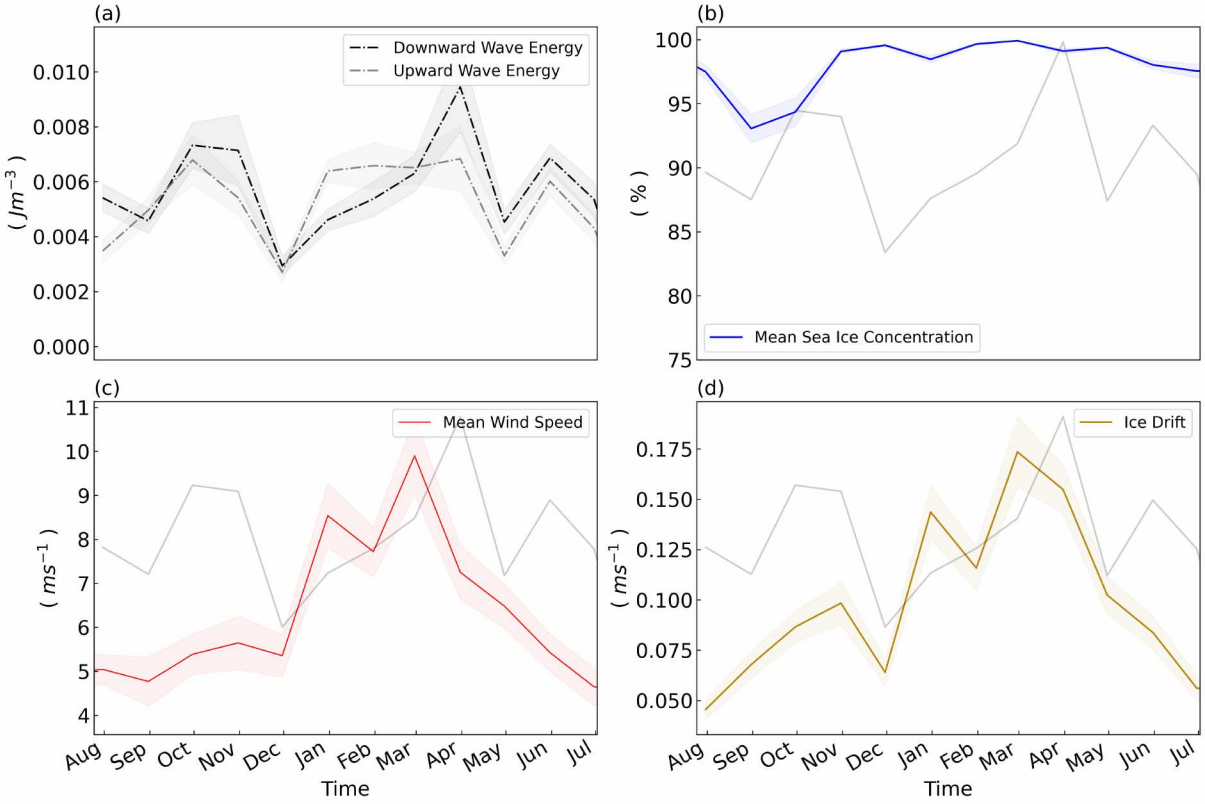


Figure 4.12: Monthly variability of (a) deep-averaged $KE_{up}$ and $KE_{dn}$. (b) Sea ice concentration. (c) Wind speed. (d) Ice drift speed. The data was binned by months and the shadows indicates the standard error. The deep-averaged $KE_{dn}$ in (a) is shown in panels (b,c,d) for comparison.

reflected due to weak stratification. We also included an example of the transient reflection process in Fig. 4.11. However, the question is whether wind in the presence of sea ice can generate near-inertial internal waves at the surface that propagate down to the mooring site. In this section we aim to identify the surface mechanisms responsible for the observed deep near-inertial kinetic wave energy.

### 4.5.1 Monthly variability: wind and sea ice properties

In Fig. 4.12, we examine the monthly averaged variability and the correlation between the near-inertial wave kinetic energy, wind and sea ice properties.

The monthly average of downward kinetic energy ($KE_{dn}$) presents two peaks, the first occurring during 1 October-1 November (0.007 $\pm$0.001 J m$^{-3}$), when the sea ice concentration (94 $\pm$ 1 %) is at its lowest and the ice drift speed peaks (0.09 $\pm$ 0.009 m s$^{-1}$), after having increased continuously during the previous months. The

latest $KE_{dn}$ maxima occur between 1 March and 1 May, in which April has the maximum $KE_{dn}$ (0.009 $\pm$0.0003 J m$^{-3}$) when sea ice concentration is always >95%, but the wind (9 $\pm$ 0.7 m s$^{-1}$) and ice drift speed (0.17 $\pm$ 0.01 m s$^{-1}$) peak in March. Although peaks in $KE_{dn}$ seemed to be associated with the lowest ice concentration and increased ice drift during the first period, and with increased wind and ice drift speed during the second period, they are not statistically correlated. Only the total energy ($KE_{dn} + KE_{up}$) was found to have a positive monthly correlation with ice drift ($r$ =0.62), meaning that the averaged response of sea ice movement is related to the total kinetic energy on a monthly scale.

### 4.5.2 Wind factor

We expected the near-inertial wave field to be significantly influenced by the transfer of momentum from wind-driven ice motion into the ocean. However, this process is complex. It depends on the properties of the sea ice, the air-ice-water drag and their interaction. The wind factor, which is the ratio of ice drift speed to wind speed, given as $W_F = |\mathbf{u}_{ice}|/|\mathbf{u}_{wind}|$, relates the response of the ice to wind forcing. A high value implies that the wind can significantly accelerate the sea ice through air-sea drag or low ice-water drag. Conversely, a low value of $W_F$ indicates that the wind cannot move the ice due to low air-ice drag or high ice-water drag. These air-ice-water drag coefficients depend in part on sea ice properties such as thickness, roughness and internal ice stress. Thus, $W_F$ captures the readiness of the ice to move under wind forcing (Dosser & Rainville, 2016b; Martini et al., 2014).

The wind speed and sea ice drift are highly correlated ($r$ =0.94), as expected. However, neither the wind speed nor the ice drift appears to account for the monthly variations observed in $KE_{dn}$. Fig. 4.13 shows a significant correlation between $W_F$ and $KE_{dn}$ ($r$ =0.68), indicating that fluctuations in sea-ice properties on a monthly basis affect the average energy of the wind-generated near-inertial wave field.

A direct response of the surface wind-driven mechanism to the deep near-inertial motions is suggested by the correlation between $W_F$ and $KE_{dw}$. In reality, the internal wave energy propagates with the $C_g$, which depends on the stratification and the shear background. If the observed deep near-inertial motions were generated

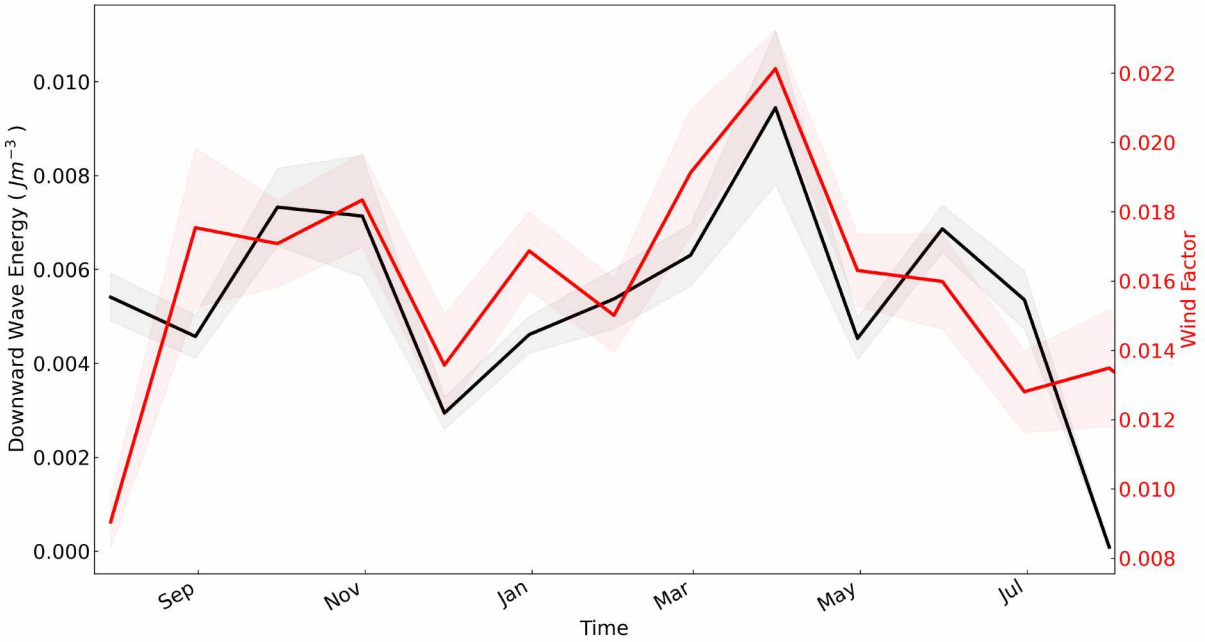


Figure 4.13: Monthly variability of near-inertial downward energy $KE_{dn}$ (black line) and the wind factor (red line). The data was binned by months and the shadow represents the standard error

in response to wind and sea-ice perturbations, we expected a lag in the temporal response, which would include both the time taken for the wind to move the sea-ice and for the internal waves to propagate to the seafloor. For the monthly correlation to remain valid, the time interval must not exceed one month. This means that a surface event that generates waves in the first half of the month is part of the monthly average if $\leq 15$ days. To investigate this lag, we performed a lag correlation analysis (Ebisuzaki, 1997) on the daily averaged time series using a 95 % bootstrapped confidence interval with 1000 repetitions. Internal wave correlations, leading surface variables and correlations with non-physical meaning are excluded from the following results.

### 4.5.3 Lag-correlation: surface-generated bottom-reached near-inertial internal waves

Fig. 4.14 shows the hourly time series of all variables (except the daily time series of ice drift). The depth-averaged $KE_{dw}$ and $KE_{up}$ are correlated ($r$ =0.77), but some $KE_{dw}$ events appear to lead $KE_{up}$, particularly during periods of lower sea ice concentration and when kinetic energy is at a maximum. They are lag-correlated with

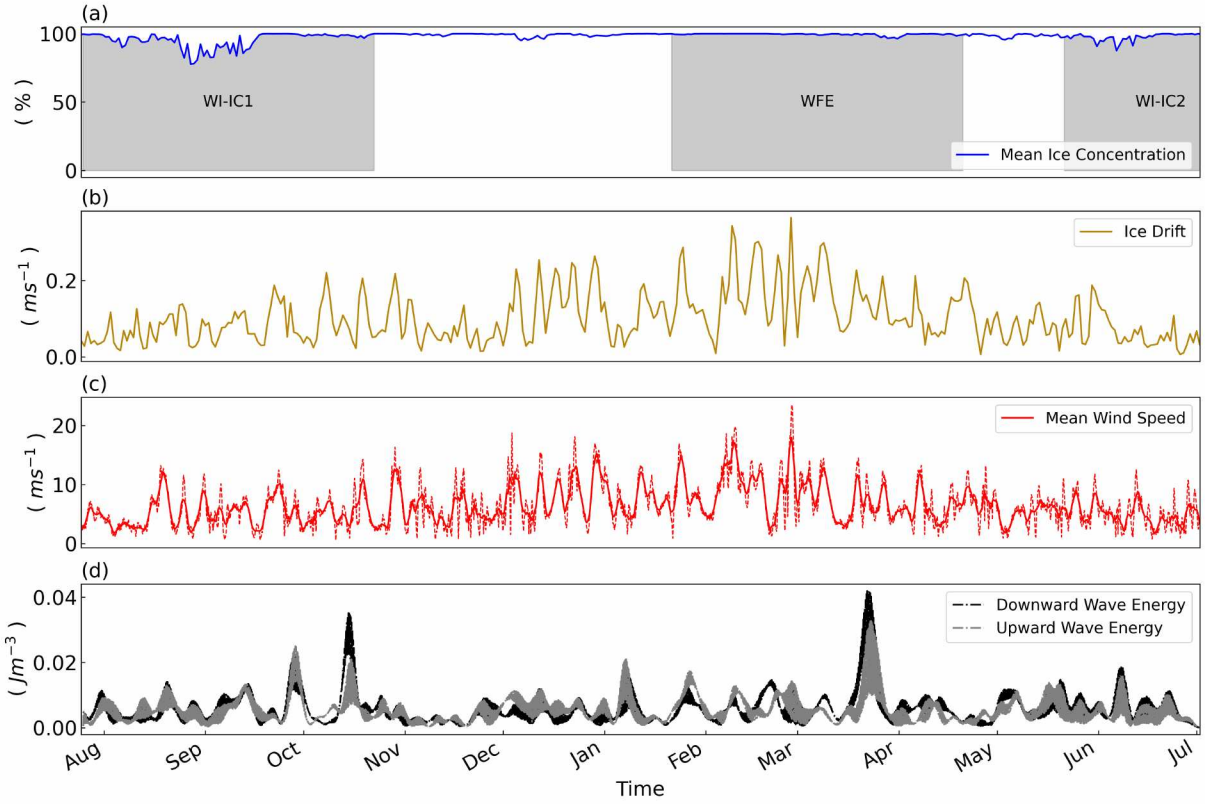


Figure 4.14: Hourly time series of (a) Sea ice concentration. (c) Wind speed. (d) deep-averaged $KE_{up}$ and $KE_{dn}$. and daily time series of (b) Ice drift.

$KE_{dw}$ leading $KE_{up}$ by one ($r$ =0.76), two ($r$ =0.62) and three days ($r$ =0.41). This may be related to the downward propagating internal wave being reflected upward, which is consistent with the results of Sec. 4.4. We also found a lag correlation of one ($r$ =0.62) and two ($r$ =0.41) days of $KE_{up}$ preceding $KE_{dw}$ which may be related to upward propagating bottom-generated internal waves.

There is no lag correlation between any of the variables when the full time period is used (except for wind and ice drift, which are correlated with $r$ =0.77). However, if there is a lag correlation between surface wind-ice motions and deep near-inertial internal waves that depend on sea ice properties, as suggested by the $W_F$–$KE_{dw}$ correlation, this lag correlation is likely to vary from a few weeks to a month depending on the season. Thus, it may not be appropriate to use the full time series in this situation. We therefore performed a lag correlation analysis for a window of 60 days, shifted by 30 days to the end of the time series.

The results were divided into three time periods (refer to Fig 4.14) according to the variables involved. Two of these periods, corresponding to the minimum in sea-ice concentration, labelled WI-IC1 (25 July - 23 October) and WI-IC2 (21 May - 20 July), showed a lagged correlation between wind and ice drift speed with $KE_{dw}$. In contrast, during the period designated as WFE (Jan 21 - Apr 21), corresponding to a maximum in wind speed and ice drift, there was a correlation between $W_F$ and $KE_{dw}$.

During the WI-IC1 period, the correlation between wind and $KE_{dw}$ was significant for 26 ($r$ =0.54) and 22 ($r$ =0.49) days, whereas the correlation between ice drift and $KE_{dw}$ was shorter, only 19 ($r$ =0.5) and 21 ($r$ =0.6) days. Similarly, the correlation in WI-IC2 gives 22 days ($r$ =0.55) for wind and $KE_{dw}$, and 21 days ($r$ =0.6) for ice drift and $KE_{dw}$. In particular, WI-IC1 and WI-IC2 coincide with the period when sea ice concentration was at its minimum for more than a month. This result suggests that deep near-inertial internal waves respond to surface motions. The correlation between wind and internal waves takes a few days longer than for ice drift, as it could be expected.

During the period WFE, in which the sea ice concentration $> 95\,\%$, there is correlation only for $KE_{dw}$ and $W_F$, corresponding with the interval of maximum ice drift and wind speed, and $KE_{dw}$. The correlation is for 15 ($r$ =0.58) and 16 ($r$ =0.51) days. If we consider these periods as the time of wave propagation and shift $W_F$ by 15 days, the monthly mean $W_F$ and $KE_{dw}$ (Fig. 4.12) correlation increases from $r$ =0.68 (without time shift) to $r$ =0.73.

The previous results can be interpreted as follows. The wind transfers momentum to near-inertial surface motions through the sea ice, which generate near-inertial internal waves that propagate downward to the mooring site in less than 26 days (e.g., $\sim$ 15 days). The wind–$KE_{dw}$ and ice drift–$KE_{dw}$ correlation during periods of relative low sea ice concentration and the opposite for the $W_F$–$KE_{dw}$ correlation are reasonable if we assume that there is a seasonal variability in the mechanisms that generate near-inertial internal waves. The wind and sea ice motions are more likely to be associated with internal waves during minimum sea ice concentration, which becomes a pure wind-wave correlation in the absence of sea ice. In contrast, during

periods of relative high sea ice concentration, the interplay between wind and sea ice properties captured in $W_F$ is more likely to be correlated with internal waves.

## 4.6 Summary & Conclusion

We have used observations of deep currents, wind speed and sea ice products, and simulations to study the deep near-inertial motions at the Aurora vent site in the Eurasian Basin of the Arctic Ocean. Our analysis and interpretation are summarized below:

- The current observations suggest the presence of upward and downward near-inertial internal waves at the mooring site between 3064 and 3572 m depth, which are more energetic during periods of maximum wind and ice drift speed or minimum sea ice concentration.

- We propose that the observed time-averaged vertical structure of the kinetic energy associated with near-inertial internal waves is related with the average response of transient reflection of internal waves. As an example, between 17 and 21 March, a downward propagating internal wave is shown to undergo reflection within a week.

- Wind and sea ice properties might be the drivers of the observed near-inertial internal waves. The wind and sea ice motions are more likely to be associated with internal waves during minimum sea ice concentration. In contrast, during full sea ice cover, the interplay between wind and sea ice properties, captured by the wind factor, is more likely to be correlated with internal waves.

- We hypothesize that internal waves generated at the surface under sea-ice reach the seafloor after $\sim$ 15-26 days.

The evidence presented in this study cannot prove with certainty that the observed near-inertial internal waves were generated at the surface, nor that they were reflected due to weak stratification. However, we have provided evidence for these processes and we have presented various arguments based on statistical analysis and model simulations that support this idea. Further observations, analysis and three-dimensional simulations are needed to fully understand the generation and propagation of internal waves in the Arctic Ocean. As the sea-ice cover is constantly decreasing, understanding these processes is crucial for correctly representing future changes in the Arctic Ocean and its state in climate projections.

# Chapter 5

# 5 General conclusion

## 5.1 Key findings

The objective of this thesis was to provide new results on internal wave propagation in the Arctic Ocean. A combination of observations, numerical simulations and theoretical analysis has been used to address the three main questions mentioned in the introduction, which were the motivation for this thesis and the subject of chapters 2-4. The main results are presented below:

**What is the transmission process of the transient interaction between an incident vertically localized internal wavepacket and a density staircase?**

We have performed numerical simulations to investigate the effect of this near-resonant coupling when a vertically localized, quasi-monochromatic internal wavepacket interacts with a density staircase. We have demonstrated a close correspondence between the frequency of incident waves at a transmission spike and the frequency of modes at the same horizontal wavenumber. However, the corresponding modes decay exponentially with time. In a series of simulations with fixed incident wave frequency and varying horizontal wavenumber, the measured transmission coefficient does not exhibit transmission spikes, but decreases monotonically with increasing horizontal wavenumber about the critical wavenumber separating strong and weak transmission. We have shown that this occurs because the incident wave excites modes that then slowly transfer energy above and below the staircase. The decay rate is slower for staircases with more steps, with the decay time increasing as the cube of the number of steps.

**Do near-inertial turning depths exist in the Deep Canadian Basin and what are the consequences of turning depths for deep mixing?**

We estimated the distribution of near-inertial turning depths from temperature and salinity data from 2005 to 2014. Near-inertial turning depths are ubiquitous in the deep Canadian Basin at $\sim 2700\,\mathrm{m}$ depth, between 100 and 1200 m above the bottom,

which is consistent with the thickness variability of the deep homogeneous layer. This deep layer below 3300 m is characterized by small squared buoyancy frequencies $N^2 \sim 0$ with locally unstable layers ($N^2 < 0$). Near-inertial internal waves are reflected from the turning depths, so their contribution to deep mixing is limited. The penetrative wave flux below the turning depth, depends on the horizontal wavenumber at the turning depth, and then the wave flux decreases exponentially with distance. Upon reflection, this evanescent perturbation can interact with the bathymetry, especially over slopes and ridges where the height of the turning depth above the seafloor is small. After reflection, most of the wave energy is trapped between the turning depth and the surface, so any potential increase in wave energy input may not only affects the deep mixing but also the mixing of mid-depth water masses such as the Atlantic Water.

**Do near-inertial internal waves reach the bottom in the Eurasian Basin of the Arctic Ocean after surface generation by a combination of wind and sea ice properties?**

In the Canadian Basin, an increase in near-inertial wave amplitude and kinetic energy has been observed, along with enhanced wind-driven vertical heat fluxes and dissipation rates, particularly in the upper column. In the deep ocean beyond the critical latitude, internal near-inertial waves are expected to contribute to mixing in the interior, but the extent of their influence remains unclear. In Chapter 4, I presented groundbreaking deep current observations from a mooring on the Gakkel Ridge in the Eurasian Basin at 82.53°N. The presence of barotropic diurnal and semidiurnal tides, along with semidiurnal harmonics, adds complexity to the interaction of internal waves. By analyzing the observed downward and upward wave kinetic energy in relation to factors such as wind speed, sea ice properties, and numerical simulations, I explored the likely surface origin of near-inertial waves. In particular, there is a lagged correlation of less than 26 days between ice drift speed and downward wave energy, and about 15 days between wind factors and downward wave energy. Evidence for wave reflection is also identified and discussed, with emphasis on its implications for surface-generated near-inertial internal waves.

# 6 Outlook

The findings and main points discussed at the end of Chapters 2-4 can be seen as a starting point for future research. Here I have summarized the most relevant ideas for each chapter.

**Transient internal wave excitation of resonant modes in a density staircase**

Exploiting the 2D configuration, some simulations can be performed to investigate the extent to which the transient transmission of a wavepacket is modified by shear, including the effect of rotation. Weak non-linear effects of non-hydrostatic wavepackets can also be assessed with numerical simulations.

The mechanism behind the internal wave-driven instability of the staircases towards mixing can be addressed using 3D numerical simulations, linear theory and stability analysis.

In addition, more observations are needed to study not only the internal wave transmission through a density staircase and the existence of interfacial waves, but also the mixing process derived from these interactions. Efforts should be made to deploy a mooring array with instruments such as CTDs or current meters covering the thermohaline staircases. In addition, autonomous vehicles can be equipped with shear probes that can directly measure energy dissipation.

**Near-inertial wave propagation in the deep Canadian Basin: Turning depths and the homogeneous deep layer**

Data acquisition is essential to study internal waves in the deep Arctic and their connection to mixing. Reliable long time series (at least one year to capture the seasonal variability of sea ice cover) of currents, temperature and salinity can be measured using moorings, inverted echo sounders and autonomous vehicles. In particular, the upper 1000 m above the seafloor, away from and on the slope or near rough bathymetry, as well as at and beyond the critical latitude, are needed to investigate the extent to which turning depths affect deep mixing.

In the absence of a more appropriate set of observations, numerical simulations can be used to investigate wave-driven deep mixing upon reflection. Assuming that waves are evanescent below the turning depth, 2D and 3D model configurations can be used to quantify the attenuation of evanescent waves by topographic stress or dissipation for different wavelengths and distances to the bottom. In addition, analogous to Chapter 2, the transient reflection of a wavepacket, including topographic effects, can be assessed instead of using a wave beam.

A similar approach can be used to study the interaction of near-inertial internal waves reflected from beneath the sea ice.

**Observations of deep near-inertial internal waves in the Eurasian Basin under weak stratification**

Despite the availability of tidal models for the Arctic Ocean, observations are needed for their calibration and full validation. Moorings need to cover most of the water column to approximate the barotropic tidal components, which would also help to study baroclinic tidal generation beyond the critical latitude and the associated energy transfer.

Tidal harmonics are also present in the data, the mechanism by which the semidiurnal baroclinic tide transfers energy to the harmonics beyond the critical latitude is not fully understood, and the theory of parametric subharmonic instabilities can be modified to include evanescent waves. This process becomes more complex when we consider that both the baroclinic waves and the wave harmonics are evanescent, i.e. trapped, and must dissipate close to the generation zone, which may be directly related to deep mixing.

In the raw velocity spectrum there is a peak with a frequency similar to the depth-averaged $N$ ($\sim 8$ hr) at the mooring site. At first sight, a plausible explanation is that the hydrothermal vents expel a vertical flux of momentum and heat, perturbing the adjacent water parcel and exciting internal waves at the local buoyancy frequency. Unexpectedly, after harmonic analysis (with all components, but not when only the main diurnal and semi-diurnal components are used), the peak was removed. These internal waves may exist, and an explanation for this problem may be that

these buoyancy internal waves are generated quasi-stationarily or at quasi-regular intervals, so that the harmonic analysis method was able to detect them as regular tidal motions.

# A Approximate dispersion relation for highest mode

The following dispersion relation approximation for highest mode was developed by Prof. Dr. Bruce Sutherland.

Here we find an approximate analytic prediction for the frequency and decay rate of the highest mode in a density staircase, whose frequency is close to the critical transition given by (2.13), in which we assume $kL \ll 1$. Consequently $|\omega|/N_0 \ll 1$ and $|M| \simeq N_0/|\omega| \gg 1$. At the critical transition $\omega_c/N_0 = kL/2$. And so we expect $\tilde{m} \equiv mL\ (= MkL) \simeq 2 - \epsilon$ with $|\epsilon| \ll 1$. Thus $\Gamma = kL(M^2+1)/2 \simeq M\tilde{m}/2$.

The implicit relation for the dispersion relation for modes in a staircase is given generally by (2.16). The value of $b_-$ in this equation is given by (2.12), which simplifies in the $kL \ll 1$ limit to $b_- \simeq -\Gamma$. Hence (2.16) can be written as

$$-\Gamma(a_+ + a_-)^2\Lambda_-/b_0 + (a_+^2 - a_-^2)\Lambda_+ \simeq 0. \tag{A.1}$$

From the definition of $a_\pm$ in (2.6), we get the approximate expressions

$$a_+ + a_- \simeq 2 + i\tilde{m} - \tilde{m}^2/2, \quad a_+ - a_- \simeq M(2i - \tilde{m}). \tag{A.2}$$

Also using $\tilde{m} = 2 - \epsilon$, (A.1) simplifies to

$$(1 - \epsilon/2)(2i + (2-i)\epsilon - \epsilon^2/2)\Lambda_-/b_0 + (2 - 2i - \epsilon)\Lambda_+ \simeq 0. \tag{A.3}$$

To find approximate expressions for $\Lambda_\pm$, we use the definition of $b_+$ in (2.12) with $kL \ll 1$ to get

$$b_+ \simeq 1 - \tilde{m}^2/2 = -1 + 2\epsilon + O(|\epsilon|^2). \tag{A.4}$$

Hence, we find

$$b_0^2 \equiv b_+^2 - 1 \simeq -4\epsilon + O(|\epsilon|^2). \tag{A.5}$$

In the expressions for $\Lambda_\pm$, we perform a binomial expansion to write (assuming $J \geq 4$)

$$\lambda_\pm^{J-1} = b_+^{J-1} \pm \left( \begin{array}{c} J-1 \\ 1 \end{array} \right) b_+^{J-2} b_0 + \left( \begin{array}{c} J-1 \\ 2 \end{array} \right) b_+^{J-3} b_0^2 \pm \left( \begin{array}{c} J-1 \\ 3 \end{array} \right) b_+^{J-4} b_0^3 + \ldots \quad \text{(A.6)}$$

Thus we have

$$\Lambda_+ = b_+^{J-1} + (J-1)(J-2) b_+^{J-3} b_0^2/2 + \ldots \simeq (-1)^{J-1} \Big[ 1 - 2(J-1)^2 \epsilon \Big] + O(|\epsilon|^2), \quad \text{(A.7)}$$

and

$$\begin{aligned} \Lambda_-/b_0 &= (J-1) b_+^{J-2} + (J-1)(J-2)(J-3) b_+^{J-4} b_0^2/6 + \ldots \\ &\simeq (-1)^{J-1} \Big[ -(J-1) + (2/3) J (J-1)(J-2) \epsilon \Big] + O(|\epsilon|^2). \end{aligned} \quad \text{(A.8)}$$

Putting these expressions in (A.3) and keeping terms up to $O(|\epsilon|)$ gives

$$6(J+i) - \left[ 4J^3 + 12iJ^2 - (10+18i)J + (6+9i) \right] \epsilon \simeq 0. \quad \text{(A.9)}$$

From this we can solve for $\epsilon$, explicitly finding its real and imaginary parts in terms of the number of steps, $J$. For $J \gg 1$ we find

$$\epsilon \simeq (3/2) J^{-2} \left[ 1 - (7/2) J^{-2} + O(J^{-3}) \right] - 3iJ^{-3} \left[ 1 - (9/4) J^{-1} - (13/8) J^{-2} + O(J^{-3}) \right]. \quad \text{(A.10)}$$

# B Polarization relation and initial conditions

To derive the polarization relation of internal gravity waves in Eq. 4.1– 4.3, we start with the non-hydrostatic, ($x$–$z$), linearized, inviscid, Boussinesq equations in the $f-$plane:

$$u_t - fv = -P_x. \tag{B.1}$$

$$v_t + fu = 0. \tag{B.2}$$

$$w_t - b = -P_z. \tag{B.3}$$

$$b_t - wN^2 = 0. \tag{B.4}$$

$$w_z + u_x = 0. \tag{B.5}$$

Here, $u$, $v$ and $w$ are the horizontal and vertical velocity components. $f = 2\Omega \sin\phi$ is the Coriolis frequency, where $\phi$ is the latitude and $\Omega$ is the angular velocity of the Earth. $N$ is the buoyancy frequency. $P = p/\rho_0$ is the deviation of the pressure from the state of rest and $\rho_0$ is the reference density. The buoyancy perturbation is defined as $b = -g\rho/\rho_0$, in which $\rho$ is the density deviation from the mean background density $\bar{\rho}$.

We define the streamfunction $\Psi$ such that satisfies the continuity equation B.5.

$$u = -\Psi_z, \qquad\qquad w = \Psi_x. \tag{B.6}$$

In an homogeneous medium, we can assume plan wave solutions in the form of Eq. 4.4. After substitution of $\Psi$ in Eq. B.1–B.6, we recovered the polarization relation in Eq. 4.1–4.3. Note that we can also derive the polarization relation for $w$ and $P$, which we have included for completeness.

$$w(x,z,t) = -\imath k \Psi(x,z,t). \tag{B.7}$$

$$P(x,z,t) = \imath m \frac{f^2 - \omega^2}{k\omega} \Psi(x,z,t). \tag{B.8}$$

# References


Alford, M. H. et al. (2007). "Internal Waves across the Pacific". In: *Geophysical Research Letters* 34.24, 2007GL031566. ISSN: 0094-8276, 1944-8007. DOI: 10.1029/2007GL031566.

Alford, Matthew H., Meghan F. Cronin, and Jody M. Klymak (2012). "Annual Cycle and Depth Penetration of Wind-Generated Near-Inertial Internal Waves at Ocean Station Papa in the Northeast Pacific". In: *Journal of Physical Oceanography* 42.6, pp. 889–909. ISSN: 0022-3670, 1520-0485. DOI: 10.1175/JPO-D-11-092.1.

Alford, Matthew H. et al. (2017). "Space–Time Scales of Shear in the North Pacific". In: *Journal of Physical Oceanography* 47.10, pp. 2455–2478. ISSN: 0022-3670, 1520-0485. DOI: 10.1175/JPO-D-17-0087.1.

André, Q., A. J. Barker, and S. Mathis (2017). "Layered semi-convection and tides in giant planet interiors". In: *Astronomy and Astrophysics* 605, A117.

Artana, Camila et al. (2022). "Tides, Internal and Near-Inertial Waves in the Yermak Pass at the Entrance of the Atlantic Water to the Arctic Ocean". In: *Journal of Geophysical Research: Oceans* 127.12, e2022JC019082. ISSN: 2169-9275, 2169-9291. DOI: 10.1029/2022JC019082.

Athanase, Marylou et al. (2019). "New Hydrographic Measurements of the Upper Arctic Western Eurasian Basin in 2017 Reveal Fresher Mixed Layer and Shallower Warm Layer Than 2005–2012 Climatology". In: *Journal of Geophysical Research: Oceans* 124.2, pp. 1091–1114. ISSN: 2169-9275, 2169-9291. DOI: 10.1029/2018JC014701.

Baumann, Till M. and Ilker Fer (2023). "Trapped Tidal Currents Generate Freely Propagating Internal Waves at the Arctic Continental Slope". In: *Scientific Reports* 13.1, p. 14816. ISSN: 2045-2322. DOI: 10.1038/s41598-023-41870-3.

Behrendt, Axel et al. (2017). *A comprehensive, quality-controlled and up-to-date data set of temperature and salinity data for the Arctic Mediterranean Sea (Version 1.0), links to data files*. data set. Supplement to: Behrendt, A et al. (2017): UDASH - Unified Database for Arctic and Subarctic Hydrography. Earth System Science Data Discussions, 37 pp, https://doi.org/10.5194/essd-2017-92. DOI: 10.1594/PANGAEA.872931. URL: https://doi.org/10.1594/PANGAEA.872931.

Behrendt, Axel et al. (2018). "UDASH – Unified Database for Arctic and Subarctic Hydrography". en. In: *Earth System Science Data* 10.2, pp. 1119–1138. ISSN: 1866-3516. DOI: 10.5194/essd-10-1119-2018. URL: https://essd.copernicus.org/articles/10/1119/2018/.

Belyaev, M. A., E. Quataert, and J. Fuller (2015). "The properties of g-modes in layered semiconvection". In: *MNRAS* 452, pp. 2700–2711.

Boury, S. et al. (2022). "Observations of double diffusive staircase edges in the Arctic Ocean". In: *J. Geophys. Res.* 127, e2022JC018906.

Brown, G. L., A. B. G. Bush, and B. R. Sutherland (2008). "Beyond Ray Tracing for Internal Waves. Part II: Finite-Amplitude Effects". In: *Phys. Fluids* 20. doi:10.1063/1.2993168, 106602:1–13.

Cao, Anzhou et al. (2019). "Upper Ocean Shear in the Northern South China Sea". In: *Journal of Oceanography* 75.6, pp. 525–539. ISSN: 0916-8370, 1573-868X. DOI: 10.1007/s10872-019-00520-x.

Carmack, Eddy C. et al. (2012). "The Arctic Ocean warms from below: THE ARCTIC OCEAN WARMS FROM BELOW". en. In: *Geophysical Research Letters* 39.7, n/a–n/a. ISSN: 00948276. DOI: 10.1029/2012GL050890. URL: http://doi.wiley.com/10.1029/2012GL050890.

Cole, Sylvia T. et al. (2018). "Internal Waves in the Arctic: Influence of Ice Concentration, Ice Roughness, and Surface Layer Stratification". en. In: *Journal of Geophysical Research: Oceans* 123.8, pp. 5571–5586. ISSN: 2169-9275, 2169-9291. DOI: 10.1029/2018JC014096. URL: https://onlinelibrary.wiley.com/doi/abs/10.1029/2018JC014096.

D'Asaro, Eric A. and Mark D. Morehead (1991). "Internal waves and velocity fine structure in the Arctic Ocean". en. In: *Journal of Geophysical Research* 96.C7, p. 12725. ISSN: 0148-0227. DOI: 10.1029/91JC01071. URL: http://doi.wiley.com/10.1029/91JC01071.

Dosser, Hayley V. and Luc Rainville (2016a). "Dynamics of the Changing Near-Inertial Internal Wave Field in the Arctic Ocean". In: *Journal of Physical Oceanography* 46.2, pp. 395–415. ISSN: 0022-3670, 1520-0485. DOI: 10.1175/JPO-D-15-0056.1. URL: https://journals.ametsoc.org/view/journals/phoc/46/2/jpo-d-15-0056.1.xml.

Dosser, Hayley V. and Luc Rainville (2016b). "Dynamics of the Changing Near-Inertial Internal Wave Field in the Arctic Ocean". In: *Journal of Physical Oceanography* 46.2, pp. 395–415. ISSN: 0022-3670, 1520-0485. DOI: 10.1175/JPO-D-15-0056.1.

Dosser, Hayley V., Luc Rainville, and John M. Toole (2014). "Near-Inertial Internal Wave Field in the Canada Basin from Ice-Tethered Profilers". en. In: *Journal of Physical Oceanography* 44.2, pp. 413–426. ISSN: 0022-3670, 1520-0485. DOI: 10.1175/JPO-D-13-0117.1. URL: http://journals.ametsoc.org/doi/10.1175/JPO-D-13-0117.1.

Ebisuzaki, Wesley (1997). "A Method to Estimate the Statistical Significance of a Correlation When the Data Are Serially Correlated". In: *Journal of Climate* 10.9, pp. 2147–2153. ISSN: 0894-8755, 1520-0442. DOI: 10.1175/1520-0442(1997)010<2147:AMTETS>2.0.CO;2.

Fer, Ilker (2014). "Near-Inertial Mixing in the Central Arctic Ocean". en. In: *Journal of Physical Oceanography* 44.8, pp. 2031–2049. ISSN: 0022-3670, 1520-0485. DOI: 10.1175/JPO-D-13-0133.1. URL: http://journals.ametsoc.org/doi/10.1175/JPO-D-13-0133.1.

Ferrari, R. and C. Wunsch (2009a). "Ocean Circulation Kinetic Energy: Reservoirs, Sources, and Sinks". In: *Ann. Rev. Fluid Mech.* 41. doi:10.1146/annurev.fluid.40.111406.102139, pp. 253–282.

Ferrari, Raffaele and Carl Wunsch (2009b). "Ocean Circulation Kinetic Energy: Reservoirs, Sources, and Sinks". In: *Annual Review of Fluid Mechanics* 41.1, pp. 253–282. ISSN: 0066-4189, 1545-4479. DOI: 10.1146/annurev.fluid.40.111406.102139.

Fine, Elizabeth C. and Sylvia T. Cole (2022). "Decadal Observations of Internal Wave Energy, Shear, and Mixing in the Western Arctic Ocean". en. In: *Journal of Geophysical Research: Oceans* 127.5. ISSN: 2169-9275, 2169-9291. DOI: 10.1029/2021JC018056. URL: https://onlinelibrary.wiley.com/doi/10.1029/2021JC018056.

Gerkema, T. et al. (2008). "Geophysical and astrophysical fluid dynamics beyond the traditional approximation". en. In: *Reviews of Geophysics* 46.2, RG2004. ISSN:

8755-1209. DOI: 10.1029/2006RG000220. URL: http://doi.wiley.com/10.1029/2006RG000220.

Ghaemsaidi, S. et al. (2016a). "The Impact of Multiple Layering on Internal Wave Transmission". In: *J. Fluid Mech.* 789, pp. 589–616.

Ghaemsaidi, S. J. et al. (2016b). "The impact of multiple layering on internal wave transmission". en. In: *Journal of Fluid Mechanics* 789, pp. 617–629. ISSN: 0022-1120, 1469-7645. DOI: 10.1017/jfm.2015.682. URL: https://www.cambridge.org/core/product/identifier/S0022112015006825/type/journal_article.

Gregg, Michael C. (2021). *Ocean Mixing*. 1st ed. Cambridge University Press. ISBN: 978-1-316-79543-9 978-1-107-17380-4. DOI: 10.1017/9781316795439. URL: https://www.cambridge.org/core/product/identifier/9781316795439/type/book.

Guthrie, J. D., I. Fer, and J. H. Morison (2017). "Thermohaline staircases in the Amundsen Basin: Possible disruption by shear and mixing". In: *J. Geophys. Res.* 122, pp. 7767–7782.

Halle, Chris (2003). "Internal wave variability in the Beaufort Sea during the winter of 1993/1994". en. In: *Journal of Geophysical Research* 108.C7, p. 3210. ISSN: 0148-0227. DOI: 10.1029/2000JC000703. URL: http://doi.wiley.com/10.1029/2000JC000703.

Halle, Chris and Robert Pinkel (2003). "Internal Wave Variability in the Beaufort Sea during the Winter of 1993/1994". In: *Journal of Geophysical Research: Oceans* 108.C7, 2000JC000703. ISSN: 0148-0227. DOI: 10.1029/2000JC000703.

Haren, Hans van and Claude Millot (2005). "Gyroscopic waves in the Mediterranean Sea". en. In: *Geophysical Research Letters* 32.24, p. L24614. ISSN: 0094-8276. DOI: 10.1029/2005GL023915. URL: http://doi.wiley.com/10.1029/2005GL023915.

– (2006). "Determination of buoyancy frequency in weakly stable waters". en. In: *Journal of Geophysical Research* 111.C3, p. C03014. ISSN: 0148-0227. DOI: 10.1029/2005JC003065. URL: http://doi.wiley.com/10.1029/2005JC003065.

Herman, Yvonne (2012). *The Arctic seas: climatology, oceanography, geology, and biology*. Springer Science & Business Media.

Hersbach, Hans et al. (2020). “The ERA5 Global Reanalysis”. In: *Quarterly Journal of the Royal Meteorological Society* 146.730, pp. 1999–2049. ISSN: 0035-9009, 1477-870X. DOI: 10.1002/qj.3803.

Hersbach, Hans et al. (2023). *ERA5 Hourly Data on Single Levels from 1940 to Present*. DOI: 10.24381/cds.adbb2d47.

Jakobsson, Martin et al. (2012). “The International Bathymetric Chart of the Arctic Ocean (IBCAO) Version 3.0: IBCAO VERSION 3.0”. en. In: *Geophysical Research Letters* 39.12, n/a–n/a. ISSN: 00948276. DOI: 10.1029/2012GL052219. URL: http://doi.wiley.com/10.1029/2012GL052219.

Javam, A., J. Imberger, and S. W. Armfield (2000). “Numerical Study of Internal Wave–Caustic and Internal Wave–Shear Interactions in a Stratified Fluid”. In: *Journal of Fluid Mechanics* 415, pp. 89–116. ISSN: 0022-1120, 1469-7645. DOI: 10.1017/S0022112000008600.

Kawaguchi, Yusuke, Taku Wagawa, and Yosuke Igeta (2020). “Near-Inertial Internal Waves and Multiple-Inertial Oscillations Trapped by Negative Vorticity Anomaly in the Central Sea of Japan”. In: *Progress in Oceanography* 181, p. 102240. ISSN: 00796611. DOI: 10.1016/j.pocean.2019.102240.

Kawaguchi, Yusuke et al. (2019). “Year-Round Observations of Sea-Ice Drift and near-Inertial Internal Waves in the Northwind Abyssal Plain, Arctic Ocean”. In: *Polar Science* 21, pp. 212–223. ISSN: 18739652. DOI: 10.1016/j.polar.2019.01.004.

Kim, Yeon-Hee et al. (2023). “Observationally-constrained projections of an ice-free Arctic even under a low emission scenario”. en. In: *Nature Communications* 14.1, p. 3139. ISSN: 2041-1723. DOI: 10.1038/s41467-023-38511-8. URL: https://www.nature.com/articles/s41467-023-38511-8.

King, Benjamin et al. (2012a). “Buoyancy Frequency Profiles and Internal Semidiurnal Tide Turning Depths in the Oceans”. In: *Journal of Geophysical Research: Oceans* 117.C4, 2011JC007681. ISSN: 0148-0227. DOI: 10.1029/2011JC007681.

– (2012b). “Buoyancy frequency profiles and internal semidiurnal tide turning depths in the oceans: INTERNAL TIDE TURNING DEPTH”. en. In: *Journal of Geophysical Research: Oceans* 117.C4, n/a–n/a. ISSN: 01480227. DOI: 10.1029/2011JC007681. URL: http://doi.wiley.com/10.1029/2011JC007681.

Kunze, E., A. J. Williams, and R. W. Schmitt (1987). "Optical microstructure in the thermohaline staircase east of Barbados". In: *Deep-Sea Res.* 34, pp. 1697–1704.

Kwok, R (2018). "Arctic sea ice thickness, volume, and multiyear ice coverage: losses and coupled variability (1958–2018)". In: *Environmental Research Letters* 13.10, p. 105005. ISSN: 1748-9326. DOI: 10.1088/1748-9326/aae3ec. URL: https://iopscience.iop.org/article/10.1088/1748-9326/aae3ec.

Langseth, M. G., A. H. Lachenbruch, and B. V. Marshall (1990). "Geothermal observations in the Arctic region". en. In: *The Arctic Ocean Region*. Ed. by Arthur Grantz, L. Johnson, and J. F. Sweeney. United Sates: Geological Society of America, pp. 133–151. ISBN: 978-0-8137-5211-2 978-0-8137-5463-5. DOI: 10.1130/DNAG-GNA-L.133. URL: https://pubs.geoscienceworld.org/books/book/866/chapter/4862450/.

Lee, Allison et al. (2020a). "Evanescent to propagating internal waves in experiments, simulations, and linear theory". en. In: *Experiments in Fluids* 61.12, p. 252. ISSN: 0723-4864, 1432-1114. DOI: 10.1007/s00348-020-03077-4. URL: http://link.springer.com/10.1007/s00348-020-03077-4.

– (2020b). "Evanescent to Propagating Internal Waves in Experiments, Simulations, and Linear Theory". In: *Experiments in Fluids* 61.12, p. 252. ISSN: 0723-4864, 1432-1114. DOI: 10.1007/s00348-020-03077-4.

Lees, Jonathan M and Jeffrey Park (1995). "Multiple-taper spectral analysis: A stand-alone C-subroutine". In: *Computers & Geosciences* 21.2, pp. 199–236.

Lilly, Jonathan and Shane Elipot (Apr. 2021). *Jonathanlilly/jLab: jLab v1.7.1*. Zenodo. DOI: 10.5281/ZENODO.4547006.

Lincoln, Ben J. et al. (Sept. 2016). "Wind-driven Mixing at Intermediate Depths in an Ice-free Arctic Ocean". In: *Geophysical Research Letters* 43.18, pp. 9749–9756. ISSN: 0094-8276, 1944-8007. DOI: 10.1002/2016GL070454. (Visited on 02/08/2024).

Liu, Kun et al. (2022). "Turning depths of internal tides in the South China Sea inferred from profile data". en. In: *Acta Oceanologica Sinica* 41.2, pp. 139–146. ISSN: 0253-505X, 1869-1099. DOI: 10.1007/s13131-021-1837-8. URL: https://link.springer.com/10.1007/s13131-021-1837-8.

Marshall, John et al. (1997). "Hydrostatic, Quasi-hydrostatic, and Nonhydrostatic Ocean Modeling". In: *Journal of Geophysical Research: Oceans* 102.C3, pp. 5733–5752. ISSN: 0148-0227. DOI: 10.1029/96JC02776.

Martini, Kim I. et al. (2014). "Near-Inertial Internal Waves and Sea Ice in the Beaufort Sea*". In: *Journal of Physical Oceanography* 44.8, pp. 2212–2234. ISSN: 0022-3670, 1520-0485. DOI: 10.1175/JPO-D-13-0160.1.

McDougall, Trevor J. and Paul M. Barker (2011). *Getting started with TEOS-10 and the Gibbs Seawater (GSW) Oceanographic Toolbox*. eng. OCLC: 724024071. Battery Point, Tas.: Trevor J McDougall. ISBN: 978-0-646-55621-5.

– (2014). "Comment on "Buoyancy frequency profiles and internal semidiurnal tide turning depths in the oceans" by B. King et al." en. In: *Journal of Geophysical Research: Oceans* 119.12, pp. 9026–9032. ISSN: 21699275. DOI: 10.1002/2014JC010066. URL: http://doi.wiley.com/10.1002/2014JC010066.

Meyer, Amelie et al. (2017). "Mixing rates and vertical heat fluxes north of Svalbard from Arctic winter to spring: N-ICE2015 ARCTIC TURBULENCE OBSERVATIONS". en. In: *Journal of Geophysical Research: Oceans* 122.6, pp. 4569–4586. ISSN: 21699275. DOI: 10.1002/2016JC012441. URL: http://doi.wiley.com/10.1002/2016JC012441.

Nurser, A. J. G. and S. Bacon (2014). "The Rossby radius in the Arctic Ocean". en. In: *Ocean Science* 10.6, pp. 967–975. ISSN: 1812-0792. DOI: 10.5194/os-10-967-2014. URL: https://os.copernicus.org/articles/10/967/2014/.

Olbers, Dirk Jürgen (2012). *Ocean dynamics*. First edition. Heidelberg ; New York: Springer. ISBN: 978-3-642-23449-1.

Padman, L. and T. M. Dillon (1988). "On the horizontal extent of the Canadian Basin thermohaline steps". In: *J. Phys. Oceanogr.* 18, p. 1458.

Paoletti, M. S., Matthew Drake, and Harry L. Swinney (2014a). "Internal tide generation in nonuniformly stratified deep oceans". en. In: *Journal of Geophysical Research: Oceans* 119.3, pp. 1943–1956. ISSN: 21699275. DOI: 10.1002/2013JC009469. URL: http://doi.wiley.com/10.1002/2013JC009469.

– (2014b). "Internal Tide Generation in Nonuniformly Stratified Deep Oceans". In: *Journal of Geophysical Research: Oceans* 119.3, pp. 1943–1956. ISSN: 21699275. DOI: 10.1002/2013JC009469.

Paoletti, M. S. and Harry L. Swinney (2012a). "Propagating and evanescent internal waves in a deep ocean model". en. In: *Journal of Fluid Mechanics* 706, pp. 571–583. ISSN: 0022-1120, 1469-7645. DOI: 10.1017/jfm.2012.284. URL: https://www.cambridge.org/core/product/identifier/S0022112012002844/type/journal_article.

– (2012b). "Propagating and Evanescent Internal Waves in a Deep Ocean Model". In: *Journal of Fluid Mechanics* 706, pp. 571–583. ISSN: 0022-1120, 1469-7645. DOI: 10.1017/jfm.2012.284.

Pedlosky, Joseph (2003). *Waves in the ocean and atmosphere: introduction to wave dynamics*. Vol. 260. Springer.

Peterson, Algot K. et al. (2017). "Turbulent heat and momentum fluxes in the upper ocean under Arctic sea ice: TURBULENT FLUXES UNDER ARCTIC SEA ICE". en. In: *Journal of Geophysical Research: Oceans* 122.2, pp. 1439–1456. ISSN: 21699275. DOI: 10.1002/2016JC012283. URL: http://doi.wiley.com/10.1002/2016JC012283.

Pinkel, Robert (2005). "Near-Inertial Wave Propagation in the Western Arctic". en. In: *Journal of Physical Oceanography* 35.5, pp. 645–665. ISSN: 1520-0485, 0022-3670. DOI: 10.1175/JPO2715.1. URL: http://journals.ametsoc.org/doi/10.1175/JPO2715.1.

– (2008). "The Wavenumber–Frequency Spectrum of Vortical and Internal-Wave Shear in the Western Arctic Ocean". In: *Journal of Physical Oceanography* 38.2, pp. 277–290. ISSN: 1520-0485, 0022-3670. DOI: 10.1175/2006JPO3558.1.

Rainville, L., C. M. Lee, and R. A. Woodgate (2011a). "Impact of Wind-Driven Mixing in the Arctic Ocean". In: *Oceanography* 24, pp. 136–145.

Rainville, Luc, Craig Lee, and Rebecca Woodgate (2011b). "Impact of Wind-Driven Mixing in the Arctic Ocean". In: *Oceanography* 24.3, pp. 136–145. ISSN: 10428275. DOI: 10.5670/oceanog.2011.65. URL: https://tos.org/oceanography/article/impact-of-wind-driven-mixing-in-the-arctic-ocean.

Rainville, Luc and Peter Winsor (2008). "Mixing across the Arctic Ocean: Microstructure observations during the Beringia 2005 Expedition". en. In: *Geophysical Research Letters* 35.8, p. L08606. ISSN: 0094-8276. DOI: 10.1029/2008GL033532. URL: http://doi.wiley.com/10.1029/2008GL033532.

Rainville, Luc and Rebecca A. Woodgate (2009). "Observations of internal wave generation in the seasonally ice-free Arctic". en. In: *Geophysical Research Letters* 36.23, p. L23604. ISSN: 0094-8276. DOI: 10.1029/2009GL041291. URL: http://doi.wiley.com/10.1029/2009GL041291.

Rippeth, Tom P. et al. (2015). "Tide-Mediated Warming of Arctic Halocline by Atlantic Heat Fluxes over Rough Topography". In: *Nature Geoscience* 8.3, pp. 191–194. ISSN: 1752-0894, 1752-0908. DOI: 10.1038/ngeo2350.

Rippeth, Tom P. et al. (2017a). "Tidal Conversion and Mixing Poleward of the Critical Latitude (an Arctic Case Study)". en. In: *Geophysical Research Letters* 44.24. ISSN: 0094-8276, 1944-8007. DOI: 10.1002/2017GL075310. URL: https://onlinelibrary.wiley.com/doi/10.1002/2017GL075310.

– (2017b). "Tidal Conversion and Mixing Poleward of the Critical Latitude (an Arctic Case Study)". In: *Geophysical Research Letters* 44.24. ISSN: 0094-8276, 1944-8007. DOI: 10.1002/2017GL075310.

Schlindwein, Vera (2023). *The Expedition PS137 of the Research Vessel POLARSTERN to the Arctic Ocean in 2023*. Ed. by Horst Bornemann and Susan Amir Sawadkuhi. Bremerhaven. DOI: 10.57738/BzPM_0781_2023.

Schmitt, R. W. et al. (1987). "C-SALT: an Investigation of the Thermohaline Staircase in the Western Tropical North Atlantic". In: *Deep-Sea Res.* 34, pp. 1697–1704.

Shibley, N. C. et al. (2017). "Spatial variability of the Arctic Ocean's double-diffusive staircase". In: *Oceanography* 122, pp. 980–994.

Shibley, Nicole C., Mary-Louise Timmermans, and Christian Stranne (2020). "Analysis of Acoustic Observations of Double-Diffusive Finestructure in the Arctic Ocean". In: *Geophysical Research Letters* 47.18, e2020GL089845. ISSN: 0094-8276, 1944-8007. DOI: 10.1029/2020GL089845.

Spreen, G., L. Kaleschke, and G. Heygster (2008). "Sea Ice Remote Sensing Using AMSR-E 89-GHz Channels". In: *Journal of Geophysical Research: Oceans* 113.C2, 2005JC003384. ISSN: 0148-0227. DOI: 10.1029/2005JC003384.

Sutherland, B. R. (2010a). *Internal gravity waves*. OCLC: ocn601113971. Cambridge ; New York: Cambridge University Press. ISBN: 978-0-521-83915-0.

Sutherland, B. R. (2010b). *Internal Gravity Waves*. Cambridge, UK: Cambridge University Press, p. 378.

– (2016). "Internal Wave Transmission through a Thermohaline Staircase". In: *Phys. Rev. Fluids* 1. doi:10.1103/PhysRevFluids.1.013801, 013701:1–13.

Sutherland, B. R. and K. Yewchuk (2004). "Internal Wave Tunnelling". In: *J. Fluid Mech.* 511, pp. 125–134.

Sutherland, Bruce R. (2010c). *Internal Gravity Waves*. Cambridge: Cambridge university press. ISBN: 978-0-521-83915-0.

Thomas, Leif N. and Xiaoming Zhai (2022). "The lifecycle of surface-generated near-inertial waves". en. In: *Ocean Mixing*. Elsevier, pp. 95–115. ISBN: 978-0-12-821512-8. DOI: 10.1016/B978-0-12-821512-8.00012-8. URL: https://linkinghub.elsevier.com/retrieve/pii/B9780128215128000128.

Timmermans, M-L. and Chris Garrett (2006). "Evolution of the Deep Water in the Canadian Basin in the Arctic Ocean". en. In: *Journal of Physical Oceanography* 36.5, pp. 866–874. ISSN: 1520-0485, 0022-3670. DOI: 10.1175/JPO2906.1. URL: http://journals.ametsoc.org/doi/10.1175/JPO2906.1.

Timmermans, M-L., H. Melling, and L. Rainville (2007). "Dynamics in the Deep Canada Basin, Arctic Ocean, Inferred by Thermistor Chain Time Series". en. In: *Journal of Physical Oceanography* 37.4, pp. 1066–1076. ISSN: 1520-0485, 0022-3670. DOI: 10.1175/JPO3032.1. URL: http://journals.ametsoc.org/doi/10.1175/JPO3032.1.

Timmermans, M.-L. et al. (2008). "Ice-Tethered Profiler Observations of the Double-Diffusive Staircase in the Canada Basin Thermocline". In: *J. Geophys. Res.* 113, C00A02.

Timmermans, M.-L. et al. (2010). "Moored observations of bottom-intensified motions in the deep Canada Basin, Arctic Ocean". en. In: *Journal of Marine Research* 68.3, pp. 625–641. ISSN: 0022-2402. DOI: 10.1357/002224010794657137. URL: http://www.ingentaconnect.com/content/10.1357/002224010794657137.

Timmermans, Mary-Louise, Chris Garrett, and Eddy Carmack (2003). "The thermohaline structure and evolution of the deep waters in the Canada Basin, Arctic Ocean". en. In: *Deep Sea Research Part I: Oceanographic Research Papers* 50.10-11,

pp. 1305–1321. ISSN: 09670637. DOI: 10.1016/S0967-0637(03)00125-0. URL: https://linkinghub.elsevier.com/retrieve/pii/S0967063703001250.

Timmermans, Mary-Louise and John Marshall (2020). "Understanding Arctic Ocean circulation: A review of ocean dynamics in a changing climate". In: *Journal of Geophysical Research: Oceans* 125.4, e2018JC014378.

Walsh, John E. et al. (2017). "A database for depicting Arctic sea ice variations back to 1850". en. In: *Geographical Review* 107.1, pp. 89–107. ISSN: 0016-7428, 1931-0846. DOI: 10.1111/j.1931-0846.2016.12195.x. URL: https://www.tandfonline.com/doi/full/10.1111/j.1931-0846.2016.12195.x.

Wang, Shuya et al. (2023). "Burst Events of Near-Inertial Waves in the Beaufort Sea". In: *Progress in Oceanography* 212, p. 102986. ISSN: 00796611. DOI: 10.1016/j.pocean.2023.102986.

Wunsch, S. (2018). "Nonlinear Harmonic Generation by Internal Waves in a Density Staircase". In: *Phys. Rev. Fluids* 3, p. 114803.

Zhao, Bowen and Mary-Louise Timmermans (2018). "Topographic Rossby Waves in the Arctic Ocean's Beaufort Gyre". en. In: *Journal of Geophysical Research: Oceans* 123.9, pp. 6521–6530. ISSN: 2169-9275, 2169-9291. DOI: 10.1029/2018JC014233. URL: https://onlinelibrary.wiley.com/doi/10.1029/2018JC014233.

Zhao, Zhongxiang et al. (2010). "Long-Range Propagation of the Semidiurnal Internal Tide from the Hawaiian Ridge". In: *Journal of Physical Oceanography* 40.4, pp. 713–736. ISSN: 1520-0485, 0022-3670. DOI: 10.1175/2009JPO4207.1.

Zhou, S.-Q. et al. (2014). "The instability of diffusive convection and its implication for the thermohaline staircases in the deep Arctic Ocean". en. In: *Ocean Science* 10.1, pp. 127–134. ISSN: 1812-0792. DOI: 10.5194/os-10-127-2014. URL: https://os.copernicus.org/articles/10/127/2014/.

Zhou, Sheng-Qi and Yuan-Zheng Lu (2013). "Characterization of double diffusive convection steps and heat budget in the deep Arctic Ocean: DDC and Heat Budget in the Deep Arctic". en. In: *Journal of Geophysical Research: Oceans* 118.12, pp. 6672–6686. ISSN: 21699275. DOI: 10.1002/2013JC009141. URL: http://doi.wiley.com/10.1002/2013JC009141.

Zodiatis, G. and G. P. Gasparini (1996). "Thermohaline staircase formations in the Tyrrhenian Sea". In: *Deep-Sea Res.* 43, pp. 655–678.

# Acknowledgements

*a mi Papá, Vidal Bracamontes... La próxima vez no habrá ciencia, trabajaremos juntos la huerta (1940-2021).*

I would like to express my deep gratitude to my supervisor, Maren Walter, who led this project and always supported and trusted me. Thank you for allowing me to develop my ideas and for giving me the opportunity to study internal waves at the Gakkel Ridge. I would also like to thank Martin Losch, my co-advisor, for his valuable advice and feedback throughout the project. Thank you for all your help with the MITgcm model. Especially during the difficult times of the Covid pandemic, I felt that Maren and Martin had infinite patience with me. Thank you, Dirk Olbers, for agreeing to be one of the reviewers of this thesis and thank to the members of the examining board. Special thanks to Bruce Sutherland for hosting me during my research stay at the University of Alberta in Canada. I gained a wealth of knowledge about internal waves and fluid dynamics during this time, opening up a new world that I am excited to explore. My experience in Edmonton would not have been the same without my roommate Simon. Thank you for all the shared moments - bike rides, movie nights, and delicious German-Mexican fusion food.

I also appreciate the opportunity to participate in the M188 expedition and would like to thank Christian Mertens for trusting me with the microstructure profiler. After this expedition I traveled through the deserts of Namibia, this experience was unique, thank you for this beautiful time, Che, Moritz, Silvano, Emelie, Zoi and Jürgen.

I would like to thank Monika Rhein and the Physical Oceanography group, especially my friends and colleagues Ilmar, Dinora, Peter, Simon, Wiebke, Kevin, Illaria, Linn, Lara as well as my friends outside the university Mirko, Julian, Philip and *Las Chicas*. You have made this journey a wonderful experience.

My Ph.D. was made possible by ArcTrain, and I thank everyone involved in making this project a reality. A special mention goes to Michal Kucera, who led ArcTrain. My appreciation also extends to all the ArcTrain members with whom I shared time during our retreats. I was associated with the TRR181 project, and I would like to

thank the organizers, principal investigators, and all the members for providing me with such an enriching scientific experience.

All my love to my family, especially my mother, Rogelina, and my siblings, Alicia and Victor Hugo, all the achievements are dedicated to you. This journey would not have been possible without the love and unwavering support of my family. Finally, I would like to express my deepest gratitude to the Braun family and especially to my partner Lisa-Marie. Du hast mein Leben und meine Zeit in Deutschland bereichert. Ohne dich hätte ich es nicht geschafft.

# Declaration of Originality

I, Joel Bracamontes Ramírez, declare that this thesis is my own work, unless otherwise stated. In Chapter 2, I explicitly acknowledge the contribution of Prof. Dr. Bruce Sutherland, stating that he developed Sections 2.2.1, 2.2.2, and Appendix A, which I have included for completeness. Parts of Chapter 1 and all of Chapters 2 and 3 have been published in Phys. Rev. Fluids and J. Geophysical Res. Oceans.

Bremen, August 7, 2024

Joel Bracamontes Ramírez